

# **Development of a Large-scale Continuous Carbon Fiber Composite Additive Manufacturing System Based on Fused Granular Fabrication**

by

Anish Abraham Philip

A thesis submitted in partial fulfillment for the degree of  
Master of Science

Department of Mechanical Engineering  
University of Alberta

©Anish Abraham Philip, 2024

## **Abstract**

The thesis details the design and development of a method to additively manufacture continuous carbon fiber in a polyether ether ketone (PEEK) polymer matrix at a large scale. The majority of the additive manufacturing techniques are limited by size and printing time. Furthermore, the mechanical characteristics of typically 3D printed polymers are often inadequate for use in industrial settings. The prevalent technique in polymer additive manufacturing is fused filament fabrication, which necessitates the production of polymer filaments. This raises the cost of raw materials and confines the process to conventional filament dimensions. Considering these shortcomings, the study aims to investigate fused granular fabrication (FGF) based 3D printing which uses polymer in pellet form. A three-axis cartesian gantry based FGF printing system with a screw-based pellet extruder was constructed for studying the process parameters that influence the printing of a performance polymer. For this study, PEEK, an engineering thermoplastic frequently used in the aerospace and medical industry, was used. Employing a design of experiments approach, a study was conducted on printing temperature, bead overlap, layer height, and material throughput rate to obtain the optimal parameters to print parts with near zero porosity and minimal surface deformities. Tensile test was conducted on parts printed with the optimal set of parameters and compared with other manufacturing processes. During the study a variety of challenges involved with 3D printing high performance thermoplastics were resolved, such as issues with delamination, warping, and poor bed adhesion. For the second half of the thesis, a novel nozzle was designed with the capability of 3D printing in-situ impregnated continuous carbon fiber reinforced polymer (CCFRP). Parametric computational fluid dynamics analysis was performed on the design to optimize the temperature distribution and flow behavior of PEEK polymer through the nozzle. In order to utilize the benefits of printing CCFRP by employing nonplanar printing path, a six-axis robotic arm based FGF printer and components were constructed. A newly fabricated nozzle was implemented along with the screw-based pellet extruder on the robotic system and PEEK-CCFRP was printed as a proof of concept.

## **Acknowledgements**

I would like to express my sincerest appreciation to my supervisors Dr. Pierre Mertiny and Dr. Ahmed Jawed Qureshi. Their guidance, advice and supervision have made this work a success. They have always had my best interest and supported me during challenging times. Thank you for all your time and support. I would also like to thank Dr. David Nobes for his inputs and invaluable guidance for the project.

I would like to thank Dr. Abdullah Mohiuddin for his guidance for the project and help with reviewing the thesis. I am grateful to my colleagues Piyush Arora, Adam Lim and Ahmed Elsherbiny for lending a hand at various stages of the project. I would like to thank Minahil Tauqir and Nathan Wieczorek for setting up the controls and electrical side of the machine. I am also thankful to Vinay for his assistance with CAD design and manufacturing.

I would also like to thank my friends John Sunny, Alvin Alexander, Arun Biradar, Jorge Palacios Moreno, Rohith Naikuli and Yingnan Wang for their constant support and encouragement.

I am indebted to the members of the Engineering Machine Shop for their support and help in the manufacturing of parts for the machine. I am also grateful to the Department of Mechanical Engineering for giving me this opportunity.

Lastly and most importantly, I would like to thank my Family. Amma and Acha, you have been my biggest supporters and your prayers keep me going daily. I am eternally indebted for it. Thanks to my brother as well, Ashi, let's keep pushing the boundaries like we always do.

# Table of Contents

Abstract.....	ii
Acknowledgements.....	iii
Table of Contents.....	iv
List of Tables.....	vi
List of Figures.....	vii
List of Abbreviations.....	ix
Chapter 1 Introduction.....	1
1.1 Motivation.....	1
1.2 Literature review.....	2
1.2.1 State of the art in large scale polymer additive manufacturing.....	3
1.2.2 Overview of Fused Granular Fabrication (FGF) process.....	7
1.2.3 Overview of high temperature engineering polymer-based material extrusion.....	12
1.2.4 Advancements in continuous fiber reinforced polymer 3D printing.....	17
1.3 Thesis hypothesis and research objectives.....	21
1.4 Thesis structure.....	22
Chapter 2 Experimental setup.....	23
2.1 Materials.....	23
2.1.1 Poly ether ether ketone (PEEK).....	23
2.1.2 Commingled carbon fiber.....	26
2.2 Fabrication system.....	27
2.2.1 Extruder.....	27
2.2.2 Manipulator.....	29
2.2.3 Print bed.....	31
2.2.4 Heating system.....	32
2.2.5 Pellet feeding system.....	33
Chapter 3 Process parameter optimization for FGF of PEEK.....	37
3.1 Parameters influencing FGF.....	37
3.2 Methodology.....	38
3.3 Challenges in 3D printing PEEK.....	42
3.3.1 Bed adhesion.....	42
3.3.2 Material oozing from nozzle.....	44

3.3.3 Delamination.....	45
3.3.4 Warping of printed parts .....	46
3.4 Results and Discussion .....	47
3.4.1 Mass flow rate measurement .....	47
3.4.2 Bead width calculation.....	50
3.4.3 Statistical analysis for optimizing inter-bead porosity.....	52
3.4.4 Statistical analysis for optimizing surface uniformity .....	57
3.4.5 Validation of optimized response .....	61
3.5 Mechanical characterization.....	62
3.6 Conclusions .....	64
Chapter 4 Design of a continuous carbon fiber/PEEK co-extrusion nozzle .....	65
4.1 Nozzle design considerations.....	65
4.1.1 Factors influencing nozzle design .....	65
4.2 First design iteration .....	67
4.3 Second design iteration .....	71
4.4 Numerical analysis of PEEK flow in nozzle .....	72
4.5.1 SolidWorks Flow Simulation setting and computational domain.....	74
4.5.1 Material model for non-Newtonian PEEK material .....	75
4.5.2 Boundary conditions .....	78
4.5.5 Results and discussion .....	82
4.6 Integration of nozzle with extruder .....	91
4.7 Conclusions .....	94
Chapter 5 Conclusions and future work .....	95
5.1 Conclusions .....	95
5.2 Future work.....	97
References .....	98
Appendix 1 .....	109
Appendix 2 .....	110
A2.1 cFRP Nozzle assembly.....	111
A2.2 Drawing for PEEK Block.....	112
A2.3 Drawing for CF Nozzle.....	113
A2.4 Drawing for Impregnation Nozzle.....	114

## List of Tables

Table 1. Large scale AM systems available in the market (adopted from [34]).	6
Table 2. Process parameters and their influence on FGF printing [55,57-62].	10
Table 3. Literature review on PEEK 3D printing via material extrusion.	15
Table 4. Literature review on CFRP additive manufacturing.	20
Table 5. Dimension of SJ-35 extruder.	28
Table 6. Specifications of the gantry.	30
Table 7. Specification of robotic arm.	31
Table 8. Decision matrix for pellet feeding system.	34
Table 9. Range of controlled process parameters used for various experiments.	37
Table 10. Parameter levels for mass flow rate measurement.	38
Table 11. DoE for determining optimum bead width.	39
Table 12. Printing parameters are selected to optimize for minimize inter bead porosity and maximize surface uniformity.	39
Table 13. Experimental runs for DoE to minimize inter-bead porosity and maximize surface uniformity.	40
Table 14. Temperature readings highlighting the effect of IR heating system.	46
Table 15. Flow rate measurement at an extrudate temperature of 360°C.	48
Table 16. Flow rate measurement at an extrudate temperature of 390°C.	48
Table 17. Bead width measured for the statistical analysis.	50
Table 18. Analysis to determine the validity of terms in Equation 5.	52
Table 19. Model summary for the regression Equation 5.	52
Table 20. Porosity measurement for each run of the DoE.	53
Table 21. Analysis of variance for inter-bead porosity versus screw motor RPM, h/D, overlap%.	55
Table 22. Surface uniformity measurements for the DoE samples.	58
Table 23. Analysis of surface uniformity versus screw motor RPM, h/D, overlap%.	59
Table 24. Optimized set of process parameters for printing minimal porous and surface deformity parts, the predicted and measured value.	61
Table 25. Tensile test comparison data for PEEK parts	64
Table 26. Mass of components mounted on robot arm.	66
Table 27. Decision matrix for material selection for nozzle parts.	67
Table 28. Mass flow rate boundary condition for various screw motor speeds.	79
Table 29. Parametric study for study on the nozzle components	86
Table 30. Predicted extrusion velocity for 5mm nozzle with varying screw motor speed	89
Table 31. Surface force measured along the fiber surface.	91
Table 32. Parameters used for initial testing of nozzle.	93

# List of Figures

Figure 1. Types of AM processes. ....	3
Figure 2. Types of material extrusion based additive manufacturing: a) Screw based, b) plunger based, c) filament based [28]. ....	5
Figure 3. Illustration of the working principle and components of FGF extruder. ....	7
Figure 4. Geometric characteristics of an auger screw. ....	8
Figure 5. Parameters affecting FGF process. ....	11
Figure 6. Material properties influencing material extrusion process [71]. ....	13
Figure 7. Classification of thermoplastics in the industry based on application [80]. ....	14
Figure 8. Molecular structure of PEEK. ....	14
Figure 9. Components constructed using composite materials on Airbus A380 [108]. ....	18
Figure 10. Illustration of various continuous fiber printing technique [112]. ....	19
Figure 11. PEEK 5600G pellets. ....	23
Figure 12. Graph plotting weight and weight% vs. temperature from temperature ramp TGA at 10°C/min. ....	25
Figure 13. Graph plotting weight and weight% vs. time from the isothermal hold TGA at 400°C. ....	26
Figure 14. Commingled carbon fiber. ....	27
Figure 15. Screw geometry. ....	28
Figure 16. Schematic of extruder barrel. ....	29
Figure 17. Three-axis cartesian gantry. ....	29
Figure 18. Robotic printing system. ....	30
Figure 19. Heated print bed. ....	31
Figure 20. Schematic of IR heater setup. ....	32
Figure 21. IR heater setup. ....	33
Figure 22. Compressed air flows through the inlet ① into an annular plenum chamber②. It is then injected into the throat through directed nozzles ③. These jets of air create a vacuum at the intake ④ which draws material in and accelerates it through it ⑤ at long vertical or horizontal distances [124]. ...	34
Figure 23. Model# 6080 Line Vac product used in the feeding system [6]. ....	35
Figure 24. Sample printed for DoE. ....	40
Figure 25. Point of measurements for surface deformity. ....	41
Figure 26. Measurement of maximum and minimum point of top face of sample. ....	41
Figure 27. Cross-section of sample magnified under optical microscope. ....	42
Figure 28. Part separating from the print bed due to poor bed adhesion. ....	43
Figure 29. Laser textured AISI304 printing surface. ....	44
Figure 30. Material oozing from the nozzle. ....	45
Figure 31. Delaminated layers after printing. ....	46
Figure 32. Shrinkage characteristics of semi-crystalline polymers due to temperature change [103]. ....	47
Figure 33. Printed parts warped from uneven cooling of material. ....	47
Figure 34. Plot of mass flow rate measured at different screw motor speed at 360°C and 390°C. ....	49
Figure 35. Plot of average bead width data from the DoE runs. ....	51
Figure 36. Factor effect plots and surface plots for porosity: a) Main effect plots, b) interaction plots. ..	56
Figure 37. Factor effect plots and surface plots for surface uniformity: a) Main effect plots, b) interaction plots. ....	60

Figure 38. Cut piece of PEEK sample printed with optimized parameters. ....	61
Figure 39. Geometry of sample 3D printed for machining out tensile test coupons. ....	62
Figure 40. Dimensions (in mm) of tensile test coupons according to ISO 527-2 Type 1B. ....	62
Figure 41. Stress strain curve for the PEEK printed samples. ....	63
Figure 42. Sideview of the initial nozzle design concept with overall dimensions in mm. ....	68
Figure 43. Side view and cross-section view of the initial nozzle design concept. ....	69
Figure 44 Exploded view of the initial nozzle design concept. ....	70
Figure 45. Final nozzle design with overall dimensions in mm. ....	71
Figure 46. Side view and cross-section view of the final nozzle design. ....	71
Figure 47. Exploded view of the final nozzle design. ....	72
Figure 48. Computational domain for simulation: a) Top view, b) front view, c) isometric view, d) side view. ....	74
Figure 49. Temperature dependent density of PEEK [26]. ....	76
Figure 50. Specific heat capacity of PEEK as a function of temperature. ....	76
Figure 51. Thermal conductivity of PEEK as a function of temperature [27]. ....	77
Figure 52. Viscosity behavior of PEEK with increasing shear rate [25]. ....	77
Figure 53. Simulation coordinate system. ....	78
Figure 54. Intel mass flow rate and the face it is applied to. ....	79
Figure 55. Environmental pressure and the faces it is applied to. ....	80
Figure 56. Faces in the assembly that will be heated. ....	80
Figure 57. Faces on which there is no heat loss through convection. ....	81
Figure 58. Mesh generated for the simulation. ....	82
Figure 59. Flow trajectory with color gradient representing fluid flow velocity. ....	83
Figure 60. Velocity plot along the cross-section of the flow orifice. ....	84
Figure 61. Flow trajectory of polymer in the final nozzle design. ....	87
Figure 62. Velocity profile of polymer at cross-section in final nozzle design. ....	87
Figure 63. Pressure profile of polymer at cross-section in final nozzle design. ....	88
Figure 64. Illustration depicting the axis along which velocity is measured. ....	88
Figure 65. Velocity plot along the central axis of the impregnation nozzle. ....	89
Figure 66. CAD model with the carbon fiber tow used for viscous force calculation simulation. ....	90
Figure 67. Sleeve heater assembly on PEEK block part. ....	92
Figure 68. Coil heater assembly on 5mm nozzle ....	92
Figure 69. Extrusion trial using newly designed nozzle ....	93
Figure 70. Rectangular geometry of 100mm x 70mm x 11mm 3D printed using PEEK. ....	109
Figure 71. 3D printed PEEK block of 200mm x 70mm x 11mm. ....	109
Figure 72 . Tensile test samples machined out as per ISO 527 from 3D printed PEEK block. ....	109

## List of Abbreviations

FGF: Fused granulated fabrication  
AM: Additive manufacturing  
RP: Rapid prototyping  
CF: Carbon fiber  
CCF: Continuous carbon fiber  
CAD: Computer aided design  
PLA: Polylactic acid  
ABS: Acrylonitrile butadiene styrene  
PBF: Powder bed fusion  
FFF: Fused filament fabrication  
FDM: Fused deposition modelling  
PEEK: Polyether ether ketone  
PETG: Polyethylene terephthalate glycol  
PA: Polyamide (Nylon)  
PVA: Polyvinyl alcohol  
PC: Polycarbonate  
ASA: Acrylonitrile styrene acrylate  
PA12: Polyamide 12 (Nylon12)  
PA66: Polyamide 66 (Nylon 66)  
PEI: Polyethylenimine  
PPS: Polyphenylene sulfide  
PPSU: Polyphenylenesulfone  
PESU: Polyethersulphone  
GF: Glass fiber  
WF: Wool fiber  
HIPS: High impact polystyrene  
PP: Polypropylene  
PET: Polyethylene terephthalate  
PEKK: Polyether ketone ketone  
cFRP: Carbon fiber reinforced polymer  
RPM: Rotations per minute

DoE: Design of experiments

OL: Adjacent bead overlap

CFD: Computational fluid dynamics

AISI: American iron and steel institute

# Chapter 1 Introduction

Additive Manufacturing (AM) formally encompasses what was previously referred to as Rapid Prototyping (RP) and commonly recognized as 3D printing. With the progression of this technology, there has been a notable enhancement in the quality of output, bringing it closer to a finished product. The distinctive feature of the AM process lies in the addition of material in layers, compared to conventional manufacturing methods that typically involve material removal to achieve the final part. Furthermore, AM only necessitates dimensional details, an understanding of the process, and knowledge of the materials to be used, as opposed to the intricate planning required in traditional manufacturing, involving the sequencing of machining features, fixture development for support, and various tooling and die needs [1,2]. These advantages have spurred extensive research into refining the technology, materials, and tools associated with the AM process.

Throughout this study, we explore the potential of leveraging the AM process particularly in the material extrusion process for high-performance engineering polymers. We investigate its thermal and mechanical effects on material consolidation, as well as the impact of process parameters on critical responses. The goal is to develop a comprehensive understanding that will ultimately facilitate the establishment of a system for the industrial-scale 3D printing of continuous fiber-reinforced polymer composites.

The present chapter discusses the motivation behind carrying out the studies conducted in this thesis. A comprehensive literature survey was conducted, detailing the state of the art and supporting the motivation of the project. Finally, the thesis hypothesis and objectives are defined based on the literature survey.

## 1.1 Motivation

The flexibility to produce intricate shapes with very short lead times has increased the popularity of AM techniques in recent years. Especially in polymer product manufacturing, this leads to faster and cheaper customized part production. While many companies have started to adopt this manufacturing technique, 3D printing still has some significant shortcomings. The additive manufacturing processes are subject to key limitations, including [3-6]:

- The production speed for 3D printed components is comparatively lower than that of subtractive manufacturing.
- Parts that can be produced are constrained in size to an average volume of  $10^{-3}\text{m}^3$ .
- Material feedstock is costly, with an average price of USD\$100/kg due to the requirement to produce preprocessed polymer filaments.

- The majority of the commonly available polymers for 3D printing are not suitable for engineering applications.

Material extrusion for polymers is frequently constrained by fast cooling rates (resulting from significant temperature differences between the print and ambient environment), phase transformation, and delamination issues. Commonly used commercial materials, such as PLA and ABS, have limitations as they become fluidic at temperatures below 250 °C [7-9], with a tensile strength not exceeding 60 MPa [10,11]. Although suitable for prototyping, these polymers lack the strength and other enhanced properties necessary for the production of functional parts. These materials are not suitable for applications in industries where parts need to survive extreme environments, such as the aerospace, automotive and biomedical sectors, even though a desire exists to deploy AM in the production. A viable resolution to this issue involves employing high-temperature engineering polymers in the material extrusion process. These polymers typically exhibit semi-crystalline characteristics, ensuring thermal stability and toughness. Nevertheless, a significant challenge arises from the elevated processing temperatures and the consequential high shrinkage during part cooling, which leads to issues such as warping and delamination from the print bed [12,13]. Additionally, the crystallization process poses a hindrance to inter-layer adhesion, as the crystals act as a barrier to polymer chain diffusion [14]. This highlights a research gap in the field, particularly in the context of scaling up the industrial printing of high-temperature engineering polymers.

Moreover, the addition of fiber reinforcement has been proven to improve the mechanical performance of additively manufactured parts. It has been reported that the incorporation of carbon fiber into polymer feedstock results in heightened thermal conductivity, diminished thermal expansion, significantly decreased warping in larger prints, lowered residual stresses within the part, and an enhanced dimensional accuracy of the printed components [15]. The majority of the research has been focused on development of short fiber reinforcement as opposed to continuous fiber reinforcement that avails significantly higher strength and stiffness [16,17]. Yet, enhancing polymers with continuous fiber in 3D printing presents a more significant challenge, demanding a distinctive feeding system unlike that used for short fiber reinforcement printing [15]. This presents another research opportunity to develop a system that can concurrently print high temperature engineering polymer reinforced with continuous fiber that can be utilized at an industrial scale.

## **1.2 Literature review**

This section discusses the state of the art in the field of large-scale polymer additive manufacturing, the advancements in the fused granular fabrication process and continuous fiber reinforced polymer 3D printing.

### 1.2.1 State of the art in large scale polymer additive manufacturing

Large scale additive manufacturing is believed to play an important role in the latest industrial transformation known as Industry 4.0 [18]. It is reported by Frost & Sullivan's Global Additive Manufacturing Market that the aerospace, automotive and medical sectors account for nearly 51% of the 3D printing market share by 2025 [19]. There has also been a rapid growth of 3D printing technology in the construction sector [20]. As a result, improving the built volume and deposition rate of 3D printers has significant advantage for these industries.

There are a number of additive manufacturing processes that can be leveraged for the manufacturing of thermoplastic polymers. Figure 1 lists the various AM techniques.

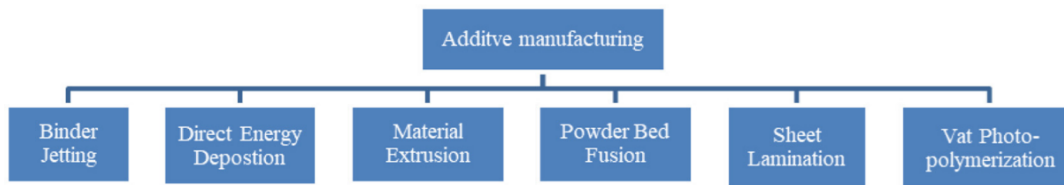


Figure 1. Types of AM processes.

1. Powder bed fusion is a printing technique where a laser-based heat source consolidates polymers in powder form. The heat source is applied to the powder on the print bed that gradually moves through each layer as powder gets spread for the subsequent layers thus forming a 3D structure. The primary benefit of PBF technique is that the un-sintered powder material acts as a support structure eliminating the requirement for a dedicated support structure. The printing technique comes with its own disadvantages in sustainability unless un-sintered powder material is recycled, the process requires costly machinery like a laser heat source and this burdens the scaling of this technology [21-23].
2. Material jetting (MJ) is a printing technique where droplets of the feedstock material are selectively deposited onto print surface. The deposited material is usually photopolymerized or allowed to solidify by cooling. The advantage of the technique over others is the ability to print comparatively thin layers allowing high print quality and lesser stair-stepping effect. Since the polymer is injected in a molten form, multiple polymers can be combined in a single MJ technology. This is popularly known as the multi-jetting technique [24]. A crucial gap in the technique is that since the material used usually has low viscosity, it compromises the mechanical properties of the finished part [25].

3. The laminated object manufacturing (LOM) method lays down individual cross-section layers that are cut out and laminated together using diffusion binding, low melting point alloys, adhesive polymers, or ultrasound. A variety of shapes, like honeycomb structures and spherical shells with holes, can be built using this technology [26]. Additionally, this technique is suitable for printing continuous fiber reinforced parts. However, the method faces limitations due to material availability, subpar surface quality, and the need for post-processing to enhance mechanical properties and dimensional accuracy [27].
4. Material extrusion-based 3D printing melts the polymer feedstock in a nozzle and deposits on to the print surface, as depicted in Figure 2. The material extrusion process is usually classified based on the feeding system of the printer as follows [28,29]:
  - a) Screw based extrusion or fused granular fabrication (FGF) takes inspiration from the injection molding where feedstock is in the form of pellets or powder, which is fed into an auger screw where material is melted and fused to form a molten form that is extruded through a nozzle onto a print bed layer by layer. The process requires bulkier machineries and multiple heat zones when compared to fused filament fabrication process (see item c) below). But due to the high pressure exerted by the screw and scalability of the equipment, it is suitable for printing high temperature and high viscosity polymer at a large scale [31], which will be discuss in greater detail in Section 1.2.2.
  - b) Plunger based extrusion also utilizes the feedstock in the form of pellets or powder which are pre-fed into a reservoir and melted. This molten material is pushed out using a plunger. While this technique shares the benefits of FGF process in scalability and printing of high viscosity polymers, it is limited to continuous printing based on the size of the reservoir. This limitation can lead to poor interlayer adhesion as printed parts may cool down during the delay for subsequent print cycles [32]. It was also identified that the limitation of continuous polymer extrusion can hinder the ability to print continuous fiber reinforced polymer parts.
  - c) Filament based extrusion, also known as fused filament fabrication (FFF) or fused deposition modelling (FDM), first developed by the Stratasys company [30], is the most popular and widely used 3D printing process. The method takes in feedstock in the form of filaments that are melted in a hot end and deposited onto a print bed layer by layer creating a 3D structure. The major reason for the method's popularity compared to other polymer manufacturing system is the ease of manufacturing, cheap components, and process control in the system. A disadvantage of this process is the required filament fabrication process which adds to feedstock cost [30]. FFF is also limited in scalability as the material deposition rate depends on

the size of the filament which is typically limited to 2.85mm in commercially available sources [31], [33].

Based on the knowledge of various AM techniques employed for thermoplastics, a literature survey was carried out to understand the various large format polymer 3D printing system currently available in market or in a research capacity. The survey has been summarized in Table 1.

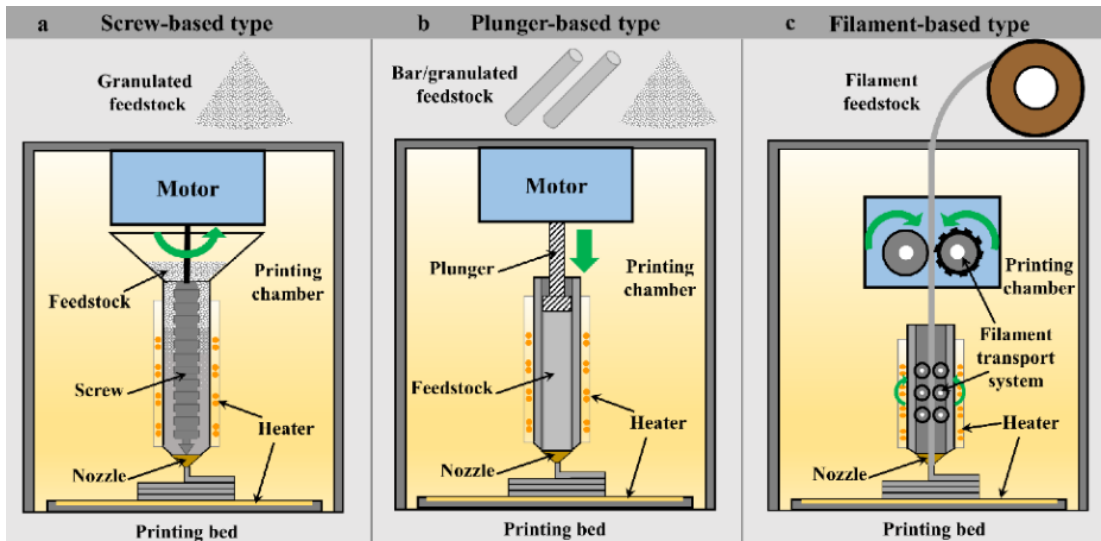


Figure 2. Types of material extrusion based additive manufacturing: a) Screw based, b) plunger based, c) filament based [28].

It is noteworthy to highlight the advancements achieved by the Stratasys company through its "Infinite Build 3D Demonstrator." This thermoplastic pellet extrusion system has the theoretical capability to print objects of unlimited length. The system, featuring eight axes, has undergone successful testing by industry leaders such as Ford Motor Company and Boeing. It has demonstrated efficacy in producing lightweight components and facilitating the exploration of innovative materials [48].

According to the literature survey, as detailed in Table 1, there have been major advancements in scaling the polymer additive manufacturing system to incorporate the capability of producing parts at a higher production rate and industrial scale. But it is also evident that most of the developed large-scale AM system focus mainly on commodity plastics or at most engineering polymers (polymer classification will be provided in Section 1.2.3). It is evident that the compatibility to print high performance engineering polymer at a large scale is limited, which proves the requirement to study and create an understanding of how process parameters that influence the material extrusion process interact while printing high performance engineering polymers.

Table 1. Large scale AM systems available in the market (adopted from [34]).

Model	Brand	Technology	Build volume (m <sup>3</sup> )	Material compatibility
Massivit 1800 [35]	Massivit 3D	MJ	3.2	Photopolymers
Massivit 1500 [35]	Massivit 3D		2.5	
3DGD-1800 [35]	Mimaki		2.9	
Jupiter [36]	ATMAT	FFF	2	PLA, PETG, PA, ABS, PVA (for limited geometry printouts)
400 Series Workbench Xtreme [35]	3D Platform		1.05	PLA, PET, PA, PC, ABS, ASA
BigRep Pro [37]	BgRep		1	PA12 CF, PA6, PA66, ASA, PLA, PETG, HI-TEMP**, BHOV**
D1000 [38]	CreatBot		1	ABS, PLA, PETG, PA, PC, PEI, PEEK
Delta WASP 60100 [39]	WASP		1.2	PLA, ABS, PETG, PA/Carbon
BAAM [40]	Cincinnati Incorporated		25	ABS, PPS, PC, PLA, PEI Composites of carbon fiber, glass fiber, or organic fiber with abovementioned polymers
MasterPrint [41]	Ingersoll		48	PLA, ABS, PETG, PC, PPSU, PEI and composites with CF, GF, WF and above polymers
LSAM 1540 [42]	Thermwood	81	Max print temperature up to 450°C	
MILLE-500XL [43]	MilleBot	15.36	ABS, PLA, HIPS, PETG etc.	
CFAM Prime [44]	CEAD	12	ABS, ASA, PA6, PC, PEEK, PEI, PESU, PETG, PLA, PP, HDPE, Continuous fiber reinforced polymers	
The Box Large [35]	BLB Industries	6	PLA, PET, PA, PC, ABS, ASA	
Super Discovery [45]	CNC Barcenas	3.25	Max print temperature up to 400°C	
Atlas 3.6 [46]	Titan Robotics	3	PEI, PEKK, ABS, PA, CF-PEI, GF-PEKK	
Delta WASP 3MT Industrial 4.0 [47]	WASP	1.2	PLA, ABS, PET, ASA, PLA+Wood, PLASMIX	
Flexbot Industry [146]	CEAD	4	PLA, PP, ABS, ASA, PET, PC, PEEK, PESU, PPS combined with GF, cellulose fiber or CF	
MDAC50 additive cell [147]	Massive dimension	4.2	ABS, PLA, HIPS, PETG	

\*SLM stands for selective laser melting, a process that falls under PBF.

\*\* Proprietary material of the brand.

### 1.2.2 Overview of Fused Granular Fabrication (FGF) process

Single screw extruders were first used for extrusion of thermoplastics material in the early 1930s. The material inside the barrel is subjected to heat and considerable shear force that fuses the material and pushes it forward through its flight [49]. The molten fluid is pushed forward by the axial component of the drag flow created by the motion of the screw, and the transverse flow generated by the drag flow component is primarily responsible for the mixing action [50]. As briefly described in Section 1.2.1, the FGF printing technique operates by transferring feedstock material in the form of pellets from the inlet to the nozzle opening via an auger screw. Prior to extrusion through the nozzle, the molten plastic experiences high pressure facilitated by the screw, which consists of transport, melting, and mixing zones. The pellets transition from a solid to a viscous state through a heater that heats the screw and barrel. The motor, linked to the screw, induces rotation, applying substantial pressure for extrusion, as illustrated in Figure 3. This screw extruder system is attached onto a manipulator that follows the path generated from a CAD model. The material is deposited in a layer-by-layer fashion until the desired 3D structure is created. Conventionally the screw extruders were used for injection molding of polymers and in the food processing industry, such that the extruder material is pressurized into a die [51,52].

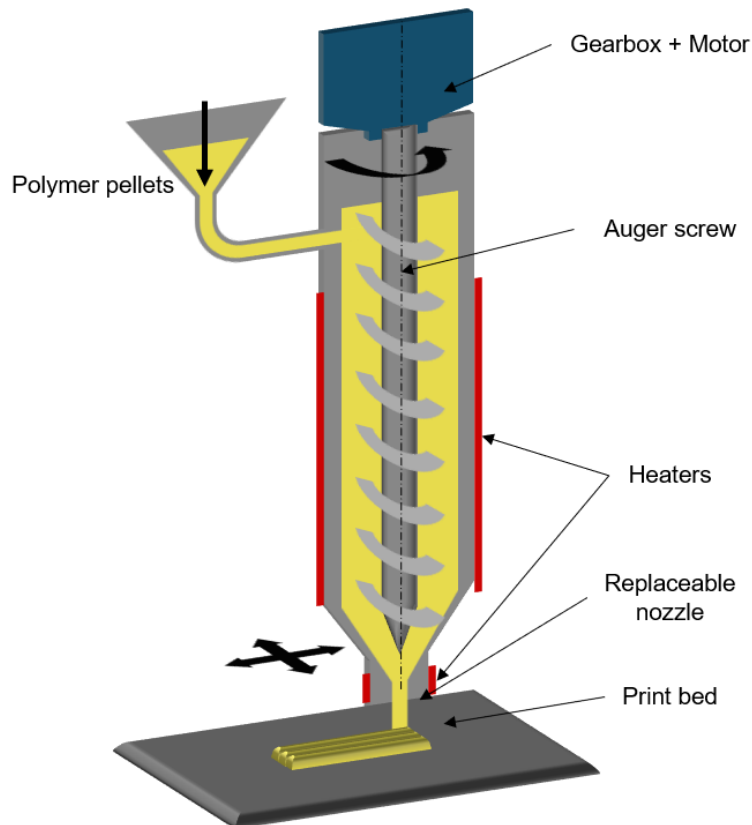


Figure 3. Illustration of the working principle and components of FGF extruder.

The auger screw (see Figure 4) is the most significant component in the extruder as the dimensional features of the screw directly influence the extruder throughput, rate of melting, mixing, melt temperature homogeneity and process efficiency [53]. The main characteristics that affect these properties of the extrudate are the length of the screw, length to diameter ratio, the compression ratio, flight width (pitch) and the channel depth. The length of the screw and the screw rotation speed dictates the residence time of the polymer in the screw [49,54]. Polymers are not readily sheared and require greater melting by conduction. The compression ratio correlates between the channel depth in the feeding section and the channel depth in the metering section, playing a significant role in influencing the mixing process. The compression ratio plays a critical role while extruding polymer composites or multiple polymers [53,145].

Other critical components in the extruder are the driver motor with a gearbox coupled to the screw which delivers sufficient torque for material extrusion and mixing. The torque requirement is proportional to the diameter of the screw. Likewise, the torque requirement is proportional to the screw speed [55].

Another important aspect is the temperature of the extrudate. The main source of energy to melt the feedstock is from the heat transfer between the heated barrel and the polymer, and viscous dissipation of mechanical energy into heat inside the polymer material. The rate of heat transfer is proportional to the amount of contact area between the barrel and the flowing material while heat due to viscous dissipation is proportional to the volume of the material. Viscous dissipation of mechanical energy dominates especially at low moisture contents and at high screw speeds [50,56]. The material is gradually heated from the feeding section to the nozzle. This curb overheating and thus degradation of the polymer [56].

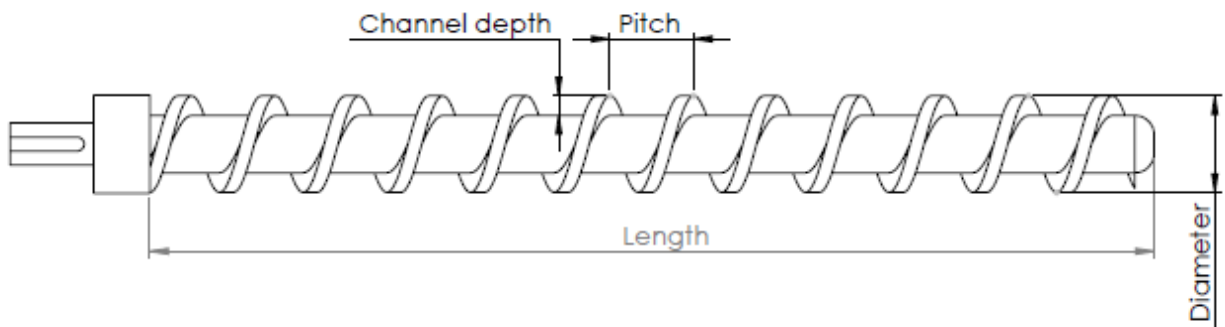


Figure 4. Geometric characteristics of an auger screw.

A thorough understanding of the process parameters that influence the FGF process and how they influence the final printing is required in order to optimize the process for high performance polymers. From the literature survey on the working principles of the FGF based material extrusion [55,57-62] the parameters in Table 2 were highlighted to have an influence on the printing process. Figure 5 provides a graphical illustration of the process parameters that were explored in the present study.

Table 2. Process parameters and their influence on FGF printing [55,57-62].

<b>Parameter</b>	<b>Independent/ dependent</b>	<b>Influenced parameters</b>	<b>Influence on printed part</b>
Screw speed (RPM)	Independent	N/A	Determines the rate of material flow through the screw flight and ultimately rate of material extruded
Extruder temperature (°C)	Independent	Material melting and degradation temperatures	Material temperature is dictated by the parameter thus dictating the viscous material properties that influence the mechanical properties of the finished part.
Nozzle diameter (mm)	Independent	N/A	Directly proportional to extrusion velocity and influences bead width thus determines the rate of printing
Mass flow rate (kg/hr)	Dependent	Linearly proportional to screw speed	Determines the rate of printing
Scanning velocity (mm/min)	Independent	N/A	This parameter can be independently controlled but it has to be tuned based on screw speed, layer height and nozzle diameter to achieve consistent bead widths
Extrusion velocity (mm/sec)	Dependent	Linearly proportional to screw speed Inversely proportional to nozzle diameter	Determines the rate of printing
Layer height (mm)	Independent	N/A	Has a major influence on print quality as it influences the stair stepping effect. Higher the layer height, more significant the stair stepping effect. It also dictates the bead geometry in conjunction with extrusion velocity and scanning velocity.
Bed temperature (°C)	Independent	N/A	Usually determined by the degree of adhesion between the first layer of polymer and print surface. For semi-crystalline polymer it is maintained slightly above the glass transition temperature
Environmental temperature (°C)	Independent	N/A	Influences the cooling rate of the deposited material. Insufficient material temperature can lead to poor inter-layer adhesion. Cooling rate of the material dictates the crystallization rate which in turn dictates shrinkage and mechanical performance of the polymer
Bead width (mm)	Dependent	Influenced by nozzle diameter, extrusion velocity, scanning velocity and layer height	Bead width influences the quality of the finished parts as it is the resolution of the printing process. It also is used to control the bead overlap.
Bead overlap (%)	Dependent	Calculated from bead width	This is a significant parameter that determines the mechanical performance of the finished part as it directly influences inter-bead porosity. An optimal bead overlap ensures the elimination of these porosities.

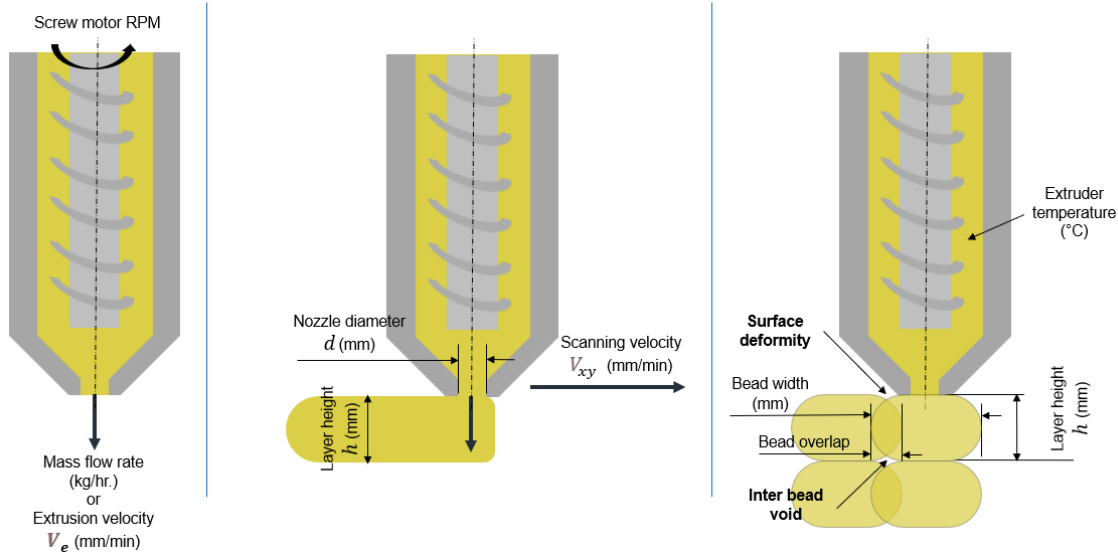


Figure 5. Parameters affecting FGF process.

The screw-based extrusion process has key advantages over the other material extrusion-based printing technique particularly while considering large format additive manufacturing. Since the auger screw, driver motor and barrel construction can be scaled up and down, the rate and scale of printing can be proportionally varied [31,33]. Typically, the nozzle diameter for FFF systems is smaller than 1mm and the deposition ranges from 1 to 20mm/s with a maximum print volume of 300mm x 300mm x 300mm. In comparison, for large scale prints the nozzle diameter ranges from 0.8mm to 10mm with deposition speeds from 20mm/s to 280mm/s with print volumes starting at 800mm x 600mm x 600mm. This shows that in order to achieve the objective of printing at large scale, screw-based extrusion process is an apt choice of technology based on its scalability [33]. Similarly, the screw produces much higher pressure compared to the filament feeding system which allows for the printing of high viscosity polymer and polymer composites. In terms of the feedstock used, the FGF system provides a cost-effective solution as the polymers are used in the form of pellets. This eliminates the need to manufacture filaments or fine powder that serves as feedstock for other AM processes. To put into perspective the disparity in cost, the unit cost of PLA pellets averages at \$2/kg while a filament of the same material can cost an average of \$25/kg, which shows a nearly 10x increase in cost of producing parts comparing FGF and FFF process [64-66]. There are additional advantages to eliminating an added melt cycle in feedstock production such as reducing the embodied energy, faster production time, and direct support of recycled polymers [64]. The downside to the FGF technique is the requirement of higher capacity manipulators as the extruder components are much bulkier than the FFF components. The temperature control also needs greater analysis and experiments to optimize in FGF as a lack in understanding can lead to poor material extrusion and material degradation in the barrel.

### *1.2.3 Overview of high temperature engineering polymer-based material extrusion*

Thermoplastics are primarily used for the material extrusion process due to their melt processability, rigidity, comparatively high strength and high temperature tolerance, and stability, when compared with thermosets and elastomers [67]. Some of the most common polymers used with the material extrusion process are ABS, PLA, PC, PA, TPU, HIPS, ASA, PEEK, PEI, etc. The industry currently utilizes these thermoplastic parts produced through additive manufacturing for a range of applications [68-70].

As the previous section investigated the process parameters that influence the FGF process, here the material parameters that influence the machine design, process parameters and print quality are explored. Figure 6 illustrates some of the material properties and the stages of FGF at which their influence becomes significant. Another point to note is that most of the polymers exhibit a non-Newtonian shear thinning behavior which is an important property to consider when selecting the screw speed and extruder temperature. A printable window for each material has to be determined between the melting point and degradation temperature [71]. Rheological properties such as viscosity, shear stress, and elastic modulus have to be monitored to determine the printable window. The printable window is usually determined through a design of experiments (DoE) process. In order to carry out material extrusion-based 3D printing the polymer should ideally exhibit following behaviors [72,73]:

- Thixotropy and shear thinning behavior
- Optimal viscosity such that material is extrudable in a continuous filament for dimensional accuracy
- Rapid viscosity increases after deposition to maintain structural integrity
- Sufficient mechanical bonding with subsequent layers to avoid delamination during and after printing
- Minimal coefficient thermal expansion to reduce part shrinkage and warping after printing

If the thermoplastic is semi-crystalline, crystallinity also plays a major role in the material extrusion process, especially in the solidification phase of the deposited material. While crystallinity enhances the mechanical properties of the polymer, if the rate of crystallization is not controlled while the extrudate cools down, it can hinder the interlayer adhesion by restricting chemical bond formation. For this to occur the rate of crystallization should be sufficiently slow to allow for the delay of the deposition of the subsequent layer. Crystallization also induces additional shrinkage to the deposited material, inducing residual stresses [12,74-76]. Crystallization kinetics is a function of temperature and can be slowed down by controlling the cooling rate of the polymer after deposition [77]. The effect of crystallization and crystallization kinetics on print quality and mechanical properties of the printed part is a vast research area to be explored and requires a dedicated study.

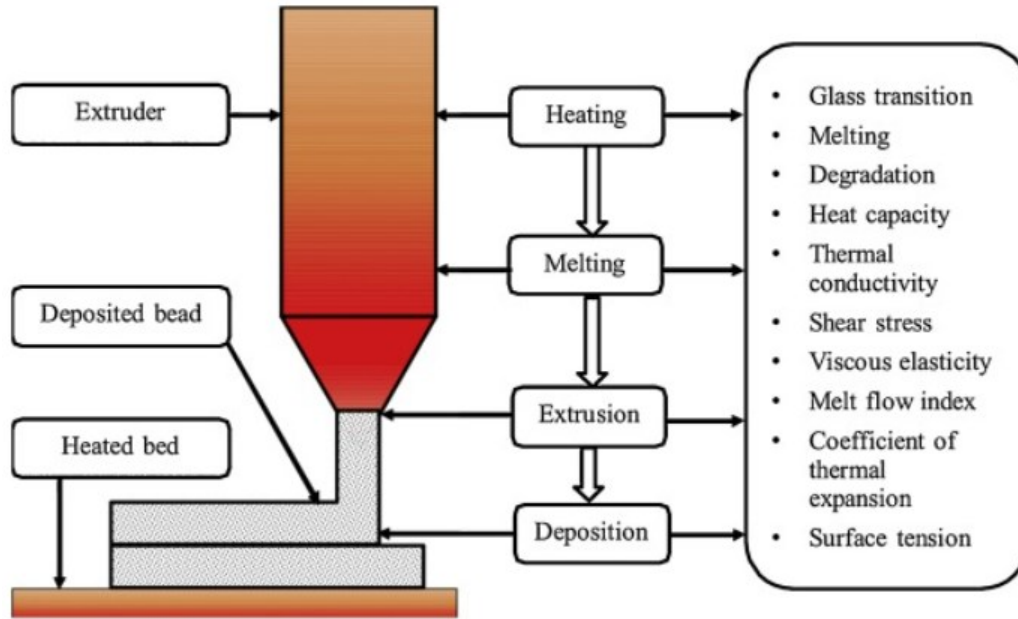


Figure 6. Material properties influencing material extrusion process [71].

In order to elevate the AM process from utilization for prototype parts to functional parts, production using high performance engineering polymer has to be carried out [72]. These polymers have superior mechanical performance, thermal stability, chemical resistance, and product quality compared to regular use plastics. Due to these desirable properties, they are generally employed in critical applications such as aerospace, defense, industrial and medical applications. These polymers are occasionally used as substitutes for metals and glass due to their superior strength to weight ratio [78-79]. Processing these polymers also comes with the challenges of elevated machinery requirement and controlled operational environment to reduce the residual stresses induced by thermal gradients [76].

The diagram in Figure 7 categorizes polymers commonly employed in the industry. Based on the objective to study the FGF process for high performance, the focus was on the top section of the pyramid. Based on various market surveys [81-83] that indicated popular polymers in aerospace [84-87], medical [88-90] and automotive [91-92] industries, PEEK was chosen as the high-performance engineering polymer for the present study. PEEK, which chemical structure is depicted in Figure 8, is also used as the matrix material in fiber reinforced composites, especially in the aerospace industry [86]. As per the material datasheet for PEEK450G (a high viscous grade of PEEK) from Victrex (Lancashire, United Kingdom) [93], its continuous operating temperature is 260°C with a Young's Modulus of 4GPa. Properties of the particular grade of PEEK used for the study are discussed in detail in Section 2.1.1.

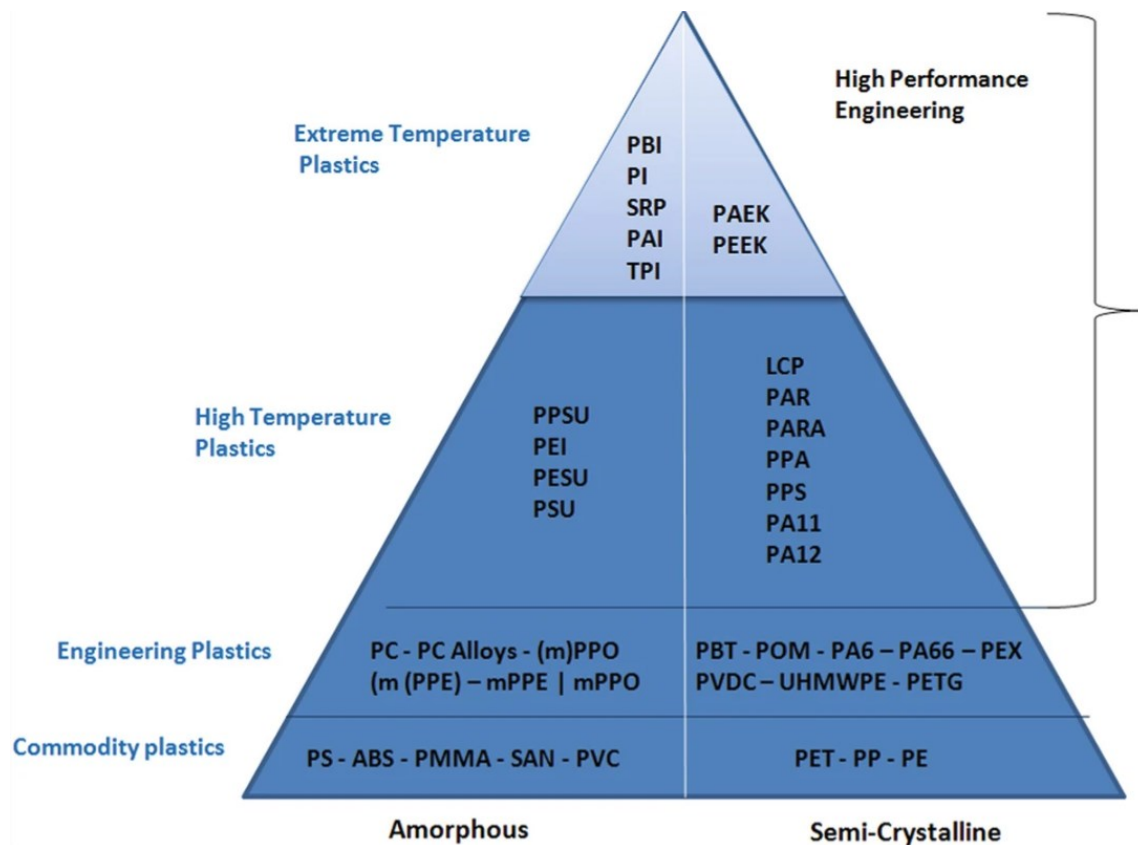


Figure 7. Classification of thermoplastics in the industry based on application [80].

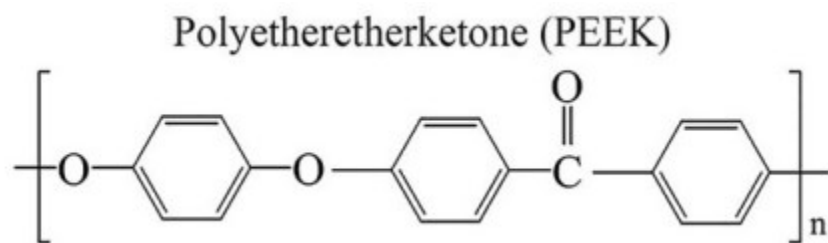


Figure 8. Molecular structure of PEEK.

To create an understanding about printing PEEK polymer, a review of existing literature was undertaken summarizing the processing parameters for printing PEEK, addressing the challenges linked to 3D printing this polymer, and examining the solutions proposed by other researchers. Table 3 details the findings from this literature review.

Table 3. Literature review on PEEK 3D printing via material extrusion.

Reference	Printing technology	Experimental description	Observations and conclusions
Jian-Wei et al., (2017) [57]	FGF	Design of screw for printing PEEK Adhesion testing with print bed Tensile and compressive mechanical testing	Optimal range of L/D ratio for screw is between 18:1 – 24:1 Bed temperature was maintained at 280°C Linearly proportional relation between flow rate and screw speed Extruder temperature was varied between 370 – 390°C
Tafaoli-Masoule et al., (2022) [94]	FFF	Process parameter optimization for mechanical properties and porosity evaluation Parameters of DoE: Nozzle temperature: 390 - 440°C Bed temperature: 120 – 160°C Print speed: 10 – 50mm/sec Layer height: 0.1 – 0.2mm	Nozzle temperature had the most effect (42%) on tensile strength followed by layer thickness and print speed. Bed temperature did not have significant effect. Higher nozzle temperature degraded the PEEK and created micropores from the escaping gas. Lower temperature caused insufficient bonding leaving inter-bead voids Best set of printing parameters: Nozzle temperature at 415°C, bed temperature at 160°C, layer height at 0.1mm and print speed at 50mm/s
Pulipaka et al., (2023) [95]	FFF	Effect of process parameters on mechanical property and surface roughness Parameters of DoE Nozzle temperature: 390 - 405°C Bed temperature: 136 – 143°C Infill density: 70 – 85% Print speed: 15 – 20mm/sec Layer height: 0.1 – 0.2mm	Layer height (41%) and nozzle temperature (36.1%) had a significant effect on surface roughness. Nozzle temperature (41.9%) and layer height (29.7%) had significant effect on elastic modulus. Infill density (80.5%), bed temperature (8.9%), layer height (5.9%) and nozzle temperature (3.5%) significantly affected tensile strength No process parameters had significant effect on hardness, contact creep of the part.
(Atatreh et al., 2022) [96]	FFF	Effect of process parameter and annealing on dimensional accuracy of CF-PEEK Nozzle diameter: 0.4mm Infill density: 70% Nozzle temperature: 405°C Bed temperature: 130°C Chamber temperature: 90°C Print speed: 40mm/sec Layer height: 0.25mm	Parts printed with a geometric tolerance of $\pm 0.2$ mm. Dimensional accuracy was slightly improved by annealing.
(Rehekampff et al., 2019) [97]	FFF	Effect of process parameters on tensile strength Nozzle diameter: 0.4mm Infill density: 25 - 100% Raster angles: +45/-45°, 0/90° Nozzle temperature: 415°C Bed temperature: 260°C for first layer then reduced to 210°C Chamber temp: 200°C Print speed: 7.5 - 15mm/sec	Tensile strength of raster angles with 0/90° have more tensile strength than +45/-45°. Parts showed slightly higher tensile strength when locally cooled while printing. Lower print speeds provide better tensile strength for printed parts. Reinforcing PEEK with chopped CF improved the tensile strength by 42%.

		Layer height: 0.2mm Air cooling nozzle: 180°C	
Lee et al., (2022) [98]	FFF	Effect of convection in built chamber on material cooling rate, DOC, and crystalline morphology was investigated Raster angles: 0/90° Nozzle temperature: 420°C Bed temperature: 160°C Chamber temp: 90°C Print speed: 12mm/sec Nozzle fan speed: 0 – 100% (controlled chamber convection)	Independent of convection fast cooling rate resulted in negligible crystallization of 10% for single layer and 20% when subsequent layers are printed on top due to secondary heating cycle. However, with convection the secondary heating cycle is eliminated. Higher degree of crystallization was observed in slower cooled parts.
Yang et al., 2017 [99]	FFF	Effect of heat treatment on crystallinity and mechanical properties Raster angles: 0° Nozzle diameter: 0.4mm Nozzle temperature: 360 - 420°C Chamber temp: 25 - 200°C Layer thickness: 0.2mm Print speed: 40mm/sec Heat treatment: air cooling, furnace cooling, quenching, annealing, tempering	An increase in ambient temperature from 25 – 200°C increased the crystallinity from 17 – 31%. Nozzle temperature was found to influence crystal melting process, crystallization process, inter-bead adhesion and material degradation. Furnace cooling and annealing produced max crystallinity of 36% and 38% respectively.
(Zhao et al., 2021) [100]	FFF	Effect of process parameters and annealing on mechanical properties Raster angles: ±45° Nozzle diameter: 0.4mm Nozzle temperature: 360 - 420°C Bed temp: 80 - 140°C Layer thickness: 0.1mm Print speed: 20 - 80mm/sec Infill density: 100% Bead width: 0.6mm Fan speed: 50%	Optimal parameters for tensile strength: Nozzle temperature, print speed and bed temperature: 420°C, 20mm/s, 100°C Nozzle temperature had the main effect on tensile and flexural strength. Annealing improved the tensile strength by 28% due to increase in crystallinity.
(Geng et al., 2019) [101]	FFF	Effect of extrusion speed and printing speed Extrusion velocity: 0.1 – 120mm/min Print speed: 6.8 – 10.4mm/s	Melt pressure directly affects the surface morphology and extrusion diameter of the filament, and higher melt pressure is beneficial to reducing surface defects of the extruded filament. Linear relationship between extrusion speed and the diameter of extrusion filament within the extrusion speed range of 5 and 80mm/min. Accuracy improvement of printed samples is attributed to introducing the relationship of the extrusion speed and filament diameter into the extrusion control algorithm
(Wang et al., 2019) [102]	FFF	Design and testing of a hot end for PEEK Effect of printing parameters on mechanical properties, surface quality and microstructure	The density and surface quality of printed PEEK parts, internal defects, and binding strength between layers and infill filaments can be improved at higher temperatures and by decreasing the layer thickness and printing

		Nozzle diameter: 0.4 – 0.8mm Nozzle temperature: 380 - 440oC Layer thickness: 0.1 – 0.5mm Print speed: 17 - 26mm/sec	speed. The optimal parameters for printing PEEK were a heating temperature of 440 °C, printing speed of 20 mm/s, and printing layer thickness of 0.1 mm, respectively, which could insure the better mechanical properties and surface quality of PEEK parts.
--	--	---	---

As evident from Table 3, the majority of the research conducted focused on FFF of PEEK and the effect of process parameter and print strategy on dimensional accuracy and mechanical properties. A small number of articles investigated laser powder bed fusion for PEEK [103-104]. However, as this technology is not the focus of the present study, it has been excluded from the table for the sake of brevity. As per this author’s knowledge, only Jian-Wei et al. (2017) studied the FGF process for PEEK and reported on it. Another important point to note from the literature review is that all printing carried out is using a <1mm diameter nozzle, which has inferior material throughput rate. Additionally, due to the small diameter of beads extruded through such nozzles, the effect of thermal gradient, residual stresses, and melt and crystallization shrinkage is not highly manifested in the finished parts. This leaves a sizable research gap in terms of understanding the process parameters and challenges faced in FGF based material extrusion for PEEK material especially at large scale.

#### *1.2.4 Advancements in continuous fiber reinforced polymer 3D printing*

Fibers with high longitudinal strength and modulus are mixed into polymer matrices to form continuous fiber reinforced polymer (cFRP) composites. The fibers act as the load bearing elements with the polymer providing structural rigidity and a distribution of load among fibers. The polymers also protect fibers from environmental interaction and associated damage [105]. The continuously rising need for materials that are not only lighter but also stronger has resulted in the widespread adoption of cFRPs. These composites exhibit superior strength-to-weight and stiffness-to-weight ratios compared to metallic materials. Furthermore, the inclusion of polymers imparts excellent corrosion resistance to these materials [106]. In terms of impact resistance and fatigue damage tolerance, cFRP composites surpass the performance of metals [107]. The combination of these highly desirable properties positions cFRP composites as a favored choice for significant applications in the aerospace, automotive, and sporting goods industries. To contextualize the progress of composites, particularly in the aerospace industry, the material distribution in latest commercial airplanes like the Airbus A350 and Boeing B787 is slightly over 50% composites while their predecessors like the A340 and B777 contained just 10% to 15% [108]. Figure 9 shows some of the major components manufactured out of composites in the Airbus A380.

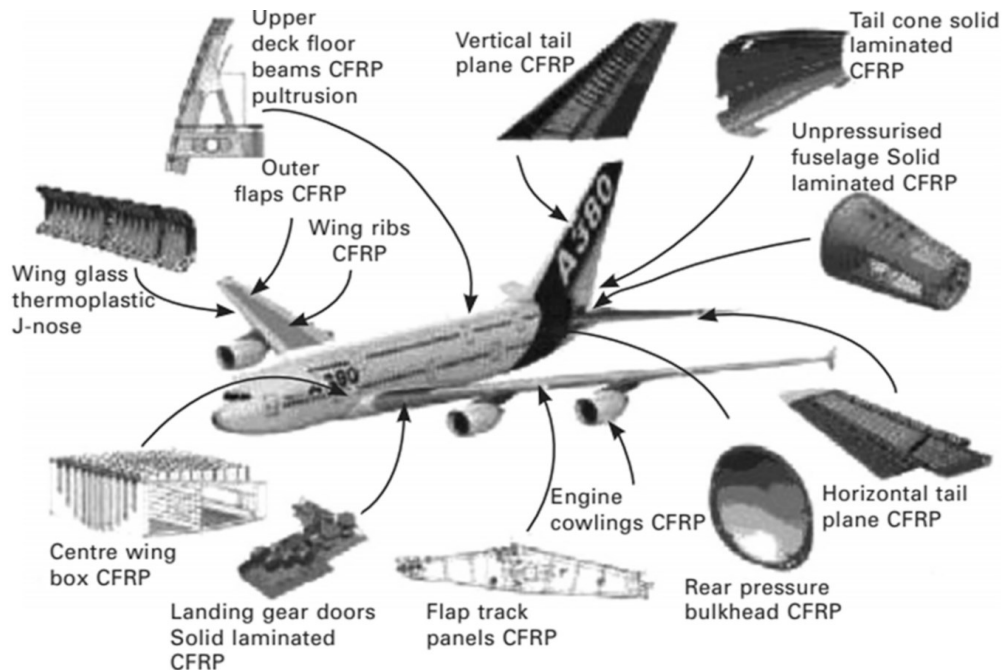


Figure 9. Components constructed using composite materials on Airbus A380 [108].

Despite the advantages of composites over metals, composites have certain shortcomings. Composites exhibit significant anisotropy. Except for the fiber direction, their performance is determined by the properties of the matrix material, which is inferior to the fiber phase. The interfacial interaction of polymer and fibers determines the load transfer capacity in composites and is a complicated challenge for design and manufacturing of composites. In laminated structures, the interlayer adhesion is usually weaker than the bulk of the material and the strength of the interface cannot be predicted during the design phase. Additionally, the design of these composite materials necessitates an in-depth understanding for utilizing the mechanical benefits that can be imparted by the fibers.

Conventional manufacturing processes of polymer composites also entails certain challenges and limitations. Composites are usually manufactured using laborious process like hand lay-up, which slows down production and drives up the cost of the parts [109]. Large composite parts are typically created using bulk polymerization which requires large autoclaves for heating and curing [110]. Most of the traditional composite manufacturing techniques require molds for manufacturing, and lack the capability to produce intricate geometries, and require post processing to obtain final parts [109], [111]. These challenges make it worthwhile to explore the use of AM techniques for manufacturing FRP composite parts.

Traditional 3D printers depend on thermoplastic filament or pellets to print parts layer by layer, but these parts lack the strength for industrial application. Introducing a reinforcement like carbon fiber into the

polymer can impart high strength and durability to 3D printed parts. Traditional printing nozzles are limited to the capability of printing chopped fibers, which can be mixed with the stock polymer. Hence, in order to use cFRP, a focused design change for the nozzle, feeding system for continuous fiber, and a fiber cutting mechanism is required. To facilitate this design task, a comprehensive investigation into the current state of the art in cFRP additive manufacturing was conducted. Techniques for continuous fiber-based printing has been classified based on the fiber impregnation process and consolidation of matrix. In the following, some notable techniques are summarized [112] and depicted in Figure 10:

1. In-situ impregnation: Dry fiber is introduced into the nozzle, while a matrix material is injected through one or more inlets during deposition through co-extrusion. The matrix is subsequently introduced, heated, and impregnates the fiber in situ before being deposited.
2. Co-extrusion with towpreg: Rather than using dry fiber, towpreg/thin prepreg tape is supplied to the nozzle, heated, and co-extruded with additional matrix material. The matrix in the towpreg is typically identical to that in the co-extrusion process.
3. Towpreg extrusion: The towpreg which already consists of the polymer mixed into the fiber is directly deposited without any additional matrix impregnation.
4. In-situ consolidation: Essentially, it is a reduced-scale adaptation of thermoplastic automated fiber placement (AFP), wherein the input thermoplastic towpreg/prepreg tape is consolidated in-situ upon deposition. The feedstock undergoes heating by an external energy source at the nozzle during the feeding process and is subsequently positioned and consolidated by a pressure roller during deposition.
5. In-line impregnation: The fiber undergoes impregnation while being transported into the print head, akin to the process of 3D filament winding. Similar to towpreg extrusion, the deposition occurs through a nozzle.

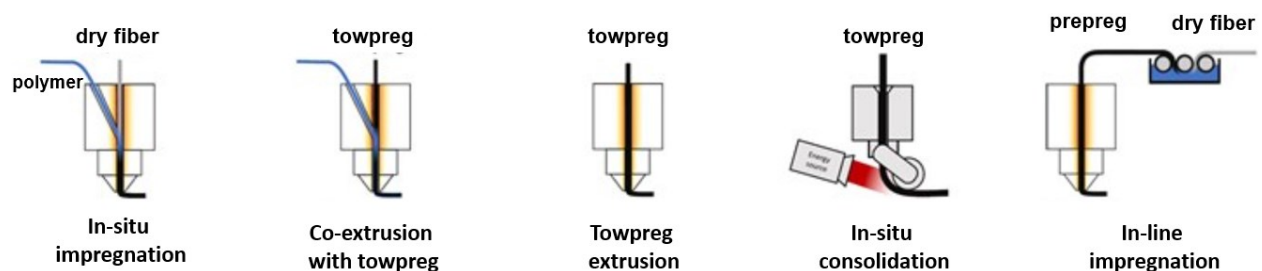


Figure 10. Illustration of various continuous fiber printing technique [112].

A literature review on the advances of cFRP based AM was undertaken to understand the various designs of the system, challenges faced in printing, benefits of reinforcing polymer printed parts, etc. This review is summarized in Table 4.

Table 4. Literature review on cFRP additive manufacturing.

Reference	Printing technology	Experimental description	Observations and conclusions
Yang et al., (2017) [113]	In-situ impregnation	Design of novel extrusion head and mechanical testing of printed parts Materials: ABS + CF (1K)	10 wt% carbon fiber reinforced parts were printed. Printed parts exhibited improved tensile (147MPa) and flexural (127MPa) strength compared to ABS parts. Interlayer shear strength (2.81MPa) was significantly reduced due to weak meso/micro scale interface in the 3D printed composite parts.
Caminero et al., (2018) [114]	Co-extrusion using MarkForged MarkTwo desktop printer	Interlayer shear strength determination Materials: Nylon + CF or GF or Kevlar fiber Layer height of unreinforced layer: 0.1 – 0.2mm Layer height of reinforced sample: CF: 0.125mm GF or Kevlar fiber: 0.1mm Infill density: 100% Fiber angle: 0°	The effects of the type of reinforcement and fiber content on the interlaminar bonding performance of reinforced nylon specimens were of particular significance. Carbon fiber reinforced composites exhibited the best interlaminar shear performance with higher stiffness followed by glass fiber and Kevlar respectively. Kevlar faced poor wettability. A compaction stage after deposition would be desirable to reduce porosity.
Meng et al., (2019) [115]	In-situ impregnation	Effect of process parameter on impregnation and laser heat source on interlayer bonding behavior Material: PEEK 150G or PEEK 450G + CF 50W fiber laser (1070nm) was used Fiber tow was passed through the nozzle to create a towpreg and this towpreg was again passed through nozzle for printing	Pre-impregnation and laser-based consolidation has improved mechanical performance. Selection of low-viscosity PEEK 150G improved impregnation and interlayer bonding compared to PEEK 450G. ILSS and flexural strength of 35MPa and 480MPa was obtained.
Liu et al., (2020) [116]	Towpreg extrusion	Development of a system for impregnation of fiber using high pressure via micro-screw Materials: PA12 + CF (1K or 3K) Screw speed, die diameter was varied for 1K and 3K fibers For printing hatch spacing, layer thickness and printing speed was varied	Melt impregnation of polymer into fiber bundle happened depending on the local high pressure and shear-thinning effect between the pin surface and fiber bundle. Fiber volume fraction improved from 31.9% to 50.2% for 3K-CCF/PA12 using the impregnation technique. Interfacial porosity was reduced to 0.15% in 1K-CCF/PA12 and 2.62% in 3K-CCF/PA12 Significantly promoted tensile and flexural strength
Rimasauskas et al., (2019) [117]	Co-extrusion with modified	Preprocessing technique to improve impregnation of polymer into fiber	Tensile test with impregnated carbon fiber tow showed that with the solution

	Geetech McCreator 2 printer	Materials: PLA or ABS or PC + CF (1K or 3K) Fibers was per-impregnated by passing them through a polymer bath.	concentration increasing the tensile force increases accordingly during tension Parts printed with these filaments also exhibited a similar trend. This tendency was significant in PLA and PC but not in ABS.
Qin et al., (2022) [118]	Towpreg extrusion	Effect of thermoplastic based sizing on carbon fiber in impregnation and mechanical performance for CF/PEEK prepreg for 3D printing PEI sizing with effective concentration of 20%. Deionized water was added to the PEI sizing in 1:19, 1:19 and 1:15 ratio by weight (PEI:water) PEEK sizing agent with effective concentration of 2.5%. Deionized water was added in a ratio of 3:2 by weight (PEEK:water)	The surface polarity and the activity of the carbon fibers have more significant impacts on the interface of the CF/PEEK composites rather than the impact by the surface roughness of the CFs. In comparison to unsized CF-reinforced PEEK composites, the tensile strength of PEI-sized CF/PEEK and PEEK-sized CF/PEEK composites increased by up to 47.6% and 54.0% respectively.
Matsuzaki et al., (2016) [119]	In-situ impregnation with modified Hotproceed Blade-1 printer	Process parameter analysis for tensile properties Materials: PLA + CF 924K or Jute fibers	Young's moduli and strength were enhanced nearly 5x for CF reinforced parts and 2x for jute fiber reinforced parts compared with pure thermoplastic parts. ~40 -50% volume fraction parts were printed

(Materials mentioned in the table are denoted as Matrix + Fiber format)

From the literature review, some of the challenges in printing cFRP and challenges in obtaining mechanical performance similar to conventional composite manufacturing techniques were identified. Significant challenges were poor interlayer adhesion due to poor interaction of matrix material during the layer-by-layer deposition, and poor impregnation of matrix material into the dry fibers. This was reported primarily for thermoplastic matrices due to the higher viscosity compared to thermosets. A few other techniques to improve the impregnation of polymers into fibers have been reported in literature [120,121,126]. Various mechanisms to tackle these challenges have also been detailed in the literature.

### 1.3 Thesis hypothesis and research objectives

This thesis work is aimed at developing a cFRP AM system that will be employed to study specially designed material extrusion-based AM toolpaths. The bird's eye view requirements for the system to be developed are,

- Capability to produce large scale industrial products

- High material throughput
- Compatibility with high performance and high temperature engineering polymers
- In-situ impregnated continuous fiber printing system

To fulfill the aforementioned criteria, the following objectives were established:

1. Identify and modify a screw-based extruder in order to meet the necessary process parameters for the selected polymer
2. Integration of extruder and material feeding system with large scale manipulator
3. Process parameter optimization to maximize print quality for basic geometries
4. Design, develop and manufacture a dedicated nozzle capable of impregnating continuous carbon fiber and polymer in parallel with the printing process
5. Integration of the developed nozzle with the screw extruder.

The thesis hypothesis is that the development of a cFRP AM system will meet the above stated requirements and will result in a technologically advanced and industrial viable solution for producing large scale industrial products.

## **1.4 Thesis structure**

The thesis is divided into five chapters. Chapter 1 explains the motivation for the work, including a comprehensive literature review to understand the latest advancements in this area. Chapter 2 details the experimental setup and the materials that were used throughout the project. The design of experiments studies conducted for the process parameter analysis for FGF are discussed in Chapter 3. The design, development and numerical analysis carried out for the continuous carbon fiber reinforced PEEK printing system are explained, and the integration and preliminary tests that were conducted, are outlined in Chapter 4. Chapter 5 summarizes the findings from the study and makes recommendation for future work.

## Chapter 2 Experimental setup

This chapter provides an in-depth exploration of the materials employed in the experiments and the machinery essential for constructing the additive manufacturing system. Section 2.1 delves into the polymer and continuous fiber utilized in the development of the additive manufacturing process. Section 2.2 provides a comprehensive breakdown of the specifications and configurations of the system's various components, including the extruder, manipulator, print bed, heating system, and pellet conveying system.

### 2.1 Materials

#### 2.1.1 Poly ether ether ketone (PEEK)

PEEK pellets of grade PEEK 5600G (JunHua PEEK, Jiangsu, China) were used for conducting the experiment. Pellets were of an average size of 2.5mm x 3.5mm in diameter and length, respectively. The material has a density of 1300kg/mm<sup>3</sup>. The glass transition temperature ( $T_g$ ) and melting temperature ( $T_m$ ) of the material are 143°C and 343°C, respectively, as per the manufacturer's datasheet. PEEK is a high-performance polymer with high specific strength, heat resistance, and chemical resistance, which makes it desirable for engineering applications. Tests on PEEK have shown that the polymer has a continuous use temperature of 260°C.

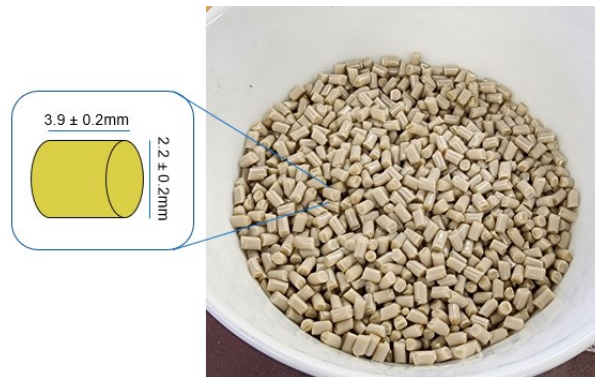


Figure 11. PEEK 5600G pellets.

PEEK absorbs moisture from atmospheric air, which causes distortions while 3D printing. To remove the moisture, PEEK pellets are dried at 120°C for 4hrs in an oven and are stored in an airtight container [122].

Thermal gravimetric analysis (TGA) was carried out on PEEK using Thermo Cahn 400 (Thermo Scientific, Waltham, Massachusetts, USA) to understand the rate of degradation of the material. TGA was conducted

in the presence of atmospheric air as it mimics the conditions inside the barrel. The following TGA studies were carried out:

1. Temperature ramp TGA: Temperature inside the testing chamber was ramped up at a rate of  $10^{\circ}\text{C}/\text{min}$  (as per ASTM E2550) from room temperature to  $750^{\circ}\text{C}$  (machine limit). The weight of the material is measured at a rate of 0.1hz to find the temperature at which the material starts to degrade and if the material completely disintegrates. Figure 12 shows a plot from the analysis. PEEK started to degrade at  $550^{\circ}\text{C}$ . The data also shows that at  $750^{\circ}\text{C}$ , PEEK was reduced to 18% of the initial mass.
2. Isothermal hold TGA: Temperature inside the test chamber was initially ramped up to  $400^{\circ}\text{C}$  at  $50^{\circ}\text{C}/\text{min}$  (maximum ramp up rate of the machine). Then, this temperature was maintained up to 10hrs to monitor the degradation of PEEK over time at  $400^{\circ}\text{C}$ . The particular temperature was selected as this is the maximum print temperature that was planned to be used for the DoE study. The data from the isothermal analysis also plays an important role in the extruder selection. The residence time of the extruder at minimum screw speed should be less than the time taken for the PEEK to degrade. The residence time influences the length to diameter ratio of the extruder screw and the minimum screw speed, which are critical parameters [123]. Figure 13 shows the plot from the isothermal TGA testing, where PEEK starts to degrade near 105 minutes.

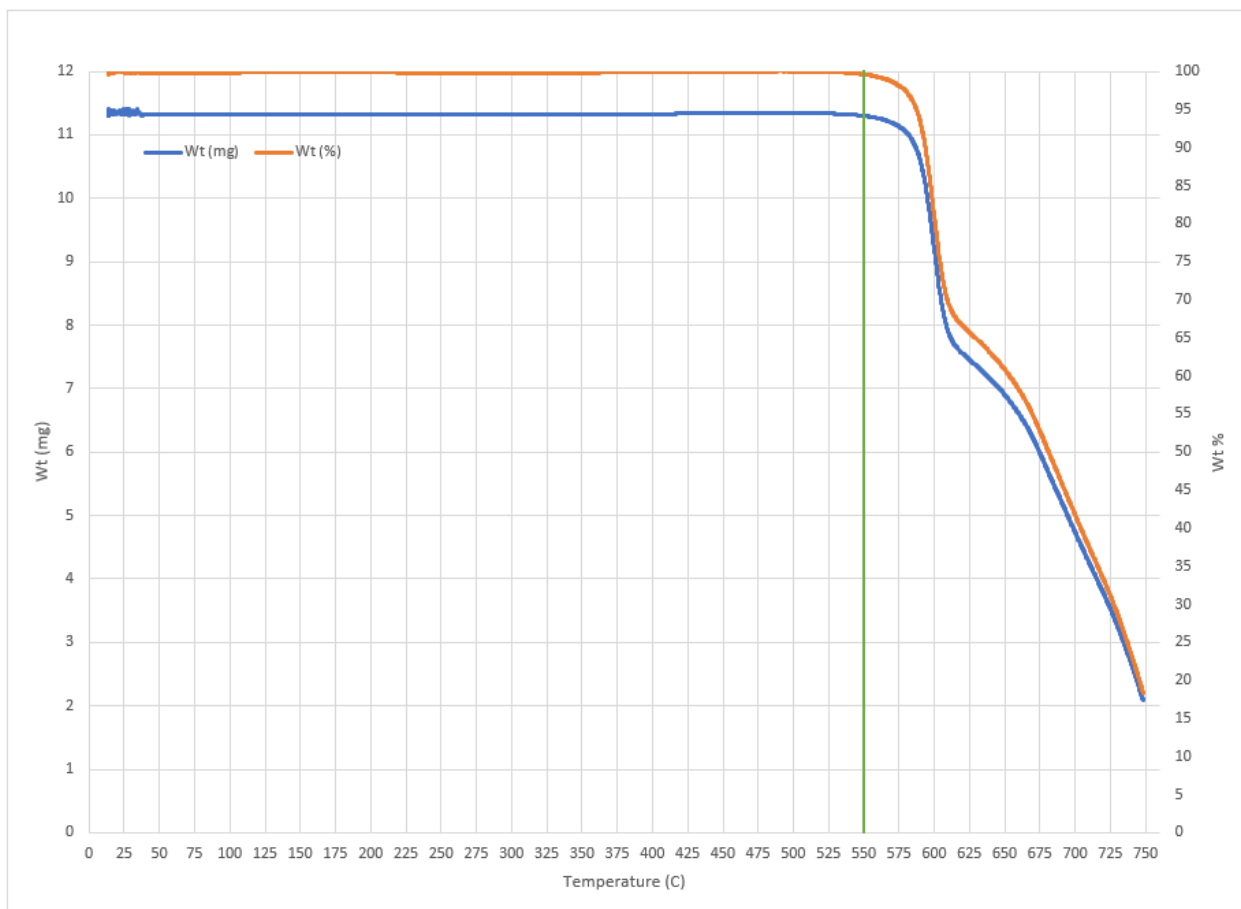


Figure 12. Graph plotting weight and weight% vs. temperature from temperature ramp TGA at 10°C/min.

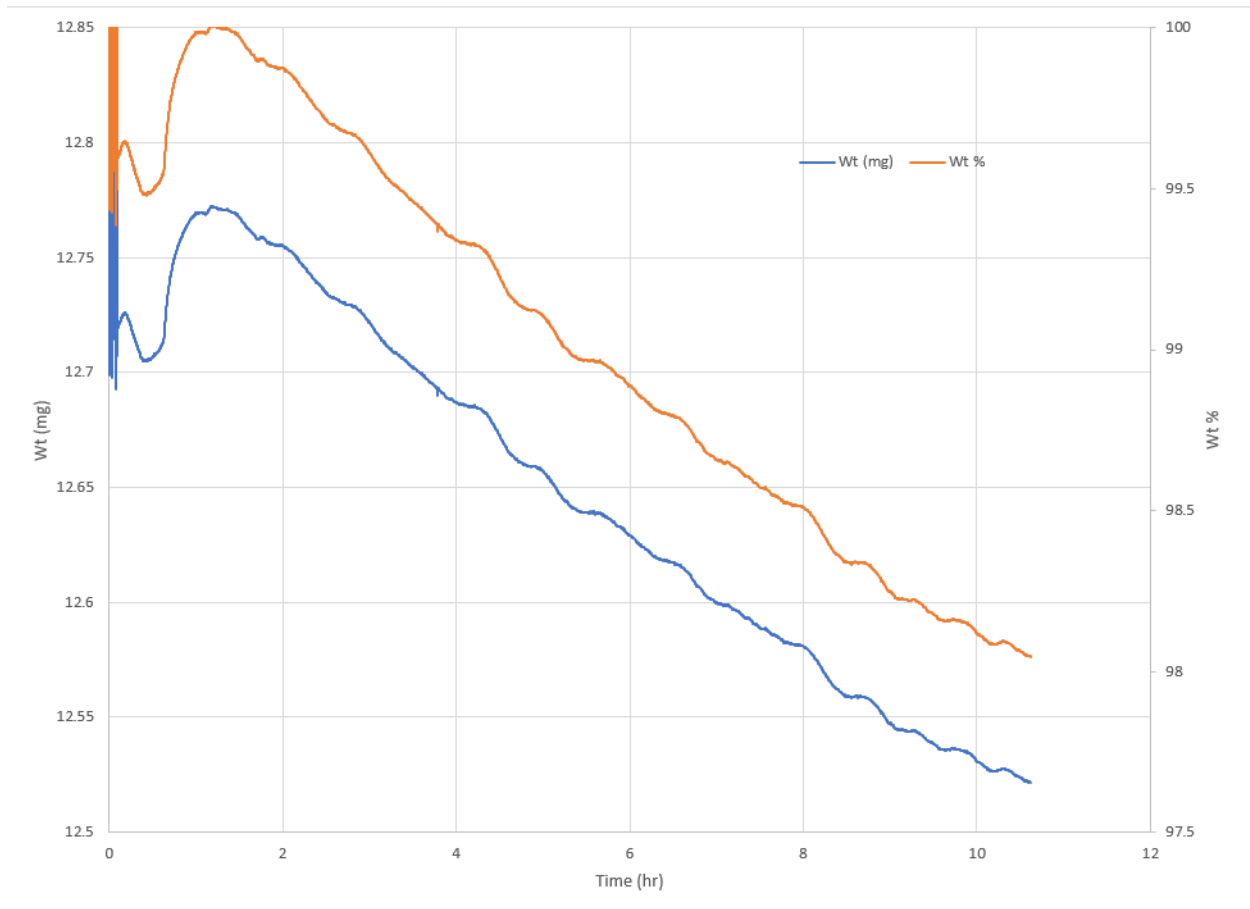


Figure 13. Graph plotting weight and weight% vs. time from the isothermal hold TGA at 400°C.

### 2.1.2 Commingled carbon fiber

As the name ‘commingled carbon fiber’ suggests, the fiber tow proposed to be used contains a mix of two different materials (see Figure 14). Since the polymer used as the matrix material was PEEK, carbon fiber commingled with PEEK fiber was proposed for this study. Commingled fibers were proposed to be used to improve the impregnation of matrix polymer into the carbon fiber, thus improving the fiber pull out force.

Comfil 57C-PEEK-1400 fiber (Gjern, Denmark), which consists of 12K carbon fiber with a linear density of 8000 dtex, was used. The specific grade of PEEK polymer was not specified by the manufacturer. The mix consisted of 49.3% volume of carbon fiber and remaining PEEK fibers. The commingled fiber has a consolidated linear density of 1400 tex and 1.53 g/cm<sup>3</sup> hybrid density.

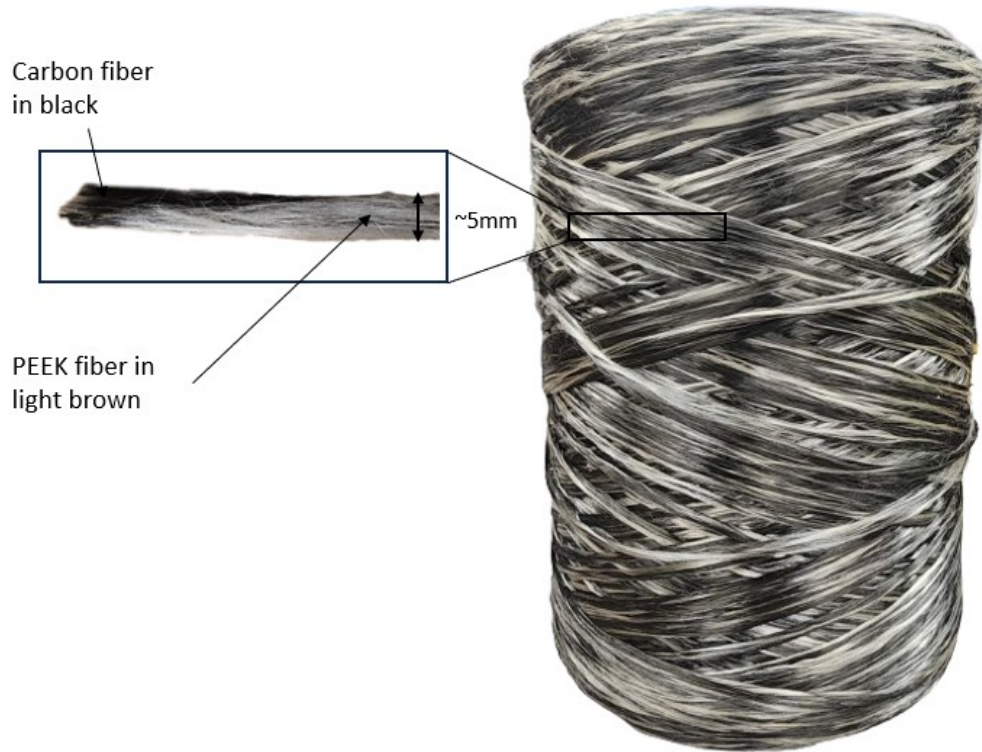


Figure 14. Commingled carbon fiber.

## 2.2 Fabrication system

### 2.2.1 Extruder

A single screw extruder RobotDigg SJ35-Desket-H extruder (RobotDigg Equip Makers, Shanghai, China) was used to carry out the FGF printing of PEEK. It is capable of max screw speed of 20 RPM. The screw has the same contour throughout its length as shown in Figure 15. The extruder has dimensions as mentioned in Table 5. Four heaters were used to heat the barrel as specified in Figure 16. Four different PT-1000 resistance temperature detectors (RTD) were used to monitor the temperature. The barrel was heated in three different zones:

- Zone 1: The feeding section was maintained at 150°C. Heat was conducted from the metering section and cooled using a DC fan to maintain the temperature.
- Zone 2: The transport, melting and mixing zone is where pellets melt, coalesce, and turn into a molten state. The temperature is taken as an input parameter for the design of experiments study.

- Zone 3: The nozzle is the final section where the molten material is expelled through a circular cross-section. The temperature here is also taken as an input parameter for the design of experiments study.

For the set of experiments with PEEK, the standard nozzle provided by the manufacturer was modified to increase the nozzle size from 2.8mm to 4mm to achieve a higher material throughput. Additionally, a 200W cartridge heater was installed to maintain the required temperature as shown in Figure 16. The length of the barrel section of the extruder was insulated with 1.5” thick fiberglass insulation sheet with an R value of 5.8.

Table 5. Dimension of SJ-35 extruder.

Parameter	Value	Unit
Barrel inner diameter	35	mm
Barrel length	280	mm
Length to diameter ratio	8	
Net weight	20	kg
Motor rated torque	1.2	Nm
Gear ratio (Motor : Screw)	50	
Rated motor RPM	1000	RPM

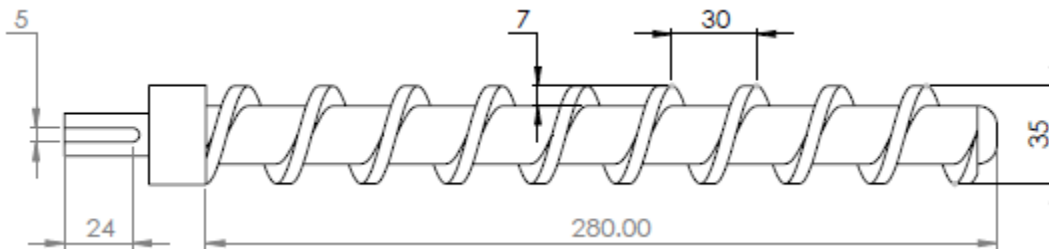


Figure 15. Screw geometry.

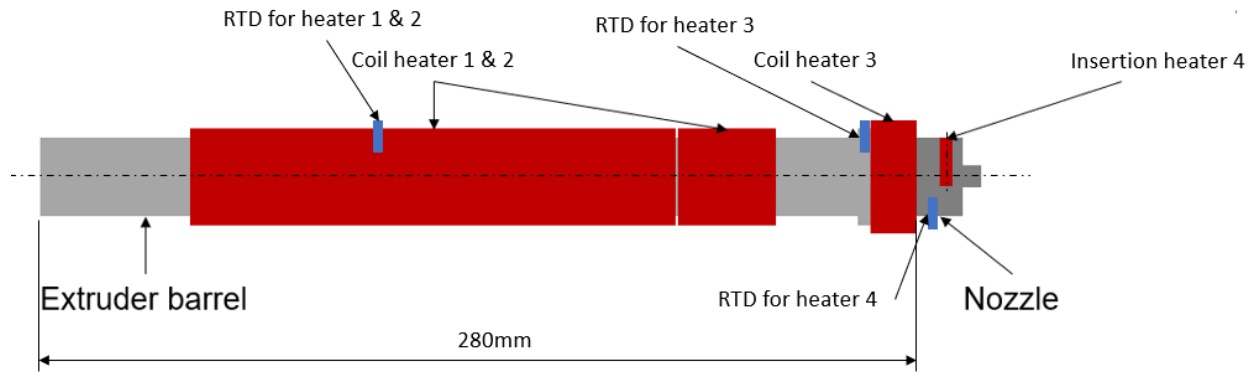


Figure 16. Schematic of extruder barrel.

## 2.2.2 Manipulator

Section describes the two-manipulator setup used for the extruder. The gantry system shown in Figure 17 was used for the DoE study and six-axis robotic arm for the subsequent experiments.

### 2.2.2.1 Three-axis cartesian gantry system

For the pilot testing of the capability of extruder to print with PEEK, a three-axis cartesian gantry (FUYU Automation, Chengdu City, China) was used to move the extruder in cartesian coordinates. The gantry was driven using NEMA 42 stepper motors. The structure of the gantry was built using 3" x 3" aluminum extrusions. Detailed specifications of the gantry system are listed in Table 6.



Figure 17. Three-axis cartesian gantry.

Table 6. Specifications of the gantry.

Parameter	Value	Unit
Range of motion, X-axis	1000	mm
Range of motion, Y-axis	1000	mm
Range of motion, Z-axis	500	mm
Positional repeatability	50	$\mu\text{m}$
Load capacity, Z-axis	70	kg
Load capacity, Y-axis	200	kg
Load capacity, X-axis	120	kg
Rated velocity, Z-axis	60	mm/s
Rated velocity, Y-axis	60	mm/s
Rated velocity, X-axis	60	mm/s

### 2.2.2.2 Robotic system

For the set of experiments #2, the extruder was mounted on a Motoman GP50 (Yaskawa, Miamisburg, OH, USA) six-axis robotic arm. The robot has a 50kg payload capacity. The robot has a reach of 2000mm x 2000mm x 3500mm in the X, Y, Z axes, respectively. Physical specifications of the robot are listed in Table 7.

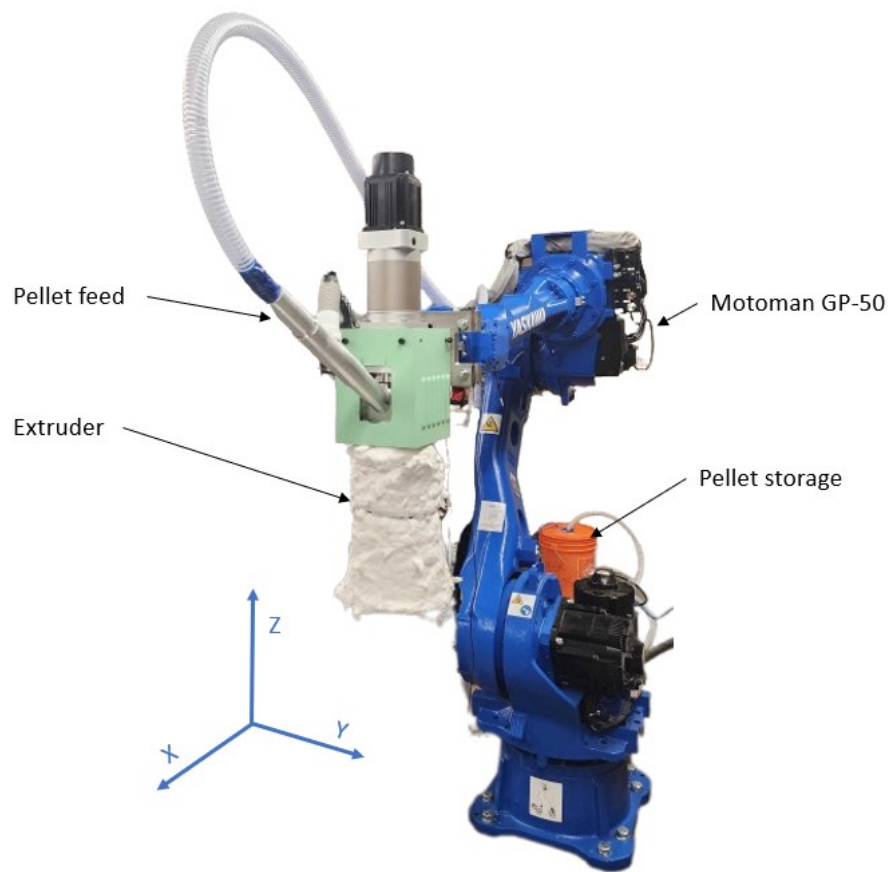


Figure 18. Robotic printing system.

Table 7. Specification of robotic arm.

Parameter	Value	Unit
Range of motion, X-axis	2000	mm
Range of motion, Y-axis	2000	mm
Range of motion, Z-axis	3500	mm
Repeatability of end joint	30	$\mu\text{m}$
Load capacity of end joint	50	kg
Rated velocity of end joint	50	m/s

### 2.2.3 Print bed

The print surface was manufactured out of a 0.4" thick AISI 304 stainless steel plate. For the purposes of the DoE study, a 356mm x 356mm sized bed was fabricated as shown in Figure 19. The surface was heated using a 1440W silicone heater pad of size 305mm x 305mm, capable of heating the surface up to 250°C. The temperature of the heated bed was controlled using a PT-1000 RTD sensor embedded into the thickness of the bed material.

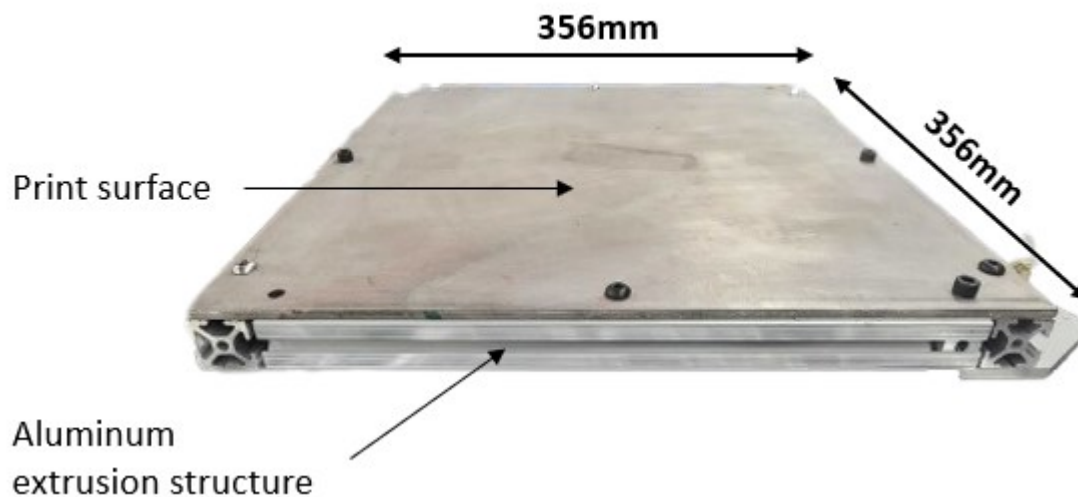


Figure 19. Heated print bed.

The print bed was leveled manually using the levelling pad supporting the structure. Additionally, a nano polymer adhesive (Vision Minor, Irvine, CA, USA) was occasionally applied on the print surface to improve the bed adhesion with PEEK.

#### 2.2.4 Heating system

Since PEEK polymer was printed at temperatures above 360°C, ambient conditions had to be controlled to prevent warping due to uneven cooling. In order to control the ambient temperature, infrared heaters were used. Three 750W infrared heaters with a heating element length of 19" were placed at 120° with respect to each other as shown in Figure 20. The heaters were controlled using IR camera Xi 400 (Optris, Berlin, Germany) that was reading the temperature of the material extruder on the print bed. Based on the temperature reading, the power to the IR heaters was modulated.

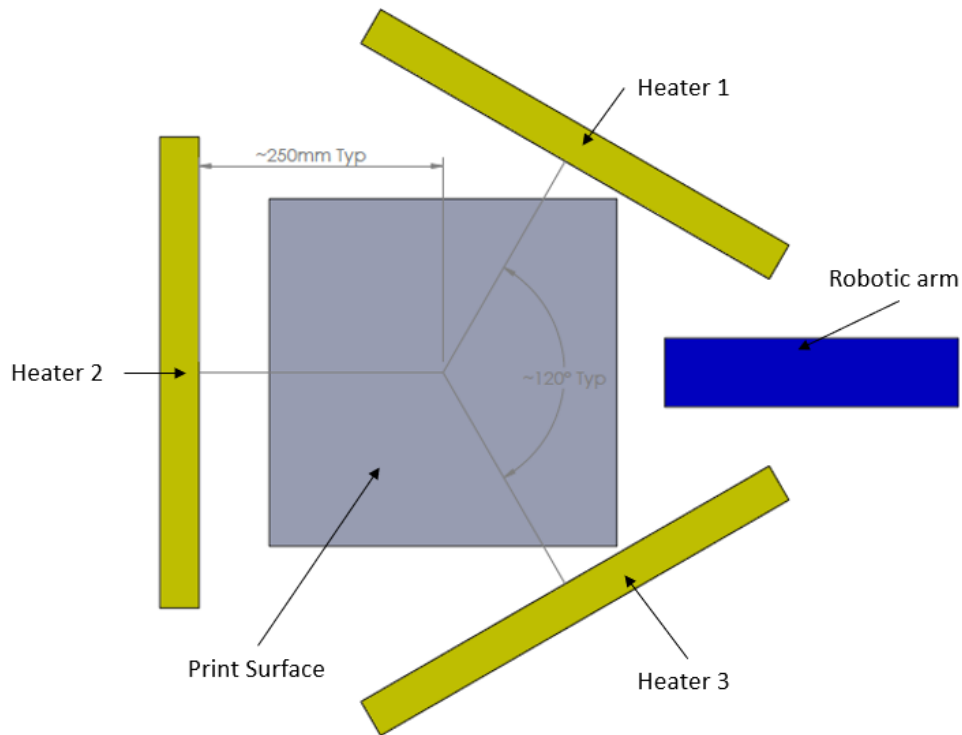


Figure 20. Schematic of IR heater setup.

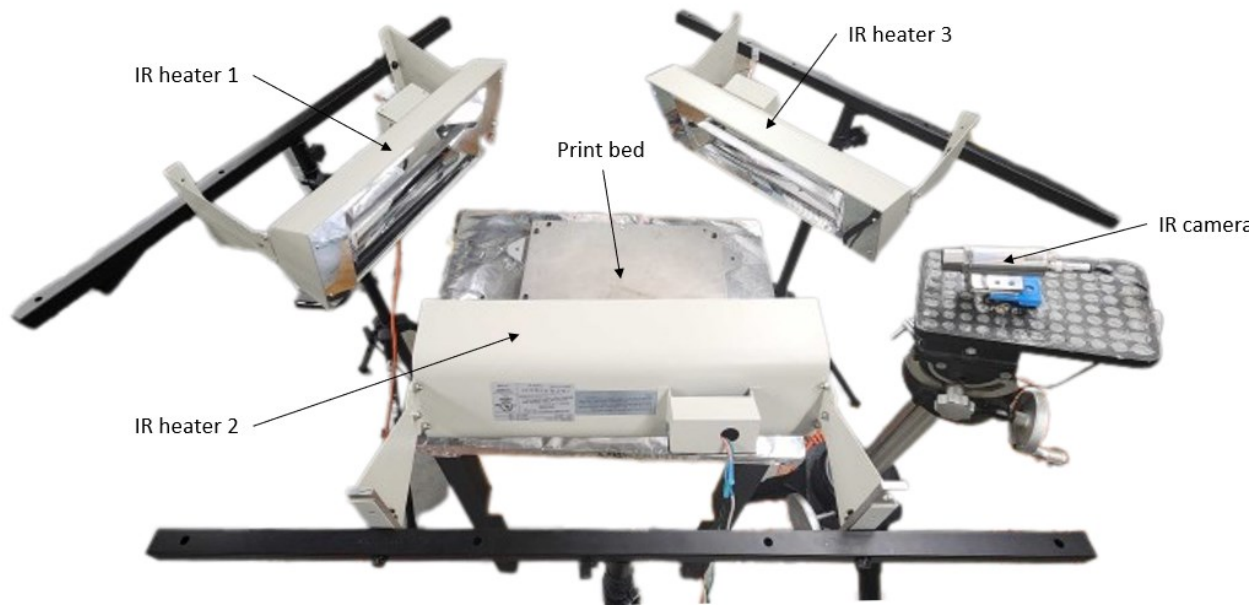


Figure 21. IR heater setup.

### 2.2.5 Pellet feeding system

PEEK pellets had to be transported from storage unit to the extruder while printing. The transport had to be automated based on the material intake rate of the extruder. Following approaches were considered for feeding pellets:

- Pneumatic pellet feeding
- Gravity feeding
- Vibratory pellet feeding

The feeding system was selected based on a decision matrix. Parameters influencing the manufacturing, installation, and usage of the feeding system were ranked on a scale of 1 to 10 with 10 being most favorable based on the research carried out. Based on the score from the decision matrix, pneumatic based pellet feeding system was selected.

Table 8. Decision matrix for pellet feeding system.

Parameter	Pneumatic based feeder	Gravity hopper	Vibratory feeder
Cost	10	5	2
Ease of design	7	10	5
Complex machinery	7	10	2
Ease of installation	10	5	7
Easy of manufacturing	10	5	2
Infrastructure requirement	2	5	10
Ease of pellet refilling	10	2	10
Total score	56	42	38

The pneumatic pellet feeding system was configured based on the compressed air supply available at the laboratory. A venturi-based system was used to create a suction at the pellet pick up point, and pressurized air transports the pellets to the deposition point. Figure 22 illustrates the basic workings of the system.

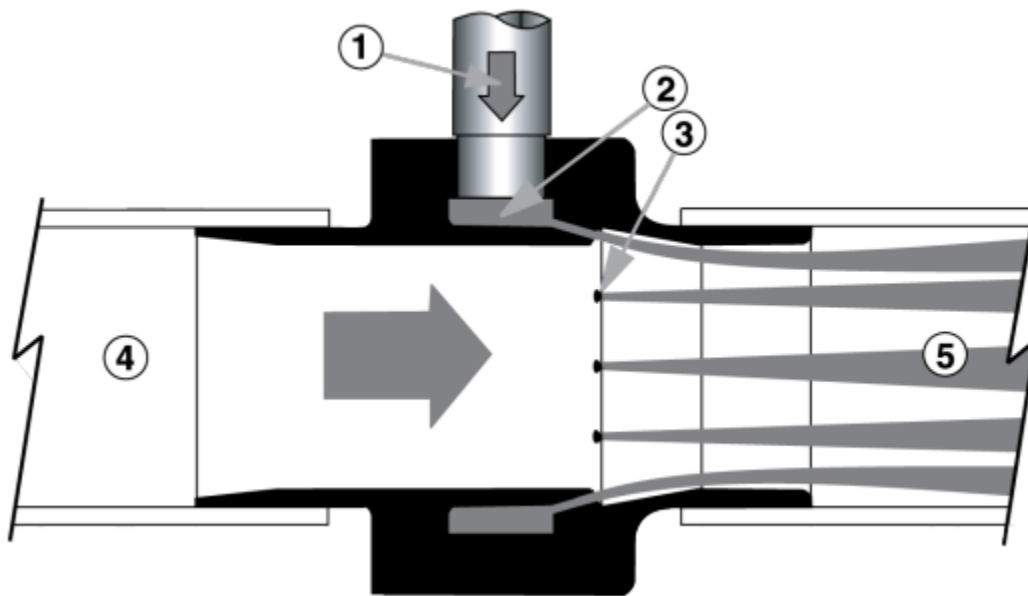


Figure 22. Compressed air flows through the inlet ① into an annular plenum chamber②. It is then injected into the throat through directed nozzles ③. These jets of air create a vacuum at the intake ④ which draws material in and accelerates it through it ⑤ at long vertical or horizontal distances [124].

Model# 6080 Line Vac (Exair, Cincinnati, Ohio, USA) shown in Figure 23 was used for the application. It has a ¼” NPT inlet for pressurized air and a ¾” diameter material flow cross-section. As per the specification sheet of the product, it creates a suction pressure of -18kPa from a 550kPa supply of air [125].



Figure 23. Model# 6080 Line Vac product used in the feeding system [6].

The product was analytically validated for its effectiveness using the PneuCalc software (Hatch, Mississauga, ON, Canada). The software provided the required pressure ( $P_1$ ) to convey the pellets at a maximum rate of 25kg/hr (10 times the maximum extrusion rate of the extruder) according to Equation (1). The components for the feeding system were configured to transfer the material over a tube of 8m split into three sections.

- Section 1 with a length of 0.5m vertically aligned from the material pick-up point to the Line Vac unit. This section operates under the vacuum pressure produced by the unit.
- Section 2 with a length of 3m of the horizontal section from the Line Vac unit to the base of the robot. This section transports material with the help of pressurized air.
- Section 3 with a length of 4.5m routed along the robotic arm to the extruders feeding zone. This section was taken as vertically aligned for the pneumatic calculations as this condition mimics the robot at its maximum extended position along the Z-axis. Pressurized air transports material through this section as well.

$$(P_1 - P_2) - (F_{fw}L - F_{sw}L) - \rho_s L(1 - \epsilon)g \sin\theta - \rho_f L \epsilon \sin\theta = \frac{\epsilon \rho_f U_f^2 + (1 - \epsilon) \rho_s U_s^2}{2} \quad (1)$$

where  $P_1$  is the pressure (kPa) used to drive the material, i.e., vacuum pressure in section 1, or air pressure in section 2 and 3;  $P_2$  is the pressure drop (kPa) at the extruder's feeding zone;  $F_{fw}$  is the friction factor between conveying tube wall and air;  $F_{sw}$  is the friction factor between conveying tube wall and PEEK pellets;  $\rho_s$  and  $\rho_f$  are the density of PEEK (1300kg/m<sup>3</sup>) and air (16kg/m<sup>3</sup>), respectively;  $L$  is the length of conveying tube (5m);  $U_f$  and  $U_s$  are the velocity (m/s) of air and pellets (m/s) calculated via the PneuCalc software, respectively;  $\epsilon$  is the void fraction at a cross-section of conveying tube;  $g$  is acceleration due to gravity (9.81 m/s<sup>2</sup>); and  $\theta$  is the angle of inclination of the conveying tube with respect to the horizontal plane (i.e., 90° for the vertical section and 0° for horizontal tube sections).

The friction terms were negligible compared to the head losses as the inner surface of the tubing was smooth. These terms were neglected from the calculation.

The calculations showed that an air pressure of 14kPa was needed for material transport through section 2 and 3 and a vacuum pressure of 1.7kPa for section 1. Given that the configured components can deliver air pressure of up to 550kPa and create a vacuum pressure of 18kPa, they are well-suited for the application, surpassing the requirements by nearly a factor of 10. A pressure regulator was used in the final system to control the rate of material flow, and a capacitive sensor in conjunction with a normally closed 5/2 solenoid valve was used to maintain the frequency of filling the feeding section at the extruder end.

# Chapter 3 Process parameter optimization for FGF of PEEK

Details discussed in this chapter have been presented at The American Society for Testing and Materials (ASTM) International Conference on Advanced Manufacturing 2023, Washington DC, USA, October 31 – November 3, 2023.

This chapter outlines the methodology employed to enhance the printing parameters for the FGF process, focusing on achieving minimal surface deformity and near-zero porosity when 3D printing PEEK polymer components. A mechanical characterization to determine the inter-bead adhesion strength of printed parts was conducted.

## 3.1 Parameters influencing FGF

Based on the literature review presented in Section 1.2.2, various parameters affecting the FGF process were identified. From this list, a subset of key parameters was shortlisted to be optimized based on the available resources. Table 9 provides an overview of the key parameters affecting the FGF process and the extent to which the experimental setup can accommodate variations within these parameters.

For all the experiments, the barrel and nozzle temperature were maintained equal in order to reduce the parameters for the DoE study. So further on, the barrel and nozzle temperature will be referred to as the extrudate temperature. Values used for parameters for each experiment are listed in the respective sections.

Table 9. Range of controlled process parameters used for various experiments.

Parameter	Upper limit	Lower limit
Barrel temperature °C	400	Room temperature
Nozzle temperature °C	400	Room temperature
Bed temperature °C	250	Room temperature
Scanning velocity mm/sec	50	0
Screw motor speed (RPM)	1000	0
Nozzle diameter (mm)	4	
Layer height (% of nozzle diameter)	60	80

### 3.2 Methodology

In order to optimize the parameters to print parts with minimal porosity and surface deformity, a DoE study was conducted. As the first step in evaluating the extruder, its mass flow rate was measured to analyze repeatability and stability. The mass flow rate at different screw motor speeds and extrudate temperatures was measured and formulated using R-square regression to form an equation relating mass flow rate to screw motor speed at different temperatures. The Excel software was used for the regression analysis (Microsoft, Redmond, WA, USA). The measurement of the mass flow was done by running the extruder at a particular screw motor speed for 10sec. Then, the extrudate was weighed. Five samples at each screw motor speed and temperature were taken and averaged as the mass flow rate for the regression analysis. The screw motor speed refers to the screw motor RPM. The parameters used for the experiment can be found in Table 10.

Table 10. Parameter levels for mass flow rate measurement.

Parameters	Levels
Temperature	360, 390
Screw motor RPM	300, 500, 700, 900

In order to eliminate the scanning velocity of the gantry as a parameter for the DoE study, Equation (2) taken from Hu et.al. [127] used to calculate the scanning velocity based on extrusion velocity, layer height and nozzle diameter.

$$V_{xy} = V_e \frac{\pi D^2}{4hD + \pi h^2} \quad (2)$$

where  $V_{xy}$  is the scanning velocity (mm/sec),  $V_e$  the extrusion velocity (mm/sec) calculated from the mass flow rate,  $D$  the nozzle diameter (mm), and  $h$  the layer height (mm).

Once the mass flow rate versus screw motor speed relation and the corresponding scanning velocity was established, the width of a raster had to be calculated to help define the degree of overlap between the rasters. Thus, a DoE study was conducted to measure the variation of bead width with varying extrudate temperature, layer height and screw motor speed. A full factorial design was conducted, and results were analyzed using the Minitab software (Lock Haven, PA, USA) to form a relation between the parameters. The various levels selected for the DoE study are shown in Table 11. The layer height was included as a percentage of nozzle diameter, which was 4mm for this particular experiment.

Table 11. DoE for determining optimum bead width.

Sl.No.	Parameters	Level -1	Level 0	Level +1
O/P	Bead Width (mm)	Response variable		
A	Extrudate temperature (°C)	360		390
B	Layer height/Nozzle diameter (h/D)	0.6	0.7	0.8
C	Screw motor speed (RPM)	200	500	800

For the full factorial design, 36 samples were printed for the analysis, that is two samples per set of parameters. The samples featured a single raster of length 150mm, and the width was measured at 75mm and 125mm lengths of the bead. The two readings were averaged and served as input for the statistical analysis.

Minitab software also provides a regression analysis, which was employed to formulate a relation between bead width and the parameters mentioned in Table 11. The formulated R-square regression equation was further used to calculate the bead width for a set of printing parameters.

With the above-mentioned experiments and formulations, the required data for optimizing the process parameters for printing parts with minimal porosity and surface non-uniformity were obtained. Layer height, degree of overlap between adjacent beads, and screw motor speed were the parameters considered to be optimized. For this purpose, a face-centered central composite DoE study was conducted. Data obtained from the experimental runs were analyzed with the Minitab software to produce a range of optimal printing parameters. The parameters are shown in Table 12, where h and D denote the layer height in mm and nozzle diameter in mm, respectively.

Table 12. Printing parameters are selected to optimize for minimize inter bead porosity and maximize surface uniformity.

Sl.No.	Input Parameters	Level -1	Level 0	Level +1
A	Layer height/Nozzle diameter (h/D)	0.6	0.7	0.8
B	Overlap % between beads (mm)	12	17	22
C	Screw motor speed (RPM)	400	600	800
O/P1	Inter bead porosity (volume %)	Response variable 1		
O/P2	Surface deformity (mm)	Response variable 2		

Parameters such as the layer height were entered as a ratio of layer height to nozzle diameter and screw motor speed as the screw motor RPM. The surface non-uniformity was measured in terms of difference

between the maximum and minimum height points on the top face of printed samples. Note that the bottom face was smooth due to the direct deposition over smooth bed surface.

For the experiment, samples of four layers and four rasters were printed and analyzed for porosity and surface deformity. Samples with length of 200mm were printed as shown in Figure 24 with different combination of the parameters as listed in Table 13. Layers were printed with length decrement of 16.7mm to avoid printing over warped section.

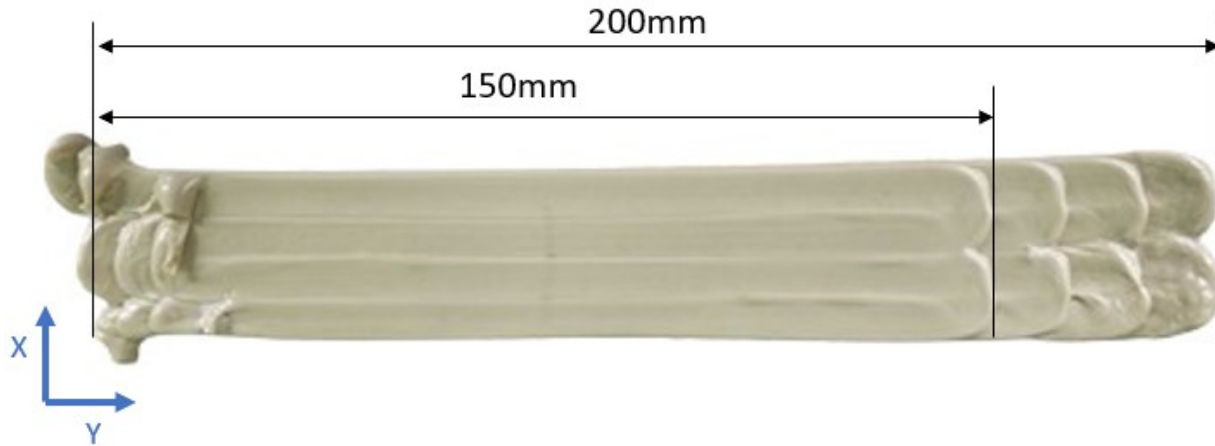


Figure 24. Sample printed for DoE.

Table 13. Experimental runs for DoE to minimize inter-bead porosity and maximize surface uniformity.

Runs	Screw motor RPM	h/D	Overlap%
1	400	0.6	12
2	800	0.6	12
3	400	0.8	12
4	800	0.8	12
5	400	0.6	22
6	800	0.6	22
7	400	0.8	22
8	800	0.8	22
9	400	0.7	17
10	800	0.7	17
11	600	0.6	17
12	600	0.8	17
13	600	0.7	12
14	600	0.7	22
15	600	0.7	17
16	600	0.7	17
17	600	0.7	17
18	600	0.7	17
19	600	0.7	17
20	600	0.7	17

For the measurement of the surface uniformity, a laser profilometer, together with the Pro2 Navigator software (SICK, Minneapolis, MN, USA) with a 25 $\mu$ m repeatability was mounted on a three-axis gantry. Four measurements at intervals of 25mm along the Y-axis were taken as shown in Figure 25. The relative difference in height from the tallest point to the shortest point was recorded as shown in Figure 26. This surface non-uniformity is created either by an excessive overlap between parts leading to over extrusion on to the previous raster or vice versa where sufficient overlap was not achieved leading to deeper valleys between layers. Thus, an optimal range of parameters were to be obtained to minimize this non-uniformity.

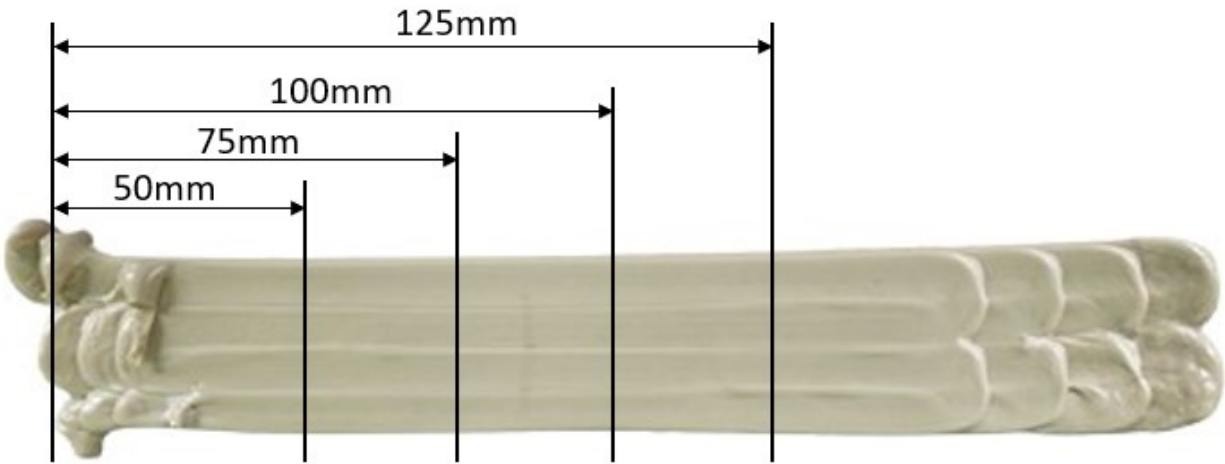


Figure 25. Point of measurements for surface deformity.

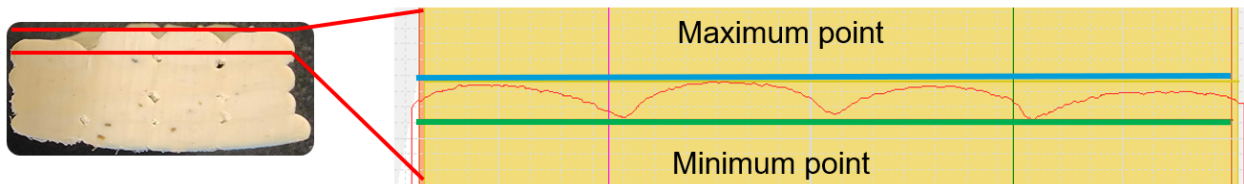


Figure 26. Measurement of maximum and minimum point of top face of sample.

For measuring inter-bead porosity, the samples were cut across the X-Z plane to create cross-sections at positions of 75mm, 100mm and 125mm along the Y-axis. Samples were cut using a waterjet cutting machine in order to avoid debris covering the pores. The cross-section was photographed under an A3RDF50 optical microscope camera (OMAX, Kent, Washington, USA), and the relative area of void to cross-section area was measured using the IC Measure software (The Imaging Source, Charlotte, NC, USA). Figure 27 shows the cross-section of a sample magnified under an optical microscope.

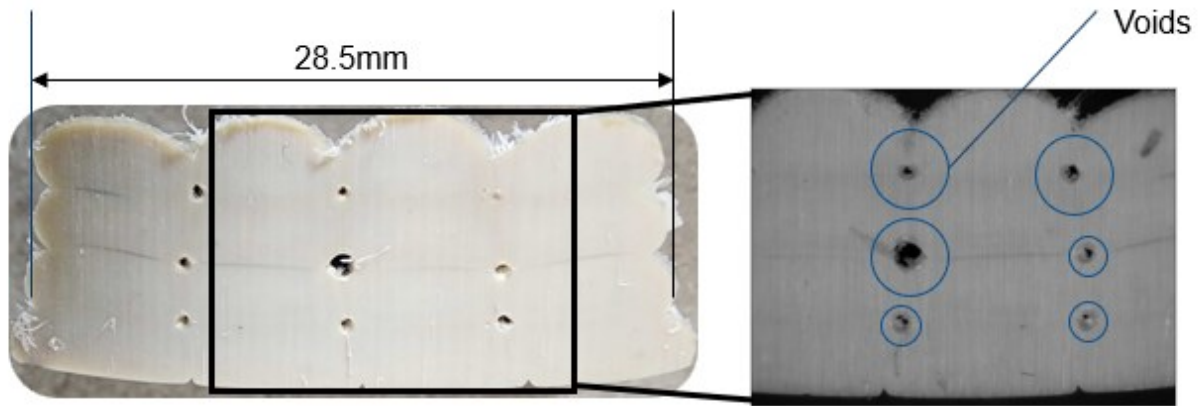


Figure 27. Cross-section of sample magnified under optical microscope.

The Minitab software was used for the response optimization of data collected from the experiments. The goal was set to minimize both the response variables with a target of zero for porosity and 0.99mm for surface uniformity, which was the least measured surface deformity. The importance factor was set to unity for both the response variables. Porosity and surface uniformity were given an equal weighting of unity. The larger the weighting, the higher the emphasis on the predicted response closer to the specified target values [134].

### 3.3 Challenges in 3D printing PEEK

During the initial stages of conducting the experiments, various deformities were observed in the 3D printed samples. Aspects of developing the high-performance polymer additive manufacturing system involved addressing and resolving these problems.

#### 3.3.1 Bed adhesion

Different bed materials were tested, like aluminum 6061-T6 and stainless steel 304, to check the adhesion of PEEK polymer with the bed while printing. A range of bed temperatures ranging from 100°C to 250°C were explored to find the optimal bed temperature for PEEK adhesion with each of the prior mentioned bed materials. The PEEK material started sticking to the bed above 150°C. But once the layer cools down it starts separating from the bed which does not provide sufficient time for printing subsequent layer for support (see Figure 28).

It is reported that the adhesion of PEEK and metal was highly influenced by the wetting characteristics of the metals [128] and that different microscale surface structures could change the wettability of metals,

especially generating superhydrophobic surfaces [129]. Since PEEK is a non-polar polymer, it will have enhanced adhesion to a hydrophobic surface [130].



Figure 28. Part separating from the print bed due to poor bed adhesion.

In order to create the laser texturing on the selected AISI 304 stainless steel print surface, FabLight FL4500 laser cutter was used (FabLight, Oakland, CA, USA). The machine employs a 4500W IPG pulsed fiber laser as the heat source. The print surface was textured with a peak and valley pattern by running the laser in parallel lines on the printed surface. Since the manufacturer reported a kerf value of 0.127mm, parallel lines were spaced at 0.250mm apart. Six engrave passes (the machine was running an engrave setting for 0.4" thick AISI304 material) with same settings were done on the print surface. The resulting surface deformity was measured using the profilometer; the resulting profile is shown in Figure 29. A surface of average maximum height ( $R_y$ ) of 0.37mm was obtained.

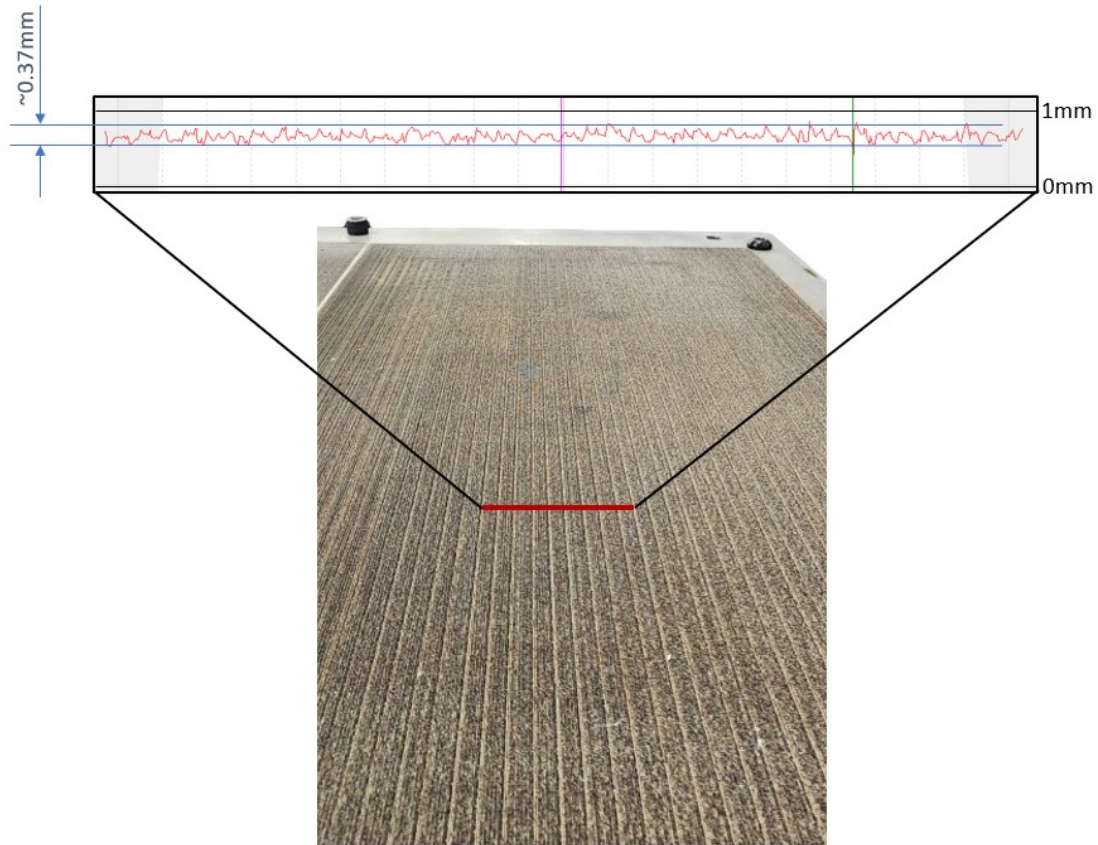


Figure 29. Laser textured AISI304 printing surface.

The print surface was heated and tested by printing a single rectangular layer and measuring the time it took for the print to separate from the bed on its own, thus disallowing subsequent layers from printing. Sufficient adhesion was found while testing at nearly 200°C to 220°C as the printed rectangle did not dislodge from the print bed on its own and allowed for printing subsequent layers. Adhesion with the bed was found even after the layer cooled down.

### 3.3.2 Material oozing from nozzle

Another major challenge was material oozing from the nozzle due to gravity. The material that occupied the conical section of the nozzle tends to flow down through the nozzle during downtime between prints. This reduced the print quality of the parts especially while switching between layers or the nozzle traversing to a location without extrusion. Additionally, the material that oozed out left a void in the nozzle leading to delayed material dispensing while starting prints. The figure below shows the severity of material oozing from the nozzle. Moreover, the material, if not cleared on time, would sometimes solidify and clog the nozzle.



Figure 30. Material oozing from the nozzle.

As the objective was to print PEEK and optimize the parameters associated with PEEK printing, a special mechanism was not put in place to prevent oozing. But special measures were taken while printing, like timely cleaning of the nozzle, cleaning the nozzle tip between each layer, and printing an extra 100mm raster for priming the nozzle before printing the actual part. These measures reduced the effects of material oozing on the part, improving print quality and dimensional accuracy.

While designing a new nozzle for continuous fiber reinforced polymer printing, the issue of material oozing was considered and the vertical section through which molten polymer flows was minimized to reduce the effect of gravity on the molten polymer, thus reducing material oozing while printing. More details on the nozzle design for continuous fiber reinforced polymer printing can be found in Chapter 4.

### 3.3.3 Delamination

Since PEEK is a high temperature polymer that melts at 343°C, the effect of ambient temperature had a significant effect on interlayer adhesion. When printed at room temperature, the layers at times exhibited spontaneous delamination as shown in Figure 31. To prevent this, a controlled environment around the printed part was required.

Because the project goal was to print at a large scale with a robotic arm, it was impractical to enclose the entire print area with an environmental chamber suitable for printing PEEK. This meant that the deposited material had to be heated in a targeted manner. Infrared heaters were installed for this purpose directed at the print bed as explained in Section 2.2.4. The IR heating system was validated for its effectiveness by measuring the cooling rate. Temperature readings were taken via an IR camera. Molten PEEK at 370°C equivalent to a five-layer height (15mm) was deposited onto the heated print bed and temperature readings

were recorded over a period of 4 minutes. Table 14 lists the temperature readings recorded by the IR camera at an interval of 1min. The IR heaters proved effective since at the end of 4 minutes the PEEK material subjected to IR radiation was at an average of temperature of 237°C while the material subject to room temperature was at 185°C.



Figure 31. Delaminated layers after printing.

Table 14 . Temperature readings highlighting the effect of IR heating system.

Temperature readings from IR camera		
Time	Without IR heater	With 3 IR heaters
min	°C	°C
1	273	287
2	247	280
3	214	258
4	185	237

### 3.3.4 Warping of printed parts

PEEK experiences a high shrinkage during cooldown [130]. As the scale of the printed bead is approximately 10-time larger than in conventional FFF printers [1], the shrinkage also tends to increase with the increase in the wall thickness. PEEK is a semi-crystalline polymer, and hence, crystallization is also a significant factor that causes shrinkage. The rate of crystallization in polymers tends to define the rate of shrinkage [103], see Figure 32. Due to this property, the parts warp while cooling down after printing. Significant warping was experienced in the preliminary stages of the project as seen in Figure 33. In order to mitigate the warping of prints, the bed adhesion was improved through the above-mentioned methods.

This allowed the part to cool in place and not freely change shape while cooling down. The addition of IR heaters also aided in reducing warping.

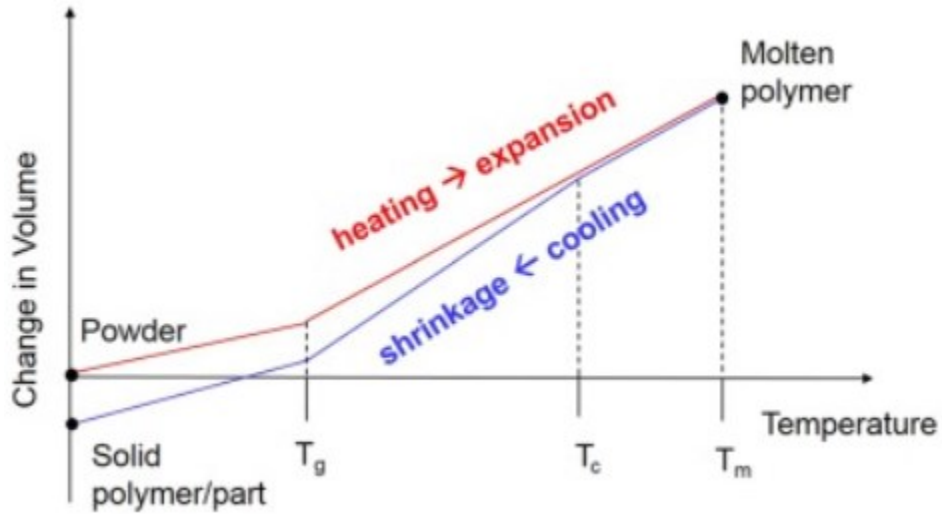


Figure 32 .Shrinkage characteristics of semi-crystalline polymers due to temperature change [103].



Figure 33. Printed parts warped from uneven cooling of material.

## 3.4 Results and Discussion

### 3.4.1 Mass flow rate measurement

Experiments were conducted at extrudate temperatures of 360°C and 390°C to understand the effect of temperature on flow rate from the extruder. Table 15 and 16 show the mass of the extrudate over a period of 10 seconds at 360°C and 390°C extrudate temperature, respectively.

Table 15. Flow rate measurement at an extrudate temperature of 360°C.

<b>RPM</b>	<b>Trial 1</b>	<b>Trial 2</b>	<b>Trial 3</b>	<b>Trial 4</b>	<b>Trial 5</b>	<b>Average</b>	<b>Std Dev</b>
<b>/min</b>	<b>kg/hr</b>						
300	0.65	0.73	0.72	0.71	0.70	0.705	0.032
500	1.19	1.24	1.19	1.22	1.25	1.216	0.028
700	1.85	1.64	1.79	1.75	1.64	1.733	0.092
900	2.23	2.18	2.34	2.17	2.20	2.224	0.067

Table 16. Flow rate measurement at an extrudate temperature of 390°C.

<b>RPM</b>	<b>Trial 1</b>	<b>Trial 2</b>	<b>Trial 3</b>	<b>Trial 4</b>	<b>Trial 5</b>	<b>Average</b>	<b>Std Dev</b>
<b>/min</b>	<b>kg/hr</b>						
300	0.66	0.67	0.65	0.70	0.71	0.679	0.026
500	1.22	1.18	1.30	1.29	1.32	1.260	0.060
700	1.85	1.83	1.76	1.85	1.98	1.853	0.077
900	2.30	2.45	2.36	2.39	2.45	2.389	0.066

The averaged mass flow rates from Table 15 and Table 16 were plotted against the respective screw motor speeds and are shown in Figure 34. The maximum deviation of flow is within a band of 5%, which confirms the stability of flow rate from the extruder. This flow stability is comparable with those reported in technical literature [57,132,133]. Since the working range for the screw motor speed in subsequent DoE is 200 – 800RPM, the variation in flow rate at different temperatures is not significant as the variation lie within the error range of the measurements.

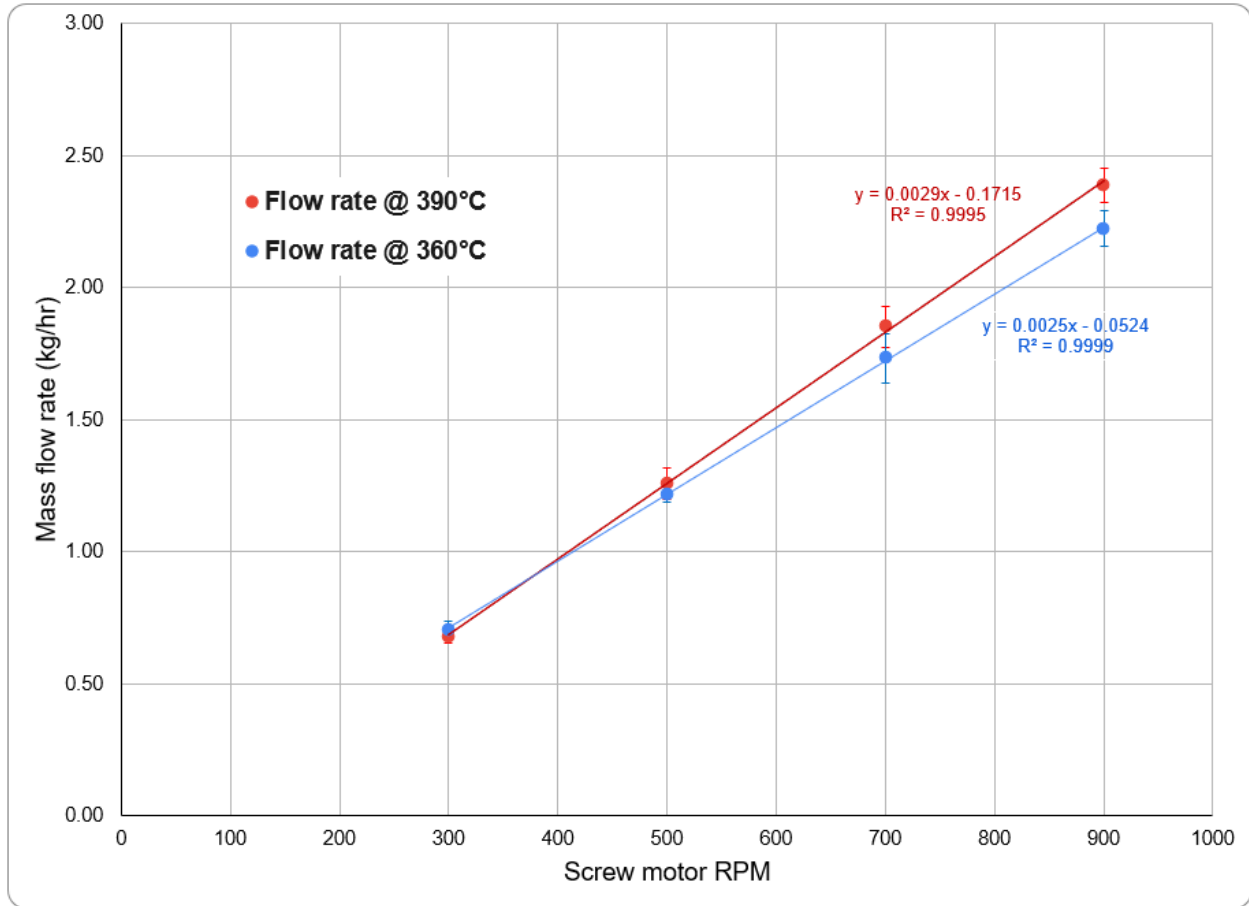


Figure 34. Plot of mass flow rate measured at different screw motor speed at 360°C and 390°C.

Data points in Figure 34 were fitted using linear R-squared fitting. An  $R^2$  value of 0.99 for both curves shows a linear increase in mass flow rate with a linear increase in screw motor speed. Equations were extracted for the  $R^2$  fitted lines for the respective temperature data relating mass flow rate with screw motor speed. Following are the equations obtained:

$$\text{For extrudate temperature of } 360^\circ\text{C: } MFR = 0.0025(RPM) - 0.0524 \quad (3)$$

$$\text{For extrudate temperature of } 390^\circ\text{C: } MFR = 0.0029(RPM) - 0.1715 \quad (4)$$

where  $MFR$  and  $RPM$  are the mass flow rate (kg/hr) and screw motor speed defined in terms of screw motor speed (RPM), respectively.

Based on Equations (3) and (4), the extrusion velocity (mm/sec) of the material was calculated using the material density and cross-sectional area of the nozzle tip. Extrusion velocity was further used to calculate the scanning velocity of the manipulator. These equations were used in the Python script to generate the GCODE for the custom experimental setup.

### 3.4.2 Bead width calculation

A regression equation correlating the parameters used for measuring the bead width as shown in Table 17 is given by Equation (5). The data shown in the table are plotted to understand the variation of bead width with changing parameters in Figure 35. The equation has an R-square fit of 98.13%, which provides an excellent fit for predicting the bead width for any set of parameters within the range of values used in the analysis. This ability to predict the bead width aids in calculating the overlap required for the printing parameters and in generating the GCODE files for printing parts rather than using manual adjustments.

Table 17. Bead width measured for the statistical analysis.

Run #	Temperature	h/D	Screw motor	Sample 1			Sample 2			Overall Avg	Std dev
				Bead Width @ 75mm	Bead Width @ 125mm	Avg 1	Bead Width @ 75mm	Bead Width @ 125mm	Avg 2		
	°C		RPM	mm	mm		mm	mm	mm	mm	mm
1	360	0.6	200	8.22	8.14	8.18	8.21	8.22	8.22	8.20	0.04
2	360	0.6	500	6.54	6.98	6.76	6.73	6.65	6.69	6.73	0.19
3	360	0.6	800	6.84	6.57	6.71	6.4	6.35	6.38	6.54	0.22
4	360	0.7	200	8.6	8.51	8.56	8.56	8.8	8.68	8.62	0.13
5	360	0.7	500	7.17	7.33	7.25	7.44	7.18	7.31	7.28	0.13
6	360	0.7	800	7.09	7.17	7.13	7.06	7.04	7.05	7.09	0.06
7	360	0.8	200	9.51	9.45	9.48	9.19	9.32	9.26	9.37	0.14
8	360	0.8	500	7.51	7.32	7.42	7.75	7.77	7.76	7.59	0.21
9	360	0.8	800	7.19	7.34	7.27	7.51	7.28	7.40	7.33	0.13
10	390	0.6	200	10.42	10.31	10.37	9.78	9.85	9.82	10.09	0.32
11	390	0.6	500	7.82	7.77	7.80	7.6	7.57	7.59	7.69	0.12
12	390	0.6	800	7.39	7.32	7.36	7.24	7.33	7.29	7.32	0.06
13	390	0.7	200	10.97	10.97	10.97	10.01	10.32	10.17	10.57	0.48
14	390	0.7	500	8.5	8.35	8.43	7.79	8.07	7.93	8.18	0.31
15	390	0.7	800	7.7	7.35	7.53	7.43	7.77	7.60	7.56	0.20
16	390	0.8	200	10.98	11.09	11.04	10.79	10.89	10.84	10.94	0.13
17	390	0.8	500	8.73	8.64	8.69	8.63	8.76	8.70	8.69	0.06
18	390	0.8	800	7.9	8.04	7.97	7.97	7.92	7.95	7.96	0.06

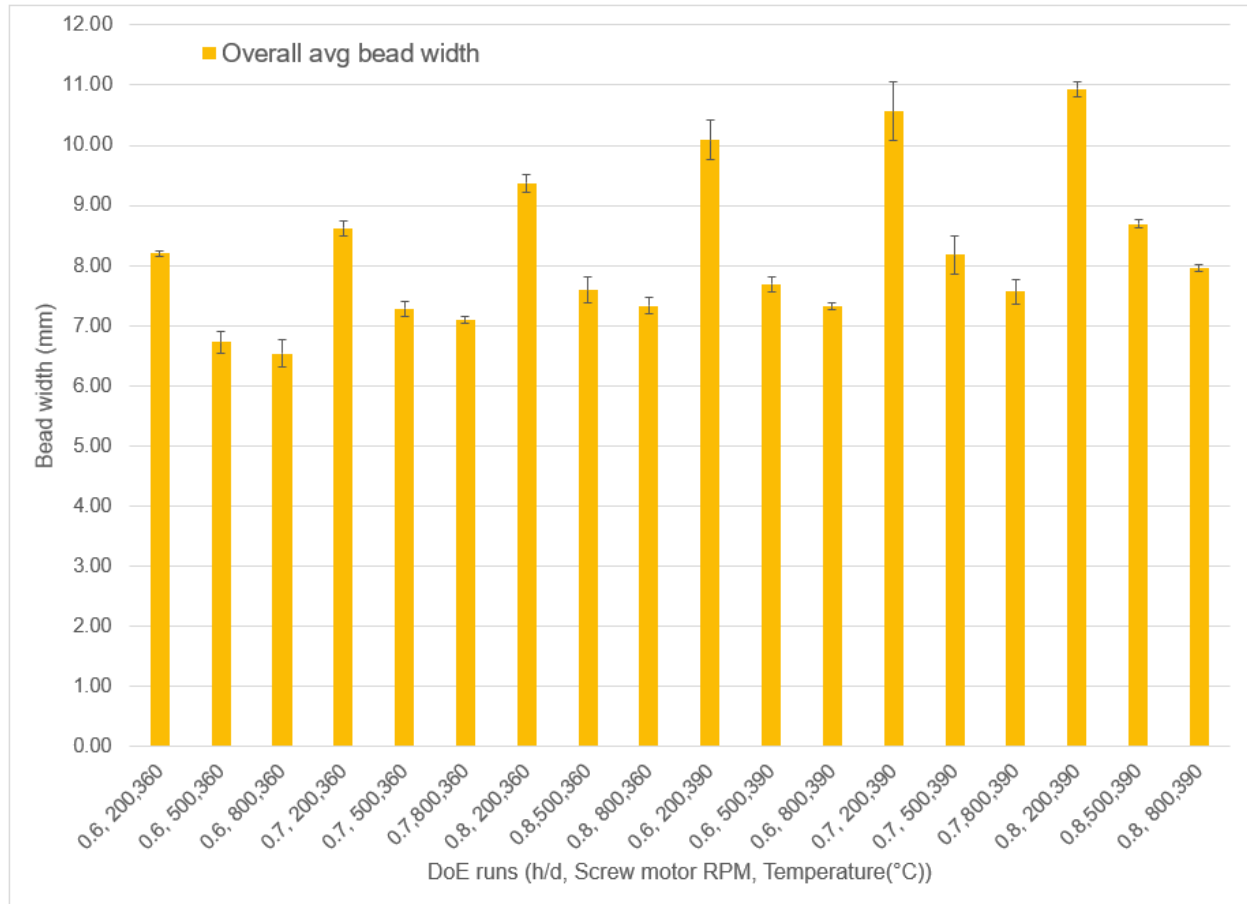


Figure 35. Plot of average bead width data from the DoE runs.

$$\begin{aligned}
 \text{Bead Width} = & -30.4 + 23.4 \left(\frac{h}{D}\right) + 0.0262 (RPM) + 0.1004 (T) - 1.31 \left(\frac{h}{D}\right)^2 \\
 & + 0.000009 (RPM)^2 - 0.0202 \left(\frac{h}{D}\right) (RPM) - 0.0424 \left(\frac{h}{D}\right) (T) \\
 & - 0.000098 (RPM) (T) + 0.000047 \left(\frac{h}{D}\right) (RPM) (T)
 \end{aligned} \quad (5)$$

Where  $\left(\frac{h}{D}\right)$  is the ratio of layer height ( $h$ ) in mm to nozzle diameter ( $D$ ) in mm;  $RPM$  is the screw motor speed in RPM; and  $T$  is the extrudate temperature in °C.

Since only two levels of temperature were selected for the experimental runs, the  $T^2$  term is not estimated in the regression analysis. An analysis was carried out to check the significance of each of the terms in Equation 5. From the analysis it was observed that removing a term from the equation had significant change in the predicted bead width compared to measured value. The analysis is tabulated in Table 18 with each bead width calculated with the removal of each term. Moreover, the  $R^2$  predicted value of the equation

reduces further if terms are omitted. Pertinent data relating to the regression analysis yielding Equation (5) are summarized in Table 19.

Table 18. Analysis to determine the validity of terms in Equation 5

Temp	h/d	RPM	Measured BW	BW based on Eqn 5	Omitted term								
					h/D	RPM	T	(h/D) x (h/D)	RPM x RPM	h/D x RPM	h/D x T	RPM x T	h/D x RPM x T
360	0.6	200	8.2	8.3	-5.7	3.1	-27.8	8.8	7.9	10.7	17.5	15.4	6.3
360	0.6	500	6.7	6.9	-7.2	-6.2	-29.3	7.4	4.6	12.9	16.0	24.5	1.8
360	0.6	800	6.5	7.1	-7.0	-13.9	-29.1	7.5	1.3	16.8	16.2	35.3	-1.0
360	0.7	200	8.6	8.9	-7.5	3.6	-27.3	9.5	8.5	11.7	19.6	15.9	6.5
360	0.7	500	7.3	7.4	-9.0	-5.7	-28.8	8.0	5.1	14.4	18.0	25.0	1.4
360	0.7	800	7.1	7.5	-8.9	-13.5	-28.7	8.1	1.7	18.8	18.1	35.7	-2.0
360	0.8	200	9.4	9.4	-9.3	4.2	-26.7	10.3	9.1	12.7	21.6	16.5	6.7
360	0.8	500	7.6	7.8	-10.9	-5.3	-28.3	8.7	5.6	15.9	20.0	25.5	1.0
360	0.8	800	7.3	7.8	-10.9	-13.1	-28.3	8.6	2.1	20.7	20.0	36.0	-3.0
390	0.6	200	10.1	10.1	-3.9	4.9	-29.0	10.6	9.8	12.6	20.1	17.8	7.9
390	0.6	500	7.7	8.1	-6.0	-5.0	-31.1	8.6	5.8	14.1	18.0	27.2	2.6
390	0.6	800	7.3	7.6	-6.4	-13.3	-31.5	8.1	1.9	17.3	17.6	38.2	-1.1
390	0.7	200	10.6	10.6	-5.8	5.4	-28.5	11.3	10.3	13.4	22.2	18.3	8.0
390	0.7	500	8.2	8.5	-7.9	-4.6	-30.7	9.1	6.3	15.6	20.1	27.6	2.1
390	0.7	800	7.6	8.0	-8.4	-12.9	-31.1	8.7	2.3	19.3	19.6	38.6	-2.2
390	0.8	200	10.9	11.1	-7.7	5.8	-28.1	11.9	10.7	14.3	24.3	18.7	8.1
390	0.8	500	8.7	8.9	-9.8	-4.2	-30.3	9.7	6.7	17.0	22.1	28.0	1.6
390	0.8	800	8.0	8.4	-10.4	-12.6	-30.8	9.2	2.6	21.3	21.6	38.9	-3.4

Table 19. Model summary for the regression Equation 5.

Standard deviation	R-square	R-square (adjusted)	R-square (predicted)
0.202mm	98.13%	97.49%	96.51%

Equation (5) was used to calculate the bead width and also the overlap percentage between beads in the process used to generate the GCODE for the custom experimental setup. Based on this bead width estimation equation and required overlap between beads, a Python script was written that takes the printing parameters from Table 9 as inputs to generate the GCODE for printing rectangular blocks and circular features.

### 3.4.3 Statistical analysis for optimizing inter-bead porosity

Table 20 shows the measured values of total cross section area for four layers and four beads widths and the area of the pore in this measured area for each of the DoE runs as listed in Table 13. The porosity percentage is calculated from these values. Cross-section #1, #2 and #3 in Table 20 refers to the cross-

section at the Y-axis position of 75mm, 100mm, 125mm, respectively as shown in Figure 27. Note that the total area of the cross-sections with no visible pores were not measured and denoted as ‘not applicable’ (n/a) as it is not necessary for the porosity percentage calculation.

Table 20. Porosity measurement for each run of the DoE.

Run # 1			
Cross-section #	1	2	3
Total area (mm <sup>2</sup> )	11485.8	11513.8	11638.6
Pore area (mm <sup>2</sup> )	363.72	334.37	447.41
Pore area %	3.17	2.90	3.84
Average	3.30		

Run # 2			
Cross-section #	1	2	3
Total area (mm <sup>2</sup> )	9088.14	9362.81	9203.07
Pore area (mm <sup>2</sup> )	67.47	119.77	97.65
Pore area %	0.74	1.28	1.06
Average	1.03		

Run # 3			
Cross-section #	1	2	3
Total area (mm <sup>2</sup> )	16710.8	16326.2	16282.7
Pore area (mm <sup>2</sup> )	228.63	113.93	166.48
Pore area %	1.37	0.70	1.02
Average	1.03		

Run # 4			
Cross-section #	1	2	3
Total area (mm <sup>2</sup> )	14278.7	14459.6	13891
Pore area (mm <sup>2</sup> )	123.7	183.98	122.45
Pore area %	0.87	1.27	0.88
Average	1.01		

Run # 5			
Cross-section #	1	2	3
Total area (mm <sup>2</sup> )	n/a	11882.5	n/a
Pore area (mm <sup>2</sup> )	0	29.69	0
Pore area %	0.00	0.25	0.00
Average	0.08		

Run # 6			
Cross-section #	1	2	3
Total area (mm <sup>2</sup> )	n/a	n/a	n/a
Pore area (mm <sup>2</sup> )	0	0	0
Pore area %	0.00	0.00	0.00
Average	0.00		

Run # 7			
Cross-section #	1	2	3
Total area (mm <sup>2</sup> )	n/a	n/a	n/a
Pore area (mm <sup>2</sup> )	0	0	0
Pore area %	0.00	0.00	0.00
Average	0.00		

Run # 8			
Cross-section #	1	2	3
Total area (mm <sup>2</sup> )	n/a	12226.1	n/a
Pore area (mm <sup>2</sup> )	0	15.31	0
Pore area %	0.00	0.13	0.00
Average	0.04		

Run # 9			
Cross-section #	1	2	3
Total area (mm <sup>2</sup> )	15520.8	13812.3	14981.5
Pore area (mm <sup>2</sup> )	87.24	67.97	88.24
Pore area %	0.56	0.49	0.59
Average	0.55		

Run # 10			
Cross-section #	1	2	3
Total area (mm <sup>2</sup> )	11053.4	11601.7	11524.6
Pore area (mm <sup>2</sup> )	42.74	26.79	74.42
Pore area %	0.39	0.23	0.65
Average	0.42		

Run # 11			
Cross-section #	1	2	3
Total area (mm <sup>2</sup> )	9281.25	9096.99	9504.65
Pore area (mm <sup>2</sup> )	37.15	21.18	31.65
Pore area %	0.40	0.23	0.33
Average	0.32		

Run # 12			
Cross-section #	1	2	3
Total area (mm <sup>2</sup> )	13400.8	12863.8	12576
Pore area (mm <sup>2</sup> )	115.05	91.15	126.33
Pore area %	0.86	0.71	1.00
Average	0.86		

Run # 13			
Cross-section #	1	2	3
Total area (mm <sup>2</sup> )	11852	11783.9	11881.6
Pore area (mm <sup>2</sup> )	94.09	60.14	86.99
Pore area %	0.79	0.51	0.73
Average	0.68		

Run # 14			
Cross-section #	1	2	3
Total area (mm <sup>2</sup> )	n/a	n/a	n/a
Pore area (mm <sup>2</sup> )	0	0	0
Pore area %	0.00	0.00	0.00
Average	0.00		

Run # 15			
Cross-section #	1	2	3
Total area (mm <sup>2</sup> )	11432.7	12152.6	11574.5
Pore area (mm <sup>2</sup> )	10.94	9.08	21
Pore area %	0.10	0.07	0.18
Average	0.12		

Run # 16			
Cross-section #	1	2	3
Total area (mm <sup>2</sup> )	11496.4	11750.5	12691.3
Pore area (mm <sup>2</sup> )	13.89	4.33	7.08
Pore area %	0.12	0.04	0.06
Average	0.07		

Run # 17			
Cross-section #	1	2	3
Total area (mm <sup>2</sup> )	13245.7	12390.1	12552.5
Pore area (mm <sup>2</sup> )	18.76	43.31	39.96
Pore area %	0.14	0.35	0.32
Average	0.27		

Run # 18			
Cross-section #	1	2	3
Total area (mm <sup>2</sup> )	12263.8	12086.9	12630.4
Pore area (mm <sup>2</sup> )	31.75	21.35	47.19
Pore area %	0.26	0.18	0.37
Average	0.27		

Run # 19			
Cross-section #	1	2	3
Total area (mm <sup>2</sup> )	12305.7	12356.1	12024.1
Pore area (mm <sup>2</sup> )	37.56	7.78	64.19
Pore area %	0.31	0.06	0.53
Average	0.30		

Run # 20			
Cross-section #	1	2	3
Total area (mm <sup>2</sup> )	n/a	12327.1	12211.4
Pore area (mm <sup>2</sup> )	0	38.62	13.78
Pore area %	0.00	0.31	0.11
Average	0.14		

Table 21 presents the analysis of variance for the parameters affecting inter-bead porosity. Figure 36(a) plots the fitted mean effect of each individual input variables screw motor RPM, layer height to nozzle diameter ratio and bead overlap % on inter-bead porosity. Figure 36(b) shows the 2-way interaction of the input variables and their fitted mean response on the inter-bead porosity. Considering a confidence interval of 95%, it was concluded that overlap percentage was the only parameter that has a significant effect on inter-bead porosity. Figure 36(a) and 36(b) reinforces this conclusion that overlap percentage has the most significant effect on inter-bead porosity. Until the optimal degree of overlap between the beads, inter-bead porosity will be present and beyond the optimal overlap percentage, there is no significant effect on porosity.

Table 21. Analysis of variance for inter-bead porosity versus screw motor RPM, h/D, overlap%.

Source	DF	Adj SS	Adj MS	F-Value	P-Value
Model	9	9.0791	1.00879	6.59	0.003
<b>Linear interaction of input parameters</b>					
Linear	3	5.7264	1.90879	12.48	0.001
<i>RPM</i>	1	0.6093	0.60927	3.98	0.074
$\frac{h}{D}$	1	0.325	0.32497	2.12	0.176
OL%	1	4.7921	4.79213	31.32	0.000
<b>Second order interaction of input parameters</b>					
Square	3	1.3716	0.45721	2.99	0.082
<i>RPM</i> * <i>RPM</i>	1	0.1241	0.12406	0.81	0.389
$\frac{h}{D}$ * $\frac{h}{D}$	1	0.2774	0.2774	1.81	0.208
OL%*OL%	1	0.0125	0.01248	0.08	0.781
<b>2-Way interaction between input parameters</b>					
2-Way Interaction	3	1.9811	0.66036	4.32	0.034
<i>RPM</i> * $\frac{h}{D}$	1	0.7079	0.70788	4.63	0.057
<i>RPM</i> * OL%	1	0.6377	0.63768	4.17	0.068
$\frac{h}{D}$ * OL%	1	0.6355	0.63551	4.15	0.069
Error	10	1.5299	0.15299		
Lack-of-Fit	5	1.4834	0.29667	31.88	0.001
Pure Error	5	0.0465	0.00931		
Total	19	10.609			

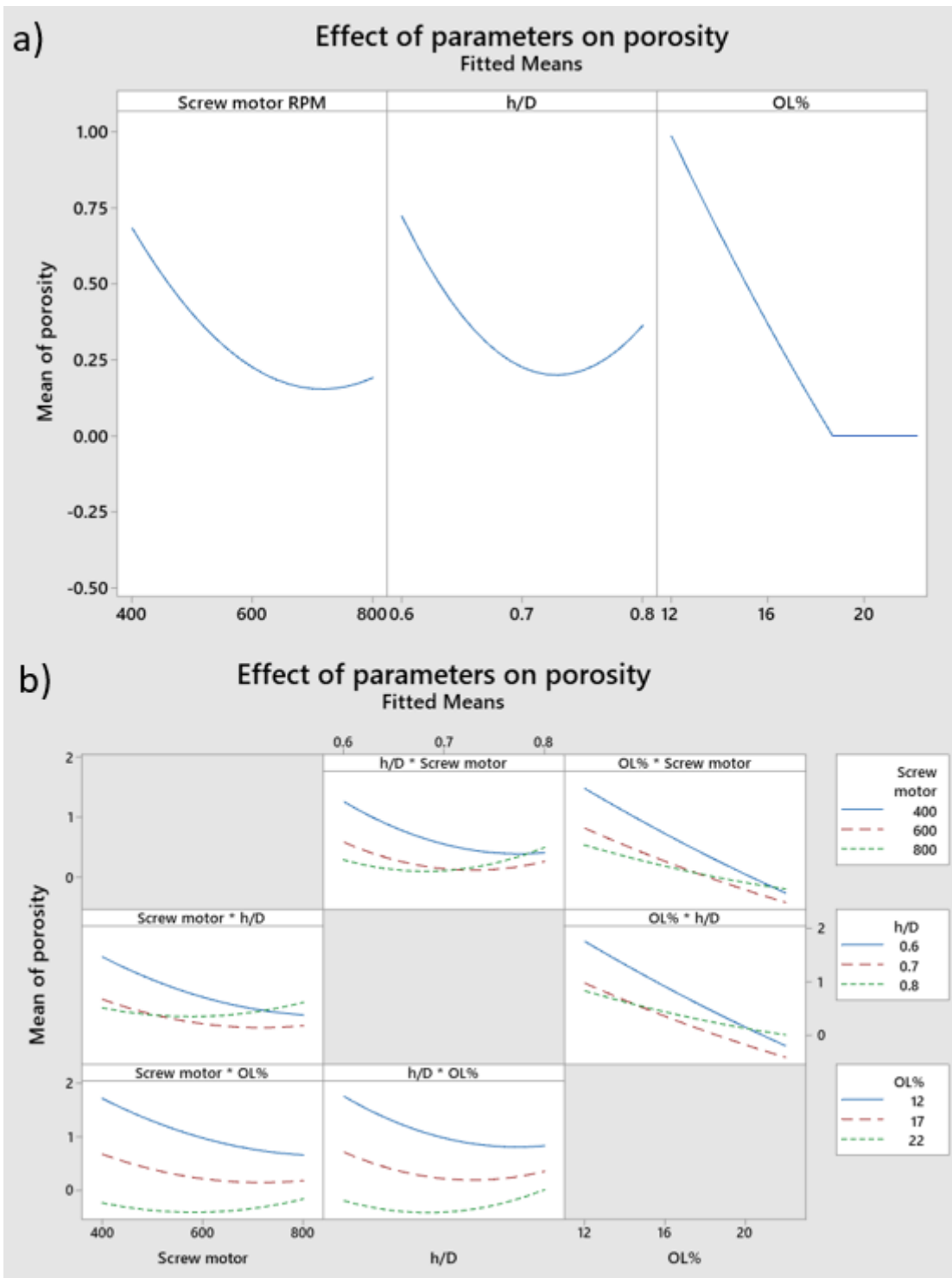


Figure 36. Factor effect plots and surface plots for porosity: a) Main effect plots, b) interaction plots.

#### *3.4.4 Statistical analysis for optimizing surface uniformity*

Table 22 shows the surface uniformity measurement obtained from the profilometer as mentioned in Section 3.2. The surface deformity measured at 5 different line segments on the top face is averaged and used as the response variable in the statistical analysis listed in Table 13.

Table 23 presents the analysis of variance for the parameters affecting surface uniformity. Figure 37(a) plots the fitted mean effect of each individual input variables screw motor RPM, layer height to nozzle diameter ratio and bead overlap %. Figure 37(b) shows the 2-way interaction of the input variables and their fitted mean response on the surface deformity. Considering a confidence interval of 95%, it was concluded that overlap percentage and 2-way interaction between overlap percentage and layer height to nozzle diameter ratio were the parameters that have significant influence on surface uniformity. Figure 37(a) and 37(b) reinforces this conclusion that overlap percentage and 2-way interaction between overlap percentage and layer height to nozzle diameter ratio has the most significant effect on surface uniformity. It was observed during the printing process, as the overlap percentage was increased the uniformity of the top surface was increasing until a particular degree of overlap. Beyond this, the interface of the beads was forming ridge like geometry due to over extruded material. Similarly, the layer height along with the scanning velocity defines the aspect ratio of the beads when the extrusion velocity is held constant. It was observed that lower aspect ratio beads produced a bead overlap into the rectangle section of the bead geometry creating ridges and the higher aspect ratio beads did not provide sufficient overlap thus creating valley like pattern on the top face.

Table 22 . Surface uniformity measurements for the DoE samples.

<b>Sample No.</b>	<b>Reading 1</b>	<b>Reading 2</b>	<b>Reading 3</b>	<b>Reading 4</b>	<b>Reading 5</b>	<b>Average</b>	<b>Std dev</b>
	<b>mm</b>	<b>mm</b>	<b>mm</b>	<b>mm</b>	<b>mm</b>	<b>mm</b>	<b>mm</b>
1	6.856	1.785	1.621	6.002	6.104	4.474	2.551
2	2.909	3.224	3.305	3.241	3.171	3.170	0.154
3	2.108	1.914	1.689	1.769	1.807	1.857	0.162
4	2.434	2.289	2.185	2.376	2.336	2.324	0.094
5	0.909	0.91	1.145	1.358	1.193	1.103	0.194
6	1.082	1.34	1.451	1.5	1.802	1.435	0.261
7	1.35	1.344	1.164	1.3	1.322	1.296	0.076
8	2.238	1.943	1.995	1.99	2.028	2.039	0.115
9	1.272	1.221	1.066	0.901	1.208	1.134	0.151
10	1.61	1.799	1.98	1.88	1.97	1.848	0.152
11	1.06	1.102	1.057	0.79	0.95	0.992	0.126
12	1.934	1.875	1.957	1.795	1.7	1.852	0.106
13	1.442	1.381	1.33	1.36	1.279	1.358	0.060
14	1.673	1.303	1.448	1.475	2.504	1.681	0.479
15	1.736	1.594	1.707	1.167	0.96	1.433	0.349
16	1.33	1.777	1.561	1.278	1.276	1.444	0.220
17	1.119	1.177	1.235	1.137	1.21	1.176	0.048
18	1.123	1.257	1.324	1.35	1.446	1.300	0.120
19	1.122	1.085	1.087	1.003	1.334	1.126	0.124
20	1.499	1.224	1.388	1.161	1.227	1.300	0.139

Table 23. Analysis of surface uniformity versus screw motor RPM, h/D, overlap%.

Source	DF	Adj SS	Adj MS	F-Value	P-Value
Model	9	10.2218	1.13576	4.07	0.02
<b>Linear interaction of input parameters</b>					
Linear	3	3.5861	1.19537	4.28	0.035
<i>RPM</i>	1	0.0906	0.09063	0.32	0.581
$\frac{h}{D}$	1	0.3258	0.3258	1.17	0.305
OL%	1	3.1697	3.16969	11.36	0.007
<b>Second order interaction of input parameters</b>					
Square	3	3.3169	1.10562	3.96	0.042
<i>RPM * RPM</i>	1	0.2992	0.29921	1.07	0.325
$\frac{h}{D} * \frac{h}{D}$	1	0.1876	0.18755	0.67	0.431
OL%*OL%	1	0.3537	0.35374	1.27	0.286
<b>2-Way interaction between input parameters</b>					
2-Way Interaction	3	3.3189	1.10628	3.96	0.042
<i>RPM * <math>\frac{h}{D}</math></i>	1	0.5946	0.5946	2.13	0.175
<i>RPM * OL%</i>	1	0.4569	0.45687	1.64	0.23
$\frac{h}{D} * OL%$	1	2.2674	2.26739	8.13	0.017
Error	10	2.7905	0.27905		
Lack-of-Fit	5	2.7064	0.54127	32.18	0.001
Pure Error	5	0.0841	0.01682		
Total	19	13.0123			

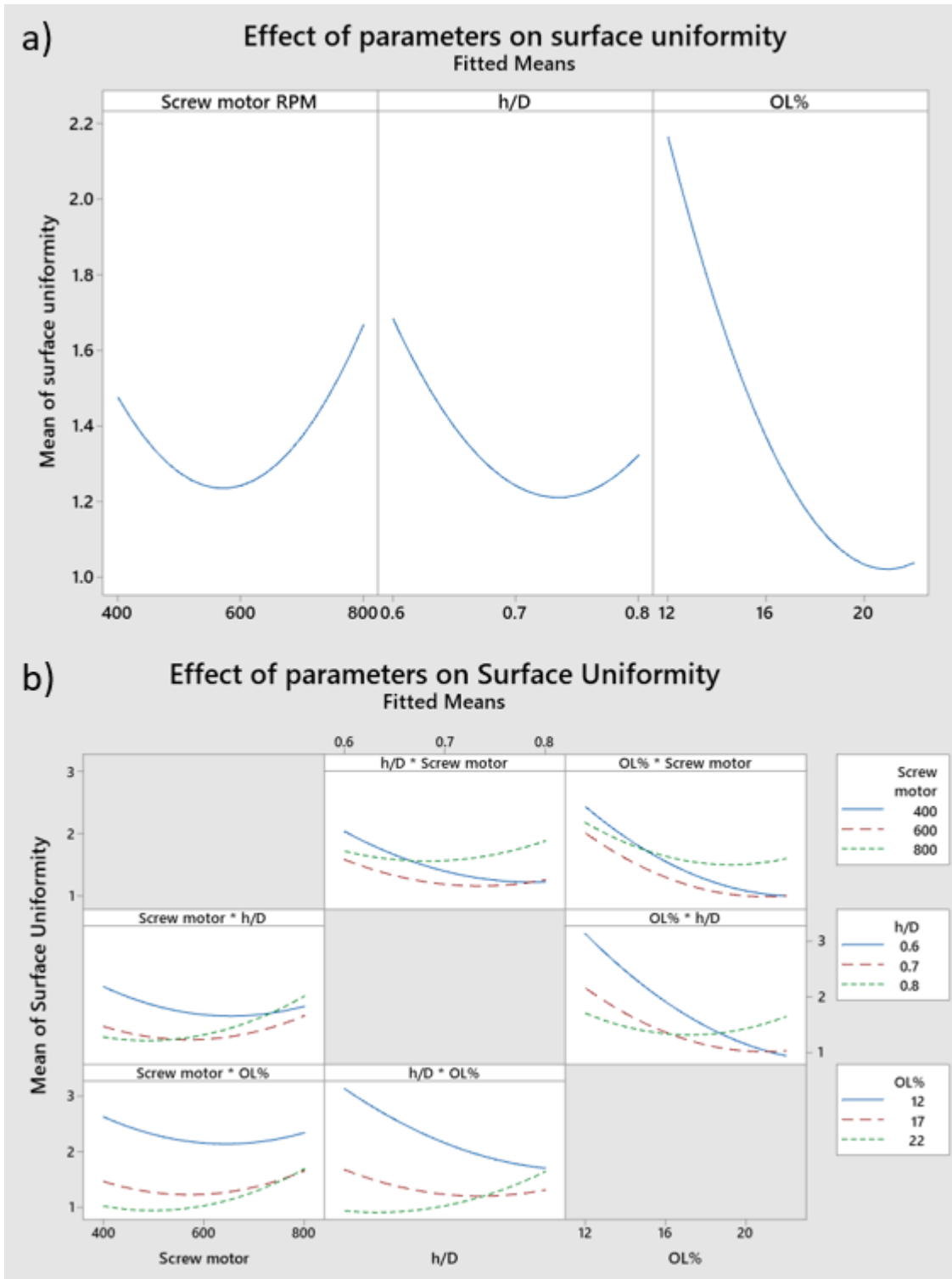


Figure 37. Factor effect plots and surface plots for surface uniformity: a) Main effect plots, b) interaction plots.

### 3.4.5 Validation of optimized response

From the central composite design carried out for inter-bead porosity and surface uniformity, the response optimization function in Minitab was used to generate a range of parameters to minimize both the responses. Screw motor RPM, layer height and overlap percentage were the parameters optimized.

The optimized set of parameters and the predicted response are tabulated in Table 24. Through the optimization of the parameters, zero porosity parts with an average surface uniformity of 1.25mm were printed. There was a 0.3% positive difference and a 0.08mm negative difference for inter-bead porosity and surface uniformity respectively between predicted and measured values. A sample part printed with optimized parameters is shown in Figure 38.

Table 24. Optimized set of process parameters for printing minimal porous and surface deformity parts, the predicted and measured value.

$\frac{h}{D}$	Overlap %	Screw motor RPM	Predicted		Actual		Residual	
			Porosity %	Surface Uniformity (mm)	Porosity %	Surface Uniformity (mm)	Porosity %	Surface Uniformity (mm)
0.77	17	500	0.3	1.17	0	1.25	0.3	0.08

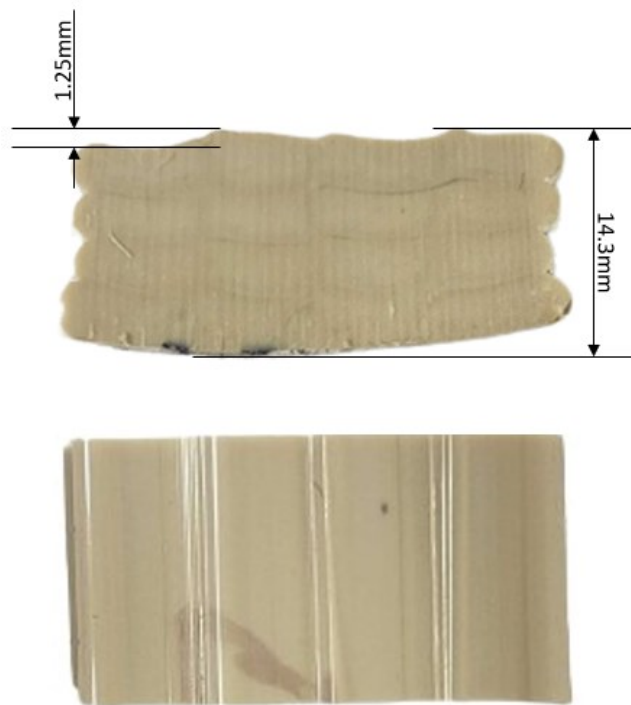


Figure 38. Cut piece of PEEK sample printed with optimized parameters.

### 3.5 Mechanical characterization

In order to test the strength of the inter bead adhesion of the parts printed from the AM system developed, tensile testing was conducted on tensile test coupons produced according to the optimized parameters identified from design of experiments. Figure 39 shows the samples printed for machining out the tensile test samples. The red box in the figure denotes the area from which the samples were machined. Five tensile test coupons were produced and machined on CNC router to the dimensions according to ISO 527-2 Type 1B, with a total length of 150 mm, a gauge length of 60 mm, a width of 10 mm and a thickness of 4 mm, as shown in Figure 40. The tensile tests were conducted with a test speed of 1 mm/min with an Instron 5966 Universal Testing Machine (Instron, Norwood, Massachusetts, US) and strain was measured with an Epsilon ONE optical extensometer (Epsilon Technology Corp., Jackson, Wyoming, US).

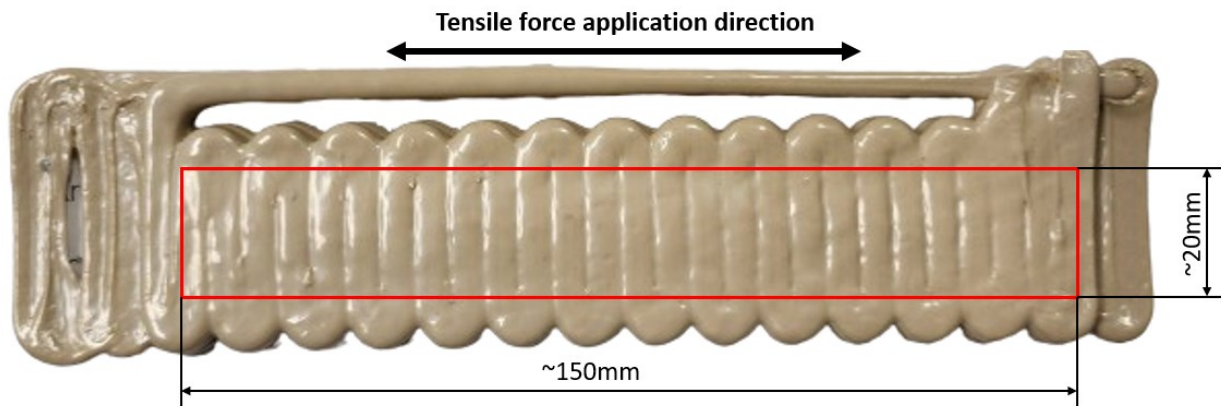


Figure 39. Geometry of sample 3D printed for machining out tensile test coupons.

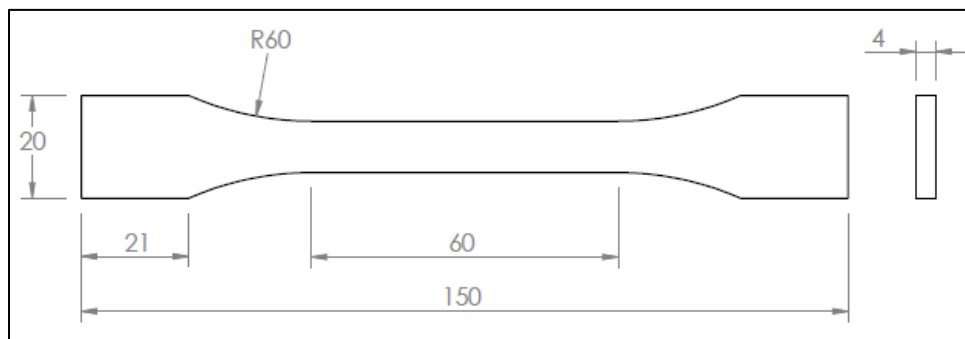


Figure 40. Dimensions (in mm) of tensile test coupons according to ISO 527-2 Type 1B.

The examined specimens demonstrated ultimate tensile strengths ranging between 72.2 and 92.2 MPa, with Young's Moduli between 3.54 and 3.70 GPa. It was noted during testing that Sample 2 contained an inter-bead void due to inconsistencies in the printing process, leading to fracture at this specific site, which

accounts for its lower ultimate tensile strength relative to the other samples. The stress-strain curves for the samples are depicted in Figure 41. Table 25 provides detailed values for ultimate tensile strength, and Young's modulus of the samples, along with a comparative analysis of the mechanical properties of PEEK components fabricated using various manufacturing methods. The findings of this study indicate that the parts produced in the current work exhibit similar strength compared to those created by other 3D printing methods, yet they still fall short of the strength levels seen in injection molded parts.

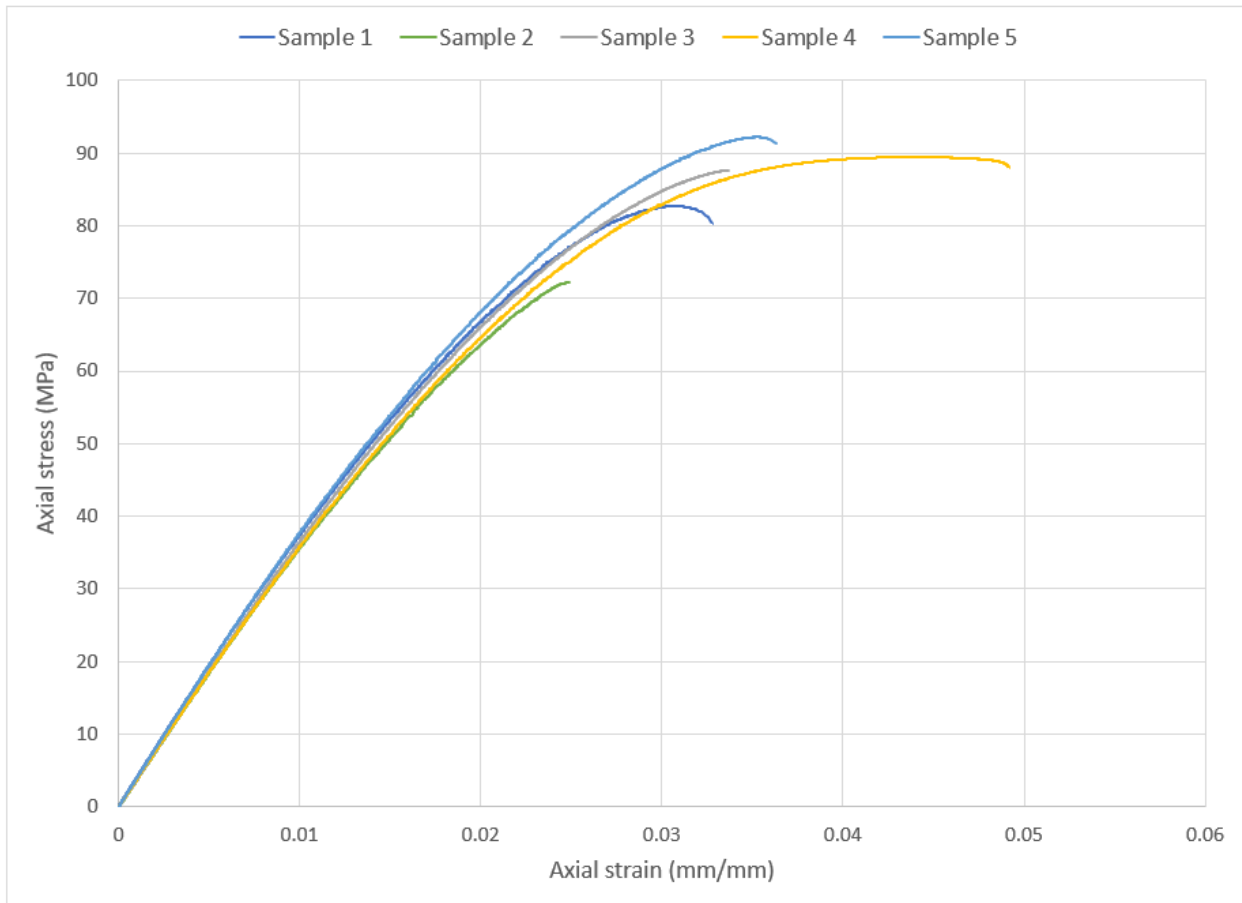


Figure 41. Stress strain curve for the PEEK printed samples.

Table 25. Tensile test comparison data for PEEK parts

Author	Printing technique	Material	Extruder temperature (°C)	Raster orientation (°)	Us (Mpa)	E (Gpa)
Present work	FGF	PEEK 5600G	390	90	84.9	3.60
Jian-Wei et al., (2017) [1]	FGF	PEEK 90G	370	0	64.0	3.91
			390	0	94.0	4.13
Rehekampff et al., (2019) [2]	FFF	AM MS NT1 PEEK	415	0/90	83.4	-
McLauchlin et al., (2014) [3]	Injection molding	PEEK 450G	380	N/A	100	-

### 3.6 Conclusions

A robotic arm based FGF 3D printing system was realized for printing high temperature engineering polymers with processing temperatures up to 400°C. PEEK polymer, which is popular for industrial applications, was used for this study. The system provides a large print volume of 2000mm x 2000mm x 3500mm and a maximum material throughput of 2.3kg/hr with a 4mm nozzle opening. The study to optimize the process parameter optimization for minimizing inter-bead void and surface deformity was conducted. From the study, it was found that based on the relations considered between parameters, the degree of bead overlap was the major parameter that affected both the inter-bead voids and the surface deformity in printed parts while the layer height and extrusion velocity did not have significant effects. Tensile test was conducted on printed parts which showed comparable strength to 3D printed PEEK parts reported in literature. Some of parts printed using the system can be seen in Appendix 1.

In addition, challenges associated with printing the high temperature semi-crystalline PEEK polymer were addressed. Controlling the cooling rate of the deposited beads improved the problem of delamination of parts while printing and helped in reducing the effect of warping. This can be attributed to the higher energy state of the already deposited layer while printing subsequent layers and the delayed onset of crystallization while cooling, respectively. The problem of warping still pertains to particular geometries and infill patterns which we believe will be curbed on the addition of carbon fiber to the polymer. Laser texturing the printing surface significantly improved the bed adhesion of PEEK to AISI 304 bed surface while printing thus improving the print quality. Oozing of material was taken a design consideration for the new nozzle, details are discussed in Chapter 4.

## **Chapter 4 Design of a continuous carbon fiber/PEEK co-extrusion nozzle**

The chapter explains the design process undertaken for the continuous fiber printing nozzle. Section 4.1 details the design consideration based on the factors influencing the printing of continuous fiber. Sections 4.2 and 4.3 runs through the different nozzle design iterations. Lastly, Section 4.4 discusses the numerical analysis conducted on the nozzle designs.

### **4.1 Nozzle design considerations**

The nozzle was designed to function with a screw based thermoplastic extruder. Parts were modelled in SolidWorks 2022 (Dassault Systems, Waltham, MA, USA). An innovative strategy to impregnate the carbon fiber with polymer matrix inside the nozzle was designed and analyzed. The nozzle has a channel that feeds carbon fiber to the polymer melt, which is deposited by the viscous drag force from the polymer flow. The nozzle was primarily designed for PEEK polymer in conjunction with continuous carbon fiber 3D printing, but the system can be used to print any continuous fiber with a suitable polymer matrix. The nozzle sections were designed to fit the RobotDigg SJ-35 extruder.

#### *4.1.1 Factors influencing nozzle design*

A study was conducted on the factors influencing the functioning of the nozzle. The following factors were taken into consideration as guidelines for the design.

1. The mass of the nozzle assembly should not exceed 5kg. The load capacity of the robotic arm is 50kg. A capacity of 10kg was reserved for forthcoming projects and developments. Details for the mass of components mounted on robot arm are given in Table 26.
2. The designed nozzle should work in conjunction with the Robotdigg SJ-35 extruder. This requires a seamless assembly with the extruder, and the screw motor should be capable of pushing the PEEK through the entire channel length of the nozzle.
3. The nozzle should have a modular design for ease of cleaning the nozzle in case of clogging. The nozzle tip should be interchangeable to study the effects with different nozzle sizes.
4. Change in section diameters should be minimal to reduce the pressure drop along the flow direction. According to [133], a change in nozzle diameter can significantly influence the pressure drop along the liquefier thus impacting the quality of the final product.

5. Flow of molten PEEK polymer into the carbon fiber feeding channel needs to be avoided. The geometry at the point of carbon fiber entry was designed such that the pressure of the molten polymer at the point was comparable with atmospheric pressure.
6. Due to the viscosity of the molten polymer, a viscous drag force is applied on the surface it flows over [133]. The carbon fiber feeding should be through the viscous drag force exerted by the polymer on the carbon fiber.
7. The temperature distribution should be uniform with minimal cold spots in the polymer flowing channel. Any temperature sensor placement must ensure that the temperature reading from the metal material in which it is embedded mimics the polymer temperature closely. The heater placement should ensure a uniform heat distribution.
8. Material used to manufacture the nozzle should withstand temperatures up to 750°C, as cleaning of the nozzle might have to be carried out by decomposing PEEK. From the thermogravimetric analysis for PEEK shown in Section 2.1.1, it is known that the material degrades to 18% of initial mass at 750°C. Carbon steel (AISI 1020), stainless steel (AISI 304), aluminum (Al-6061-T6) and brass (C360) were considered for manufacturing the parts. Most commonly available alloy grades were selected for each material. Material was selected based on the decision matrix detailed in
9. Table 27. Materials were rated out of 10, where 10 being most desirable and 0 being least. Material was chosen based on the total score. As indicated in
10. Table 27, AISI 304 stainless steel was selected based as it received the maximum score.
11. The velocity profile of the polymer from the point of carbon fiber entry should be increasing or maintained constant to avoid mass accumulation inside nozzle which in turn leads to spooling of the fiber inside the nozzle.

Table 26. Mass of components mounted on robot arm.

<b>Sl.no.</b>	<b>Part</b>	<b>Weight (kg)</b>
1	Extruder net weight	20
2	Extruder gross weight (with material and insulation material)	23
3	Mounting plates connecting extruder to robot	8
4	Carbon fiber feeding system	4
	Subtotal	35
	Total allowable weight on robot excluding reserve load	40
5	Allowable weight for carbon fiber printing nozzle	5

Table 27. Decision matrix for material selection for nozzle parts.

<b>Parameters</b>	<b>Carbon steel</b>	<b>Stainless steel</b>	<b>Aluminum</b>	<b>Brass</b>
Temperature capability (Recrystallisation above 750°C) [134]	10	10	0	5
Material density	5	5	10	5
Ease of machining [135, 136]	7	5	10	10
Corrosion resistant [137-140]	5	7	7	7
Cost [131]	10	10	7	5
<b>Total score</b>	<b>37</b>	<b>40</b>	<b>32</b>	<b>32</b>

## 4.2 First design iteration

Based on the design considerations mentioned above, the initial design concept was created. This design concept consisted of five parts with overall assembly dimensions in mm as seen in Figure 42 to 44. Note that fasteners were omitted in the CAD model as it was created primarily for preliminary computational fluid dynamics (CFD) analysis. The internal sections through which the PEEK and carbon fiber flows is the computational domain. The results from the computational fluid dynamics analysis conducted on the initial design are explained in Section 4.5.5. A parametric study was conducted on the external geometry of carbon fiber feed portion, i.e., referred to herein as ‘CF nozzle’, and the internal geometry of the fiber-polymer flow portion of the nozzle, i.e., ‘PEEK+CF nozzle’, to achieve a geometry that prevents molten PEEK from leak through the carbon fiber feed feature while fiber is fed through the system.

Items listed in the bill of materials in Figure 42 are explained as follows:

1. The nozzle side mount is in place to connect the PEEK pipe from the Robodigg SJ35 extruder with the PEEK+CF nozzle.
2. PEEK+CF nozzle is where the molten material mixes with the feed of continuous carbon fiber.
3. Impregnation nozzle serves the purpose of ensuring proper penetration of molten PEEK into the carbon fiber strand. As the viscosity of PEEK is comparatively higher than most polymers, it was found that for proper impregnation sufficient time and pressure was required as mentioned in Section 1.2.4. The impregnation nozzle has a protruding nozzle in place to increase the time the fiber is mixed in molten PEEK. The order of impregnation was to be determined experimentally as modelling the problem is quite difficult.
4. The PEEK pipe with flange is the section that transports molten PEEK from the Robodigg SJ-35 extruder to the PEEK+CF nozzle.

5. The CF nozzle is the part that feeds carbon fiber into the section. This part was designed in such that PEEK does not flow back through the carbon fiber entry point.

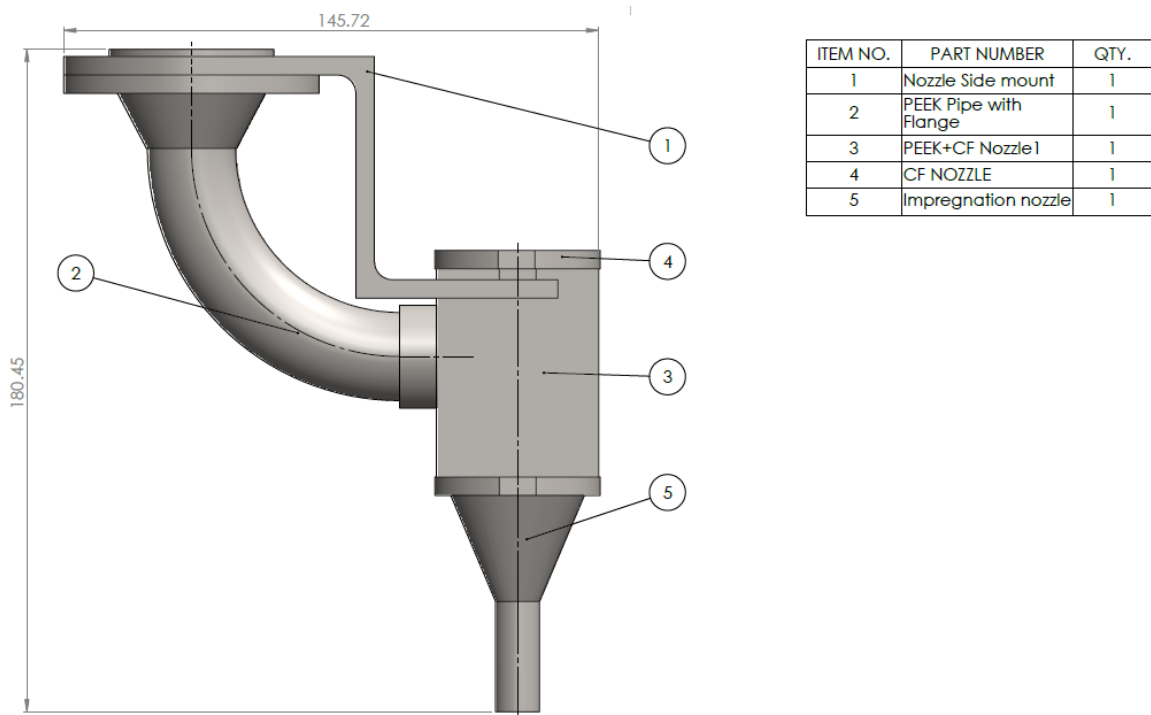


Figure 42. Sideview of the initial nozzle design concept with overall dimensions in mm.

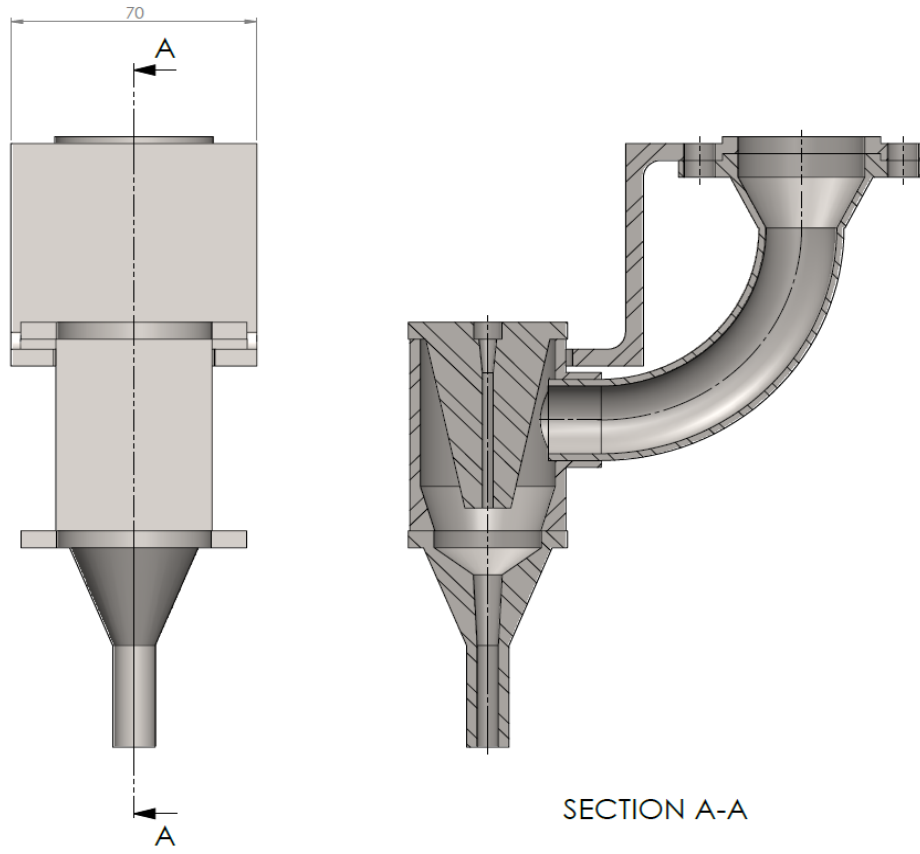


Figure 43. Side view and cross-section view of the initial nozzle design concept.

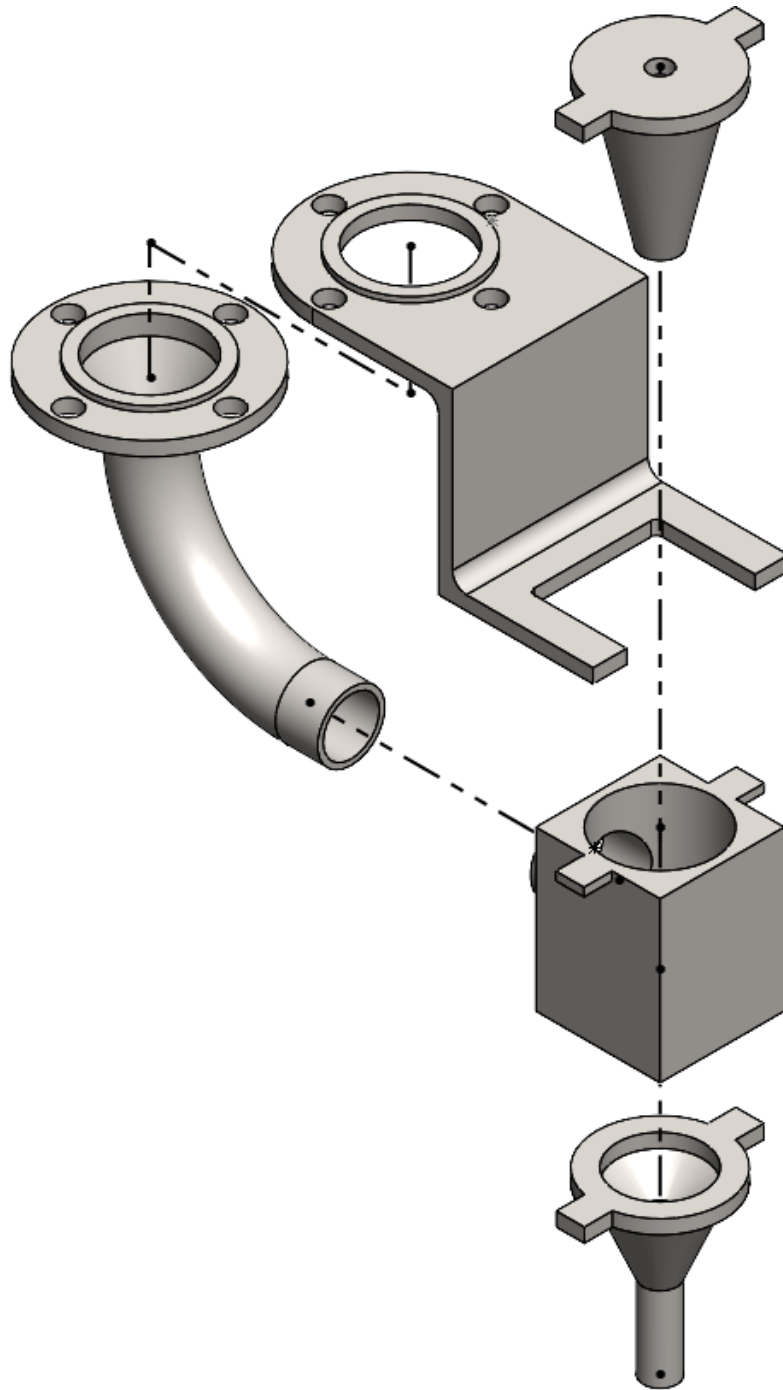


Figure 44 Exploded view of the initial nozzle design concept.

### 4.3 Second design iteration

From the preliminary CFD analysis, it was discovered that a large amount of PEEK was occupying the nozzle flow chamber which can possibly lead to cold spots and mass accumulation for the initial design concept. Another disadvantage was the cost of manufacturing parts like the nozzle side mount and PEEK pipe with flange.

Referring to Figure 45 and 47 for the revised and final design, a plug screw was used to close the blind hole drilled for PEEK flow in the PEEK block part. A dead zone is created at the 90° bend near the plug screw in the PEEK block that forms a fillet which facilitates the further flow [133]. Figure 45 and 46 shows the overall dimensions in mm and a cross-section view of the final design.

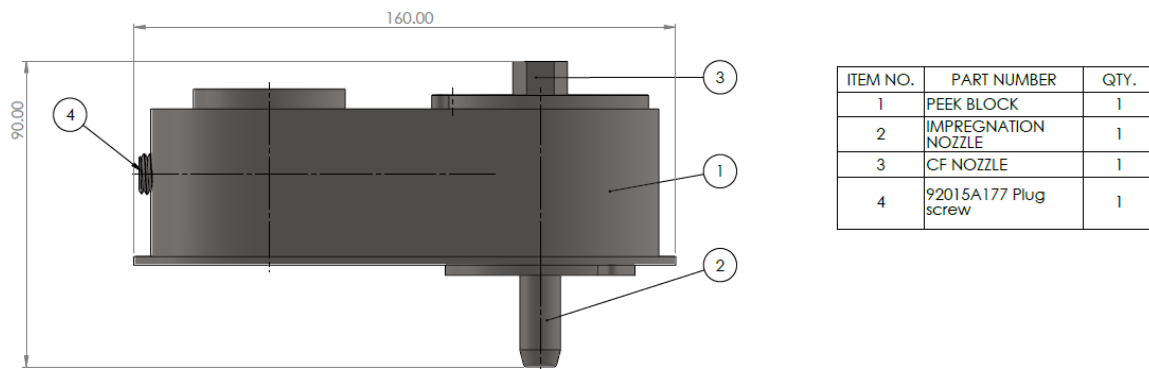


Figure 45. Final nozzle design with overall dimensions in mm.

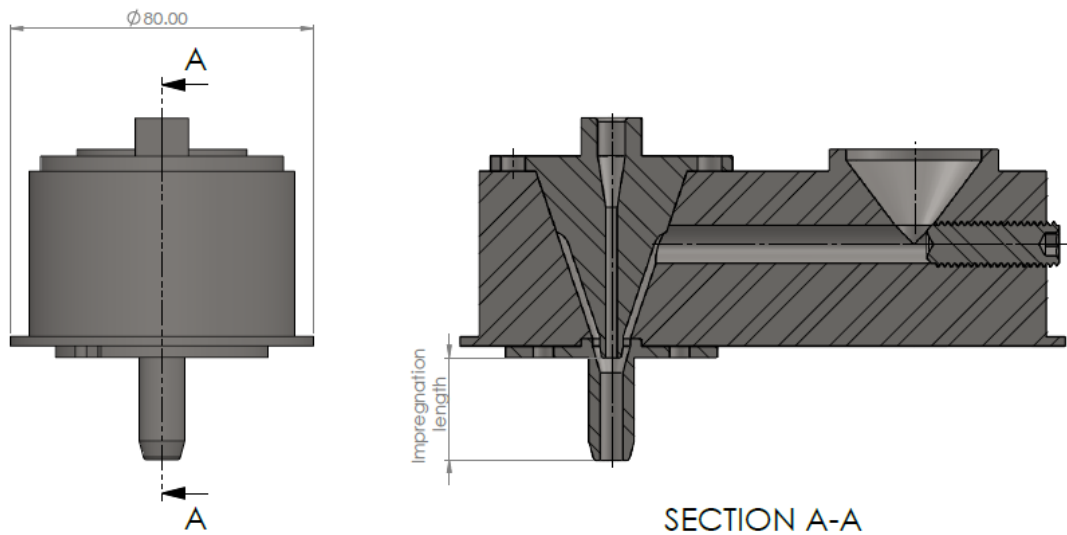


Figure 46. Side view and cross-section view of the final nozzle design.

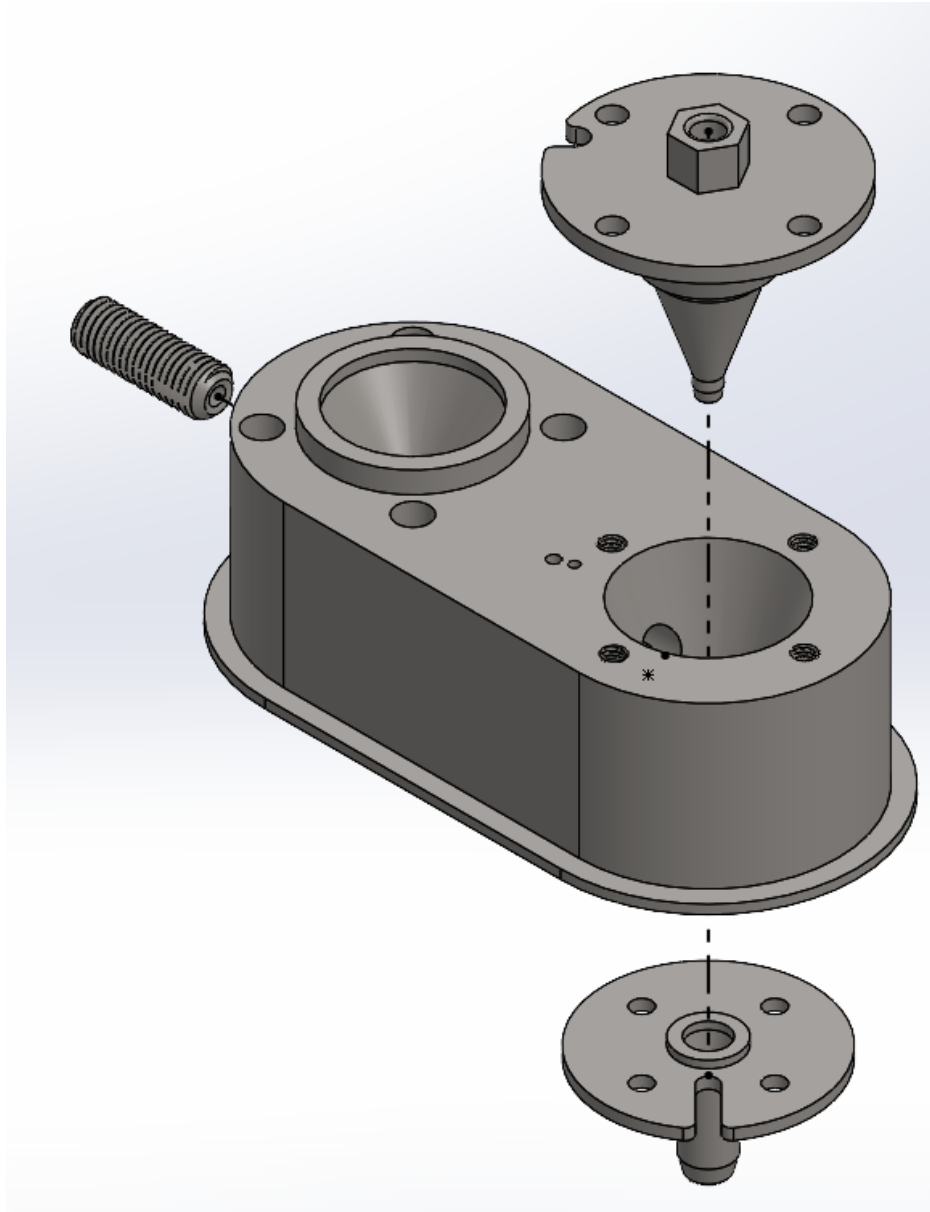


Figure 47. Exploded view of the final nozzle design.

#### 4.4 Numerical analysis of PEEK flow in nozzle

The operation of the nozzle was simulated using the SolidWorks Flow Simulation package to understand the various parameters, such as flow trajectory, temperature distribution, and pressure field. The study was performed to maximize the impregnation length of the nozzle with the PEEK material flowing through the carbon fiber feeding section. Since the boundary conditions, computational domain and meshing was kept the same for both the initial and final nozzle design, these features are illustrated only for the final nozzle design. For solving the fluid regions of the nozzle, SolidWorks Flow Simulation solves the Navier-Stokes

equations, which formulates mass, momentum, and energy conservation laws, see Equations (6) to (9) [141].

$$\frac{\partial \rho}{\partial t} + \frac{\partial}{\partial x_i} (\rho u_i) = 0 \quad (6)$$

$$\frac{\partial \rho u_i}{\partial t} + \frac{\partial}{\partial x_i} (\rho u_i u_j) + \frac{\partial p}{\partial x_i} = \frac{\partial}{\partial x_j} (\tau_{ij} + \tau_{ij}^R) + S_i \quad i = 1,2,3 \quad (7)$$

$$\frac{\partial \rho H}{\partial t} + \frac{\partial \rho u_i H}{\partial x_i} = \frac{\partial}{\partial x_i} (u_j (\tau_{ij} + \tau_{ij}^R) + q_i) + \frac{\partial p}{\partial t} - \tau_{ij}^R \frac{\partial u_i}{\partial x_j} + \rho \varepsilon + S_i u_i + Q_H \quad (8)$$

$$H = h + \frac{u^2}{2} \quad (9)$$

where  $u$  is fluid velocity;  $\rho$  the fluid density;  $S_i$  a mass-distributed external force per unit mass due to a porous media resistance ( $S_i^{porous}$ ), a buoyancy ( $S_i^{gravity}$ ) =  $\rho g_p$ , where  $g_i$  is the gravitational acceleration component along the  $i$ -th coordinate direction), and the coordinate system's rotation ( $S_i^{rotation}$ ), i.e.,  $S_i = S_i^{porous} + S_i^{gravity} + S_i^{rotation}$ ;  $h$  the thermal enthalpy;  $Q_H$  a heat source or sink per unit volume;  $\tau_{ij}$  the viscous shear stress tensor;  $q_i$  the diffusive heat flux; and  $i, j, k$  subscripts used to denote the summation over the three coordinate directions.

Molten PEEK polymer behaves as a non-Newtonian fluid and the SolidWorks Flow Simulation is capable of computing laminar flows of inelastic non-Newtonian liquids. For this, the viscous shear stress tensor is defined as follows:

$$\tau_{ij} = \mu (\dot{\gamma}) \cdot \left( \frac{\partial u_i}{\partial x_j} + \frac{\partial u_j}{\partial x_i} \right) \quad (10)$$

where the shear rate,  $\dot{\gamma} = \sqrt{d_{ij}^2 - d_{ii} \cdot d_{jj}}$ ,  $d_{ij} = \frac{\partial u_i}{\partial x_j} + \frac{\partial u_j}{\partial x_i}$ .

For specifying the viscosity function based on shear rate  $\mu(\dot{\gamma})$ , five models are available in SolidWorks Flow Simulation for inelastic non-Newtonian viscous liquids, i.e.,

1. Herschel-Bulkley model
2. Cross-William-Landel-Ferry model

3. Carreau model
4. Power-law model
5. Polynomial regression model

#### 4.5.1 SolidWorks Flow Simulation setting and computational domain

The green highlighted portions in Figure 48 denote the computational domain for the flow simulation. The computational domain included all the internal geometry through which molten PEEK can flow and faces on which boundary conditions in the assembly. The initial design concept encompassed a similar computational domain including all the internal geometry through which molten PEEK flows and faces on which boundary conditions were applied.

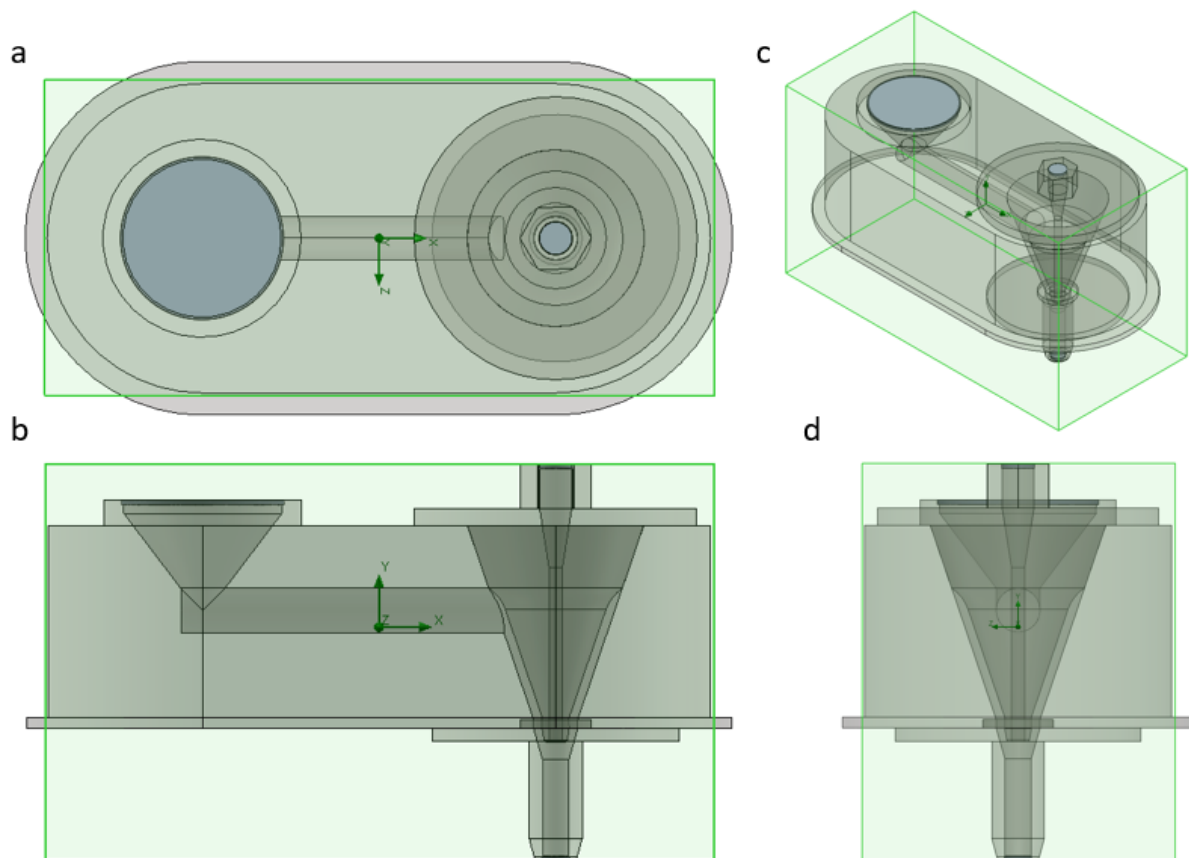


Figure 48. Computational domain for simulation: a) Top view, b) front view, c) isometric view, d) side view.

#### *4.5.1 Material model for non-Newtonian PEEK material*

In order to define an inelastic non-Newtonian liquid in SolidWorks Flow Simulation, material properties are required, such as density, specific heat capacity, thermal conductivity, and viscosity. These properties were supplied to the model as a function of temperature as the properties of PEEK polymer change with temperature. The following sub-section details each material property and their source used for the simulation.

##### *4.5.1.1 Density*

A relation of density versus temperature of PEEK was taken from [26] as illustrated in Figure 49.

##### *4.5.1.2 Specific heat capacity*

Specific heat capacity as a function of temperature for PEEK is illustrated in Figure 50 [26]. The peak in the specific heat capacity plot denotes the melting point of PEEK and measures the latent heat capacity of the material.

##### *4.5.1.3 Thermal conductivity*

The thermal conductivity of PEEK as function of temperature was taken from [27] and is depicted in Figure 51.

##### *4.5.1.4 Viscosity and Viscosity data set*

The polynomial regression model for inelastic non-Newtonian viscous liquids in Solidworks flow simulation was used to input the viscosity data for PEEK. Since there is a lack of data about the viscous behavior of PEEK 450 at various temperatures, the CFD analysis was carried out with an isothermal boundary condition of 350°C for which viscous data was available. A polynomial regression model was chosen for simulating the PEEK flow behavior in SolidWorks Flow Simulation as the viscosity behavior of PEEK 450, which is similar in molecular weight and flow properties as PEEK 5600, was available in [25]. Viscosity data for molten PEEK 450 at 350°C was extracted from the plot in Figure 52. As illustrated by the plot in Figure 52, the maximum shear rate for the Newtonian cut-off for the molten PEEK material is 0.02 1/s.

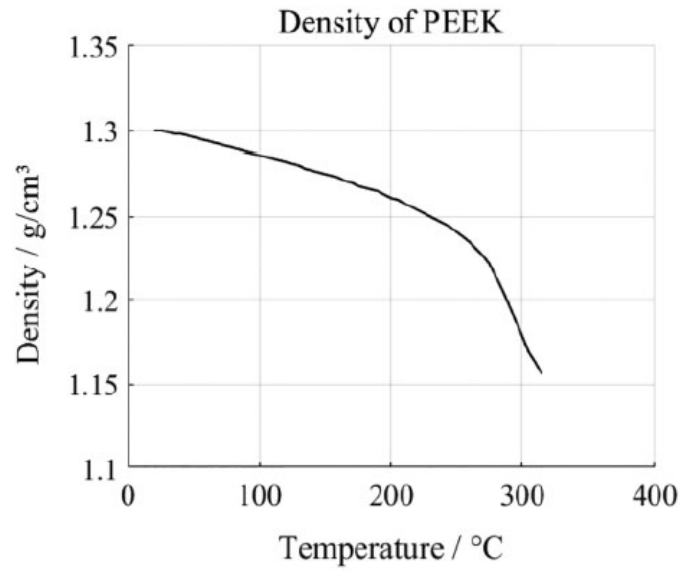


Figure 49. Temperature dependent density of PEEK [26].

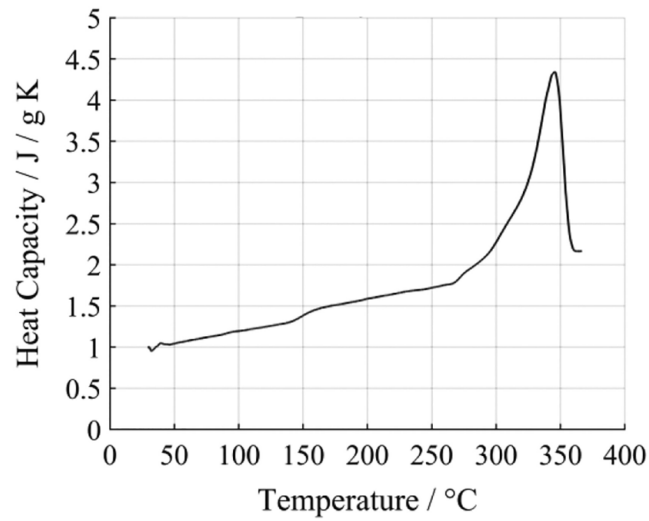


Figure 50. Specific heat capacity of PEEK as a function of temperature.

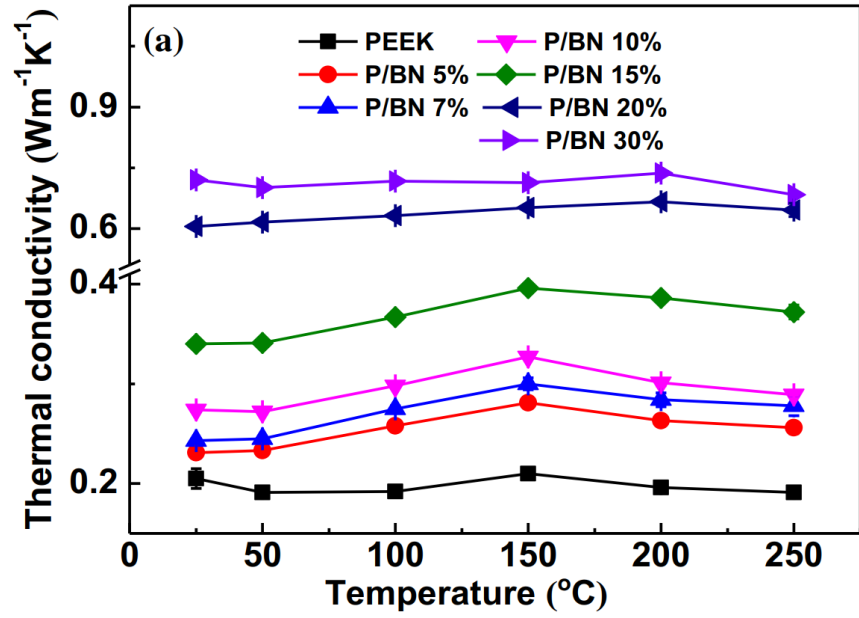


Figure 51. Thermal conductivity of PEEK as a function of temperature [27].

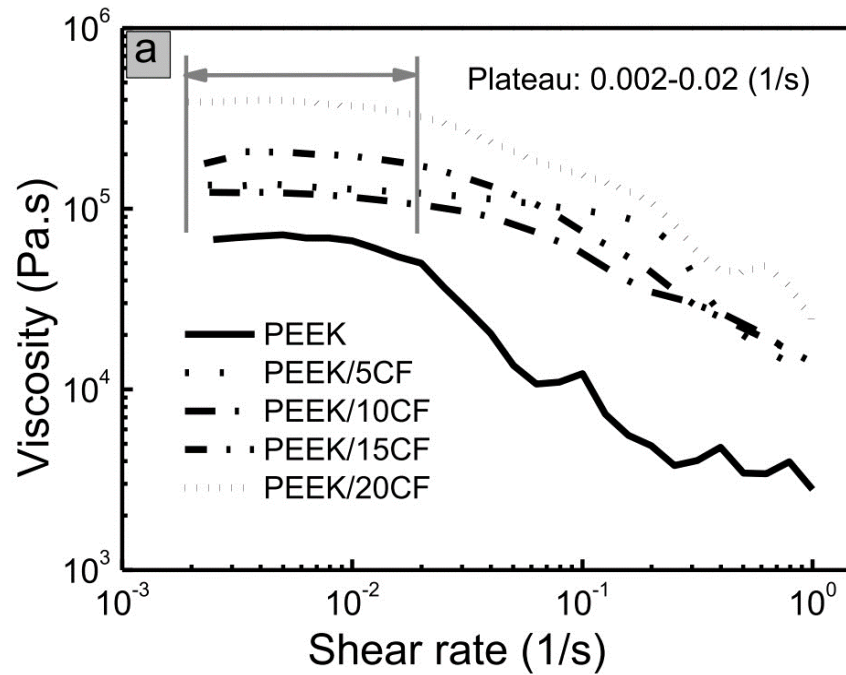


Figure 52. Viscosity behavior of PEEK with increasing shear rate [25].

#### 4.5.2 Boundary conditions

Figure 53 shows the coordinate system used in the simulation. Gravity was taken as  $9.81\text{m/s}^2$  along the negative Y-axis. The Y-axis was taken as the reference axis for simulation. The ambient temperature was set at 300K and all walls were given a default natural convection coefficient of  $10\text{W/m}^2\text{K}$  in the general setting of the simulation. Further, the following conditions were prescribed for the simulation.

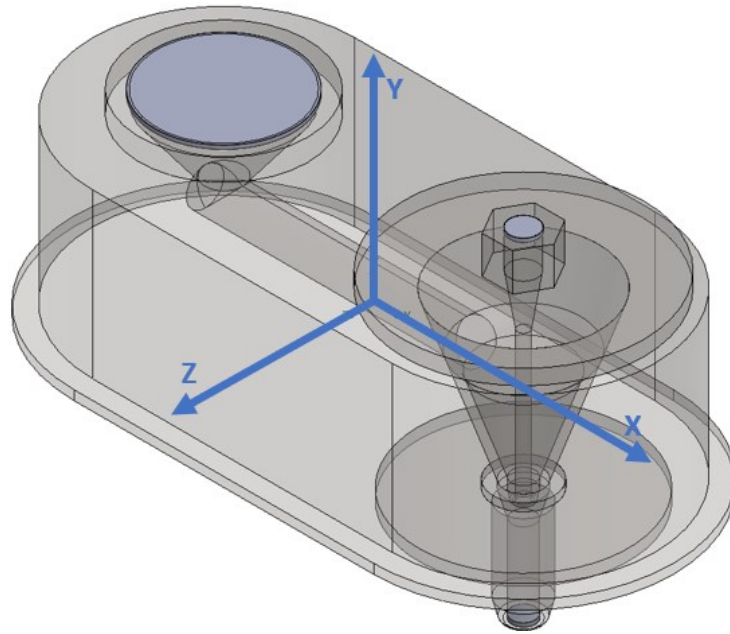


Figure 53. Simulation coordinate system.

1. Inlet mass flow rate (kg/s): This condition was set based on the experimental flow rate measurement at the extruder opening at  $360^\circ\text{C}$ . An initial analysis was conducted with a 500RPM motor speed which gives a mass flow rate of  $1.26\text{kg/hr}$  (see Table 28). The inlet mass flow rate was applied on the opening that interfaced with extruder, see Figure 54. Solidworks flow simulation takes mass flow rate in the units of kg/s, so the experimental mass flow rate values obtained were converted from kg/hr to kg/s for this purpose.

Table 28. Mass flow rate boundary condition for various screw motor speeds.

Screw motor speed (RPM)	Mass flow rate (kg/hr)
200	0.45
300	0.71
400	0.97
500	1.26
600	1.49
700	1.76
800	2.02
900	2.27

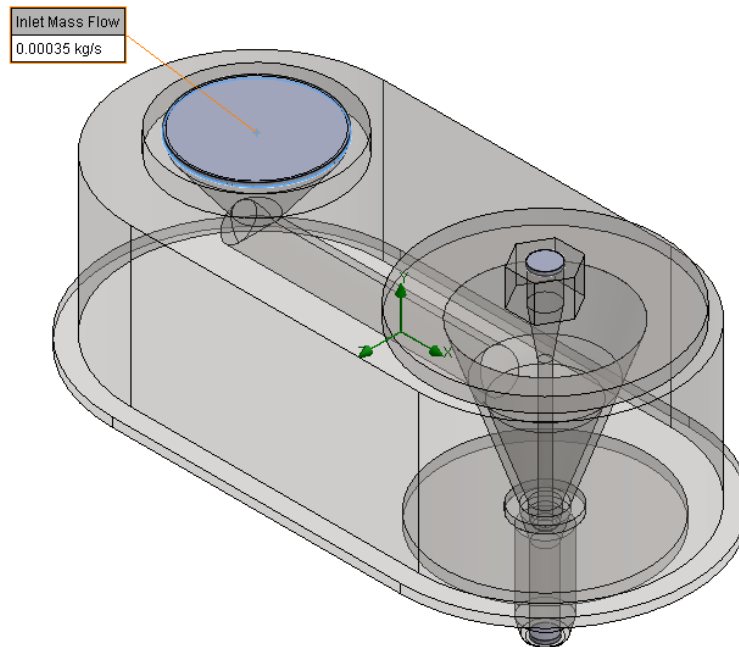


Figure 54. Inlet mass flow rate and the face it is applied to.

2. Environmental pressure (Pa): All other outlets open to the atmosphere were set to atmospheric pressure of 101325Pa. It was applied on the inner face of the lids covering the fiber feeding hole and the extrusion tip. Figure 55 shows the faces on which this pressure was applied.

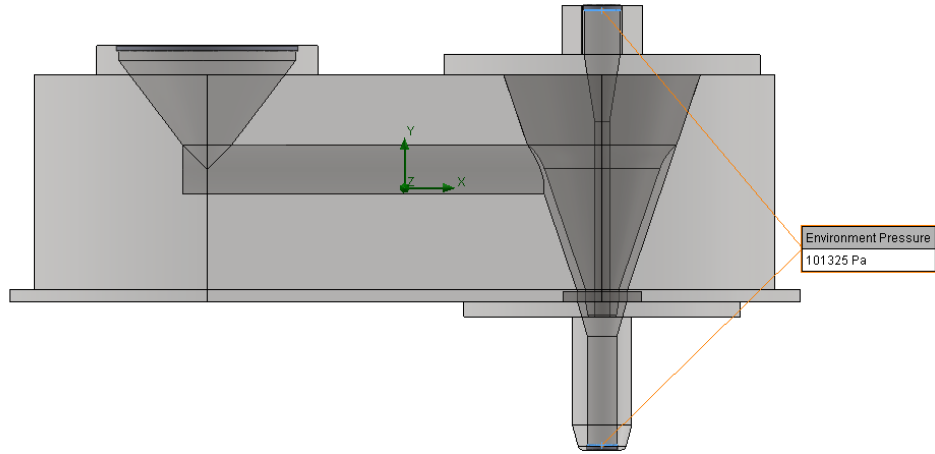


Figure 55. Environmental pressure and the faces it is applied to.

3. Outer wall 1: All the walls on which the heaters were designed to attach on were given an isothermal wall condition of 623.15K as the PEEK material properties are available for this temperature. Figure 56 shows the faces on which the isothermal condition was applied.

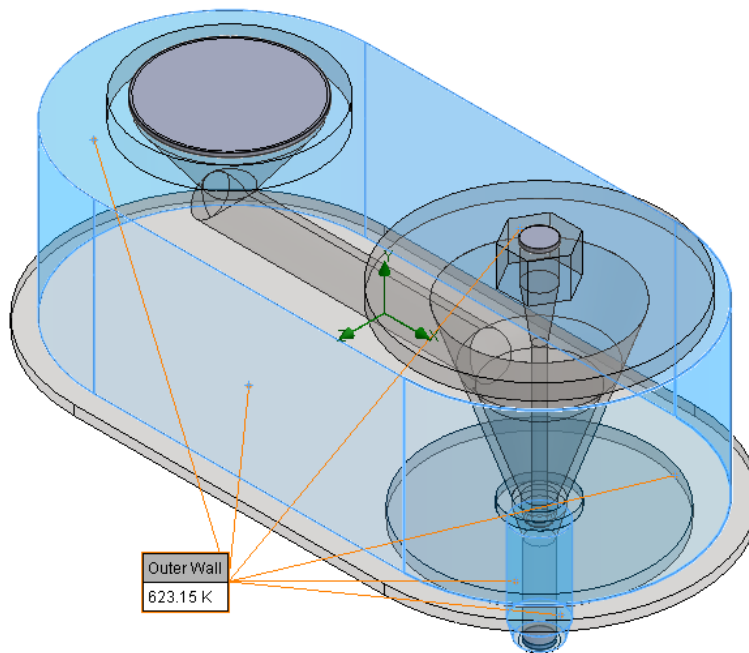


Figure 56. Faces in the assembly that will be heated.

4. Outer wall 2: Since the opening that interfaces with the extruder does not interface with the environment, it was not given a convective heat transfer boundary.

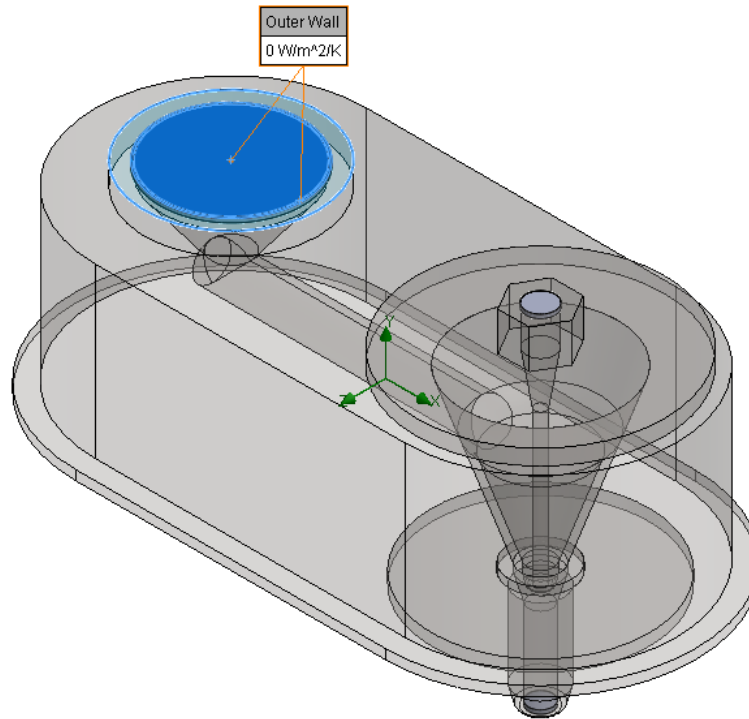


Figure 57. Faces on which there is no heat loss through convection.

#### 4.5.4 Meshing

The mesh generated for the simulation is shown in Figure 58. The section of interest was the impregnation length, carbon fiber feeding opening, and flow around the CF nozzle. As shown in the figure, the mesh in this section has been refined to capture flow behavior in great detail. Mesh refinement was carried out until a higher refined mesh did not produce a variation in the flow properties of PEEK. SolidWorks Flow Simulation uses tetrahedral shaped elements for meshing.

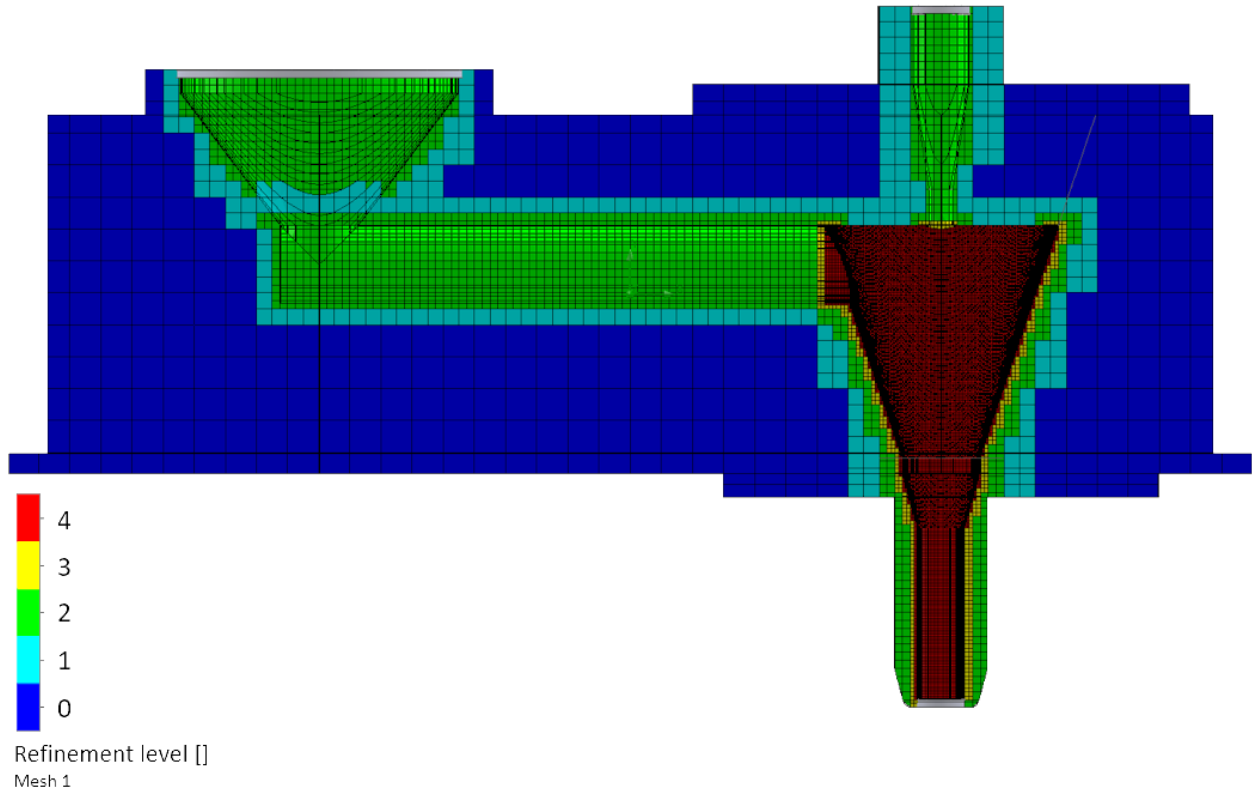


Figure 58. Mesh generated for the simulation.

#### 4.5.5 Results and discussion

An abbreviated discussion of the CFD analysis for the initial design is provided in Section 4.5.5.1. A more elaborated discussion of the CFD analysis is included for the final nozzle design as this embodiment was manufactured in response to the modeling work.

##### 4.5.5.1 CFD analysis for Design 1

Figure 59 and 60 shows the flow trajectory of molten PEEK for the initial design concept. As indicated by the velocity profile, the velocity of the PEEK flow in the PEEK pipe with flange part and around the CF nozzle part is nearly stagnant. This can lead to mass accumulation of PEEK in a real-life scenario causing clogging in these parts. The primary rationale behind the later design alteration was to transition to a significantly more compact flow orifice. In addition, there was a necessity to ease the nozzle assembly by reducing the number of components. The geometry of both the PEEK pipe with flange part and the PEEK + CF nozzle part needed to be modified to facilitate simpler manufacturing, assembly, and integration of heaters. These inputs were taken into consideration during the development of the final design.

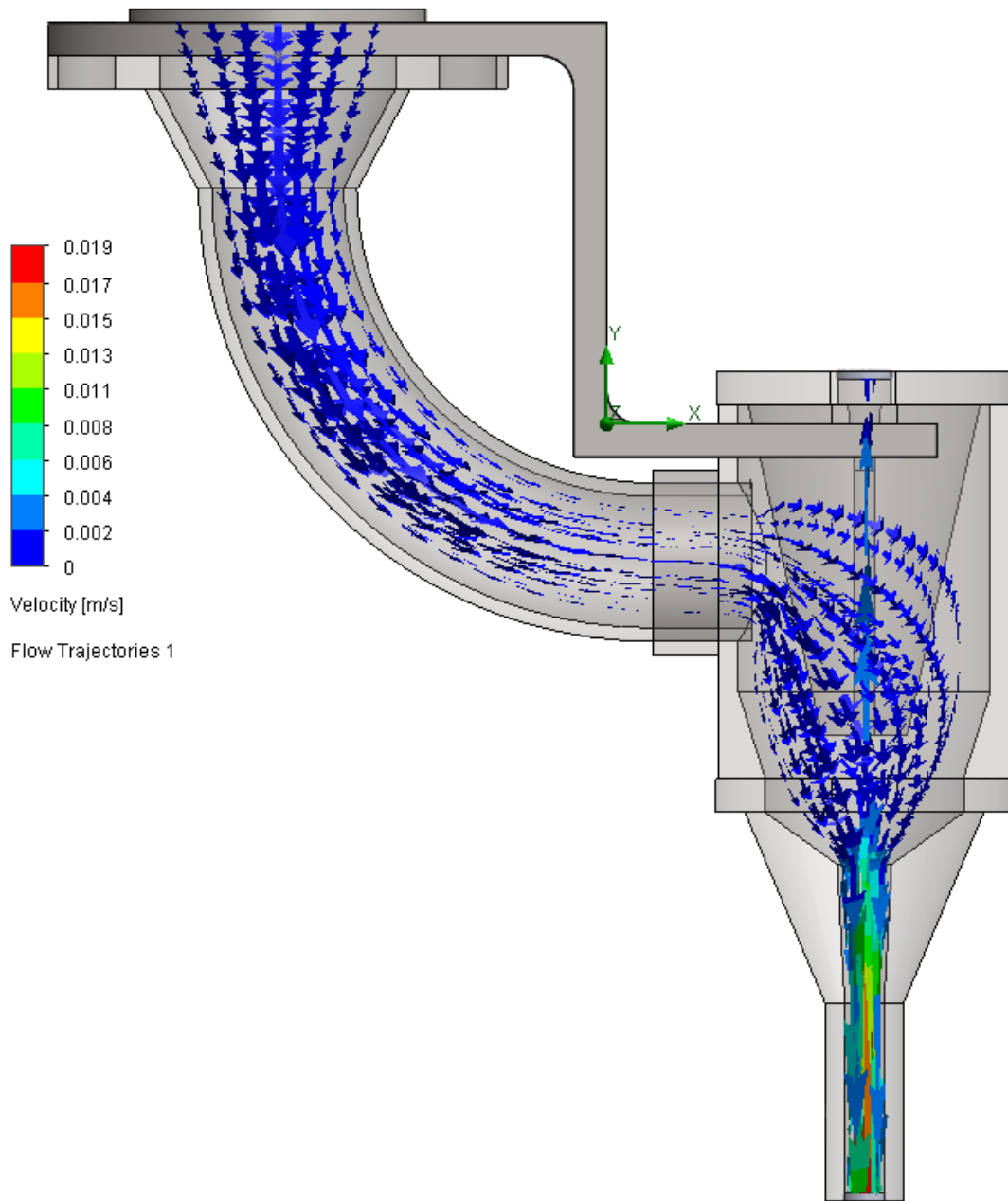


Figure 59. Flow trajectory with color gradient representing fluid flow velocity.

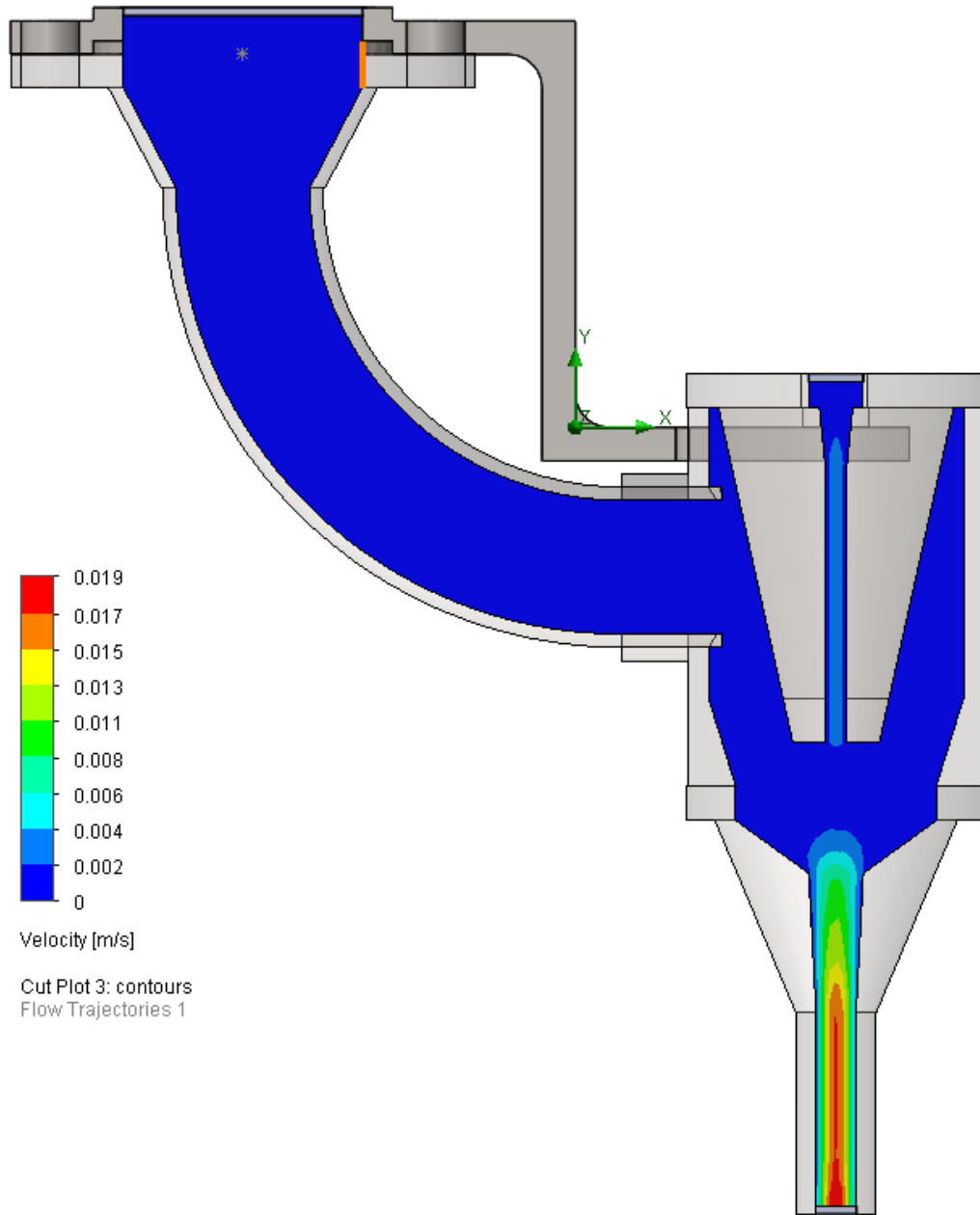


Figure 60. Velocity plot along the cross-section of the flow orifice.

#### 4.5.5.2 CFD analysis for final nozzle design

Three aspects of the design were simulated using the SolidWorks Flow Simulation package: Flow trajectory, extrusion velocity, and fiber pulling force. The following sections elaborate on these aspects and respective results.

### Flow trajectory:

The geometry of the CF Nozzle part was altered through iterations to achieve the following goals:

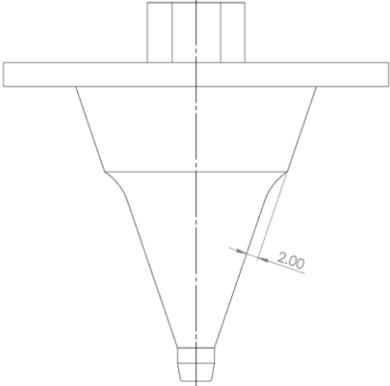
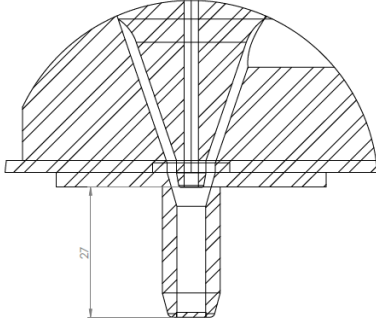
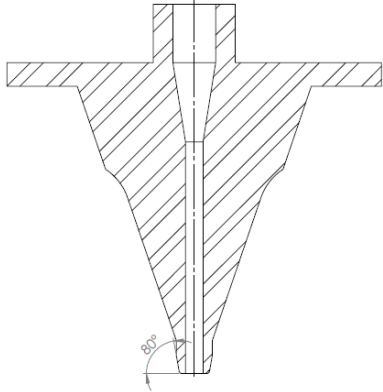
- Increase the flow rate at the point where fiber starts interfacing with molten PEEK, such that the fluid pressure at that point is minimal to eliminate an upward flow through the fiber insertion channel.
- Ensure an even flow around the conical section of the CF nozzle part.
- Ensure the elimination of mass accumulation around the conical section of CF nozzle part.

The length of the impregnation nozzle part was fixed at 30mm in order to reduce the vertical section through which PEEK flows to reduce the oozing of the molten material, a challenge of printing using the FGF method discussed in the previous chapter.

A parametric investigation into the geometric design of the nozzle components was performed. Table 29 provides a comprehensive overview of this study, focusing on three pivotal sections: the gap facilitating the flow and convergence of PEEK, the length of molten PEEK flow facilitating CF impregnation, and the tip angle of the CF nozzle. The table delineates the range and incremental steps for each parameter under examination, details the impact of varying geometries on flow parameters, and ultimately highlighting the optimal values selected for each.

Figure 61 shows the flow trajectory of molten PEEK through the channel with the color gradient for velocity profile. Figure 62 depicts a cut plot for the velocity profile for the central cross-section. Similarly, Figure 63 illustrates the pressure profile. The fluid velocity along central axis of the impregnation nozzle as shown in Figure 64 was plotted to find the convergence point of fluid flow at the carbon fiber entry. From the plot in Figure 65, it is evident that the flow converges at 0.37mm from the tip of the CF nozzle part which leaves an effective 26.63mm of impregnation length.

Table 29. Parametric study for study on the nozzle components

Changed geometry	Variation	Geometry	Effect of variation	Optimal Value
Gap around conical section around CF nozzle	1 – 3mm Analyzed in steps of 0.5mm		If the gap was too wide, mass accumulation was noticed with insufficient flow to all around the conical section. If the gap was too small, the PEEK exhibited a high-pressure section at tip of CF nozzle part leading to flow in fiber insertion channel	2mm
Impregnation length*	24 – 27.5mm Analyzed in steps of 0.5mm		Ideally, the length should be maximized for better fiber impregnation, but if the length is increased beyond optimal value, polymer flows into the fiber insertion channel and	27mm
Tip angle of CF nozzle	65 – 90° Analyzed in steps of 5°		The higher the angle the convergence point of the polymer moves away from the tip of the fiber insertion point. The angle cannot reduce below an optimal value for manufacturing feasibility.	80°

\*Drawing shown is a snippet of detailed view from assembly. Refer Appendix 2 for the complete drawing.

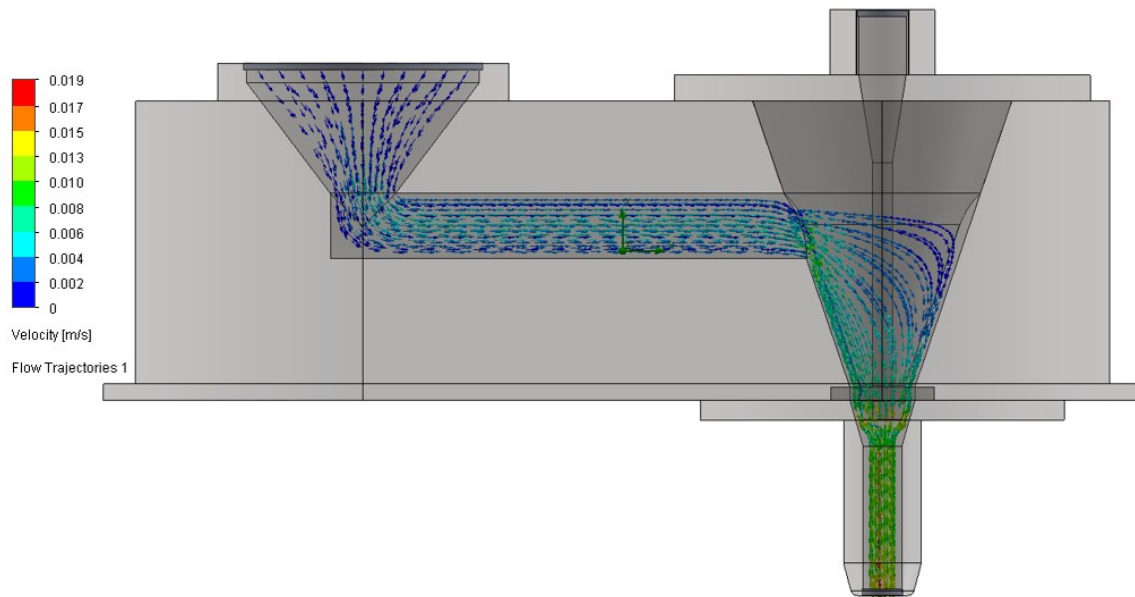


Figure 61. Flow trajectory of polymer in the final nozzle design.

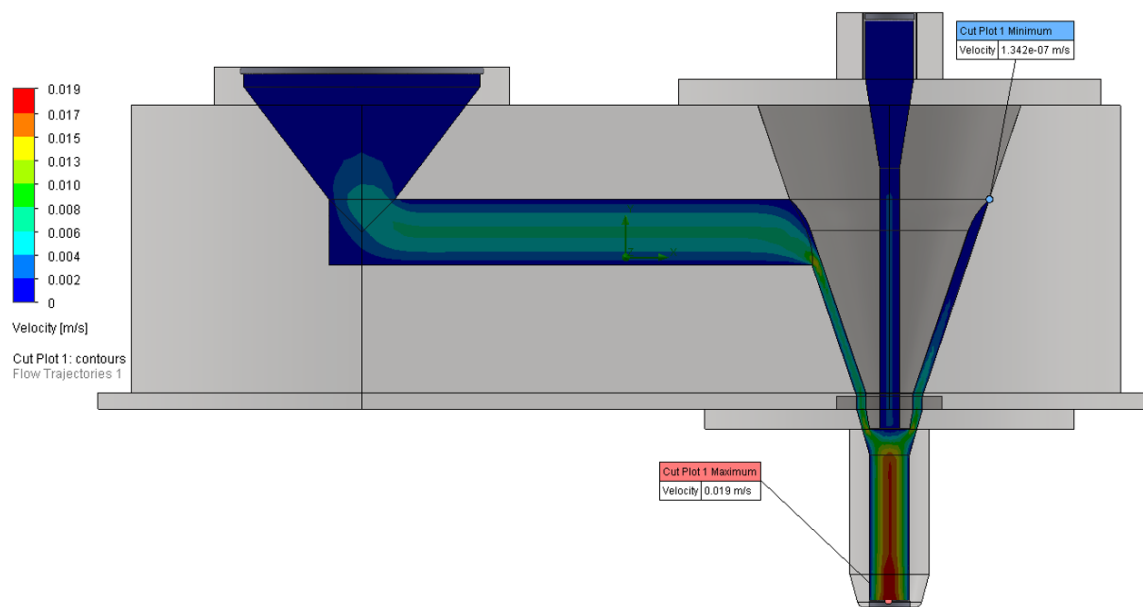


Figure 62. Velocity profile of polymer at cross-section in final nozzle design.

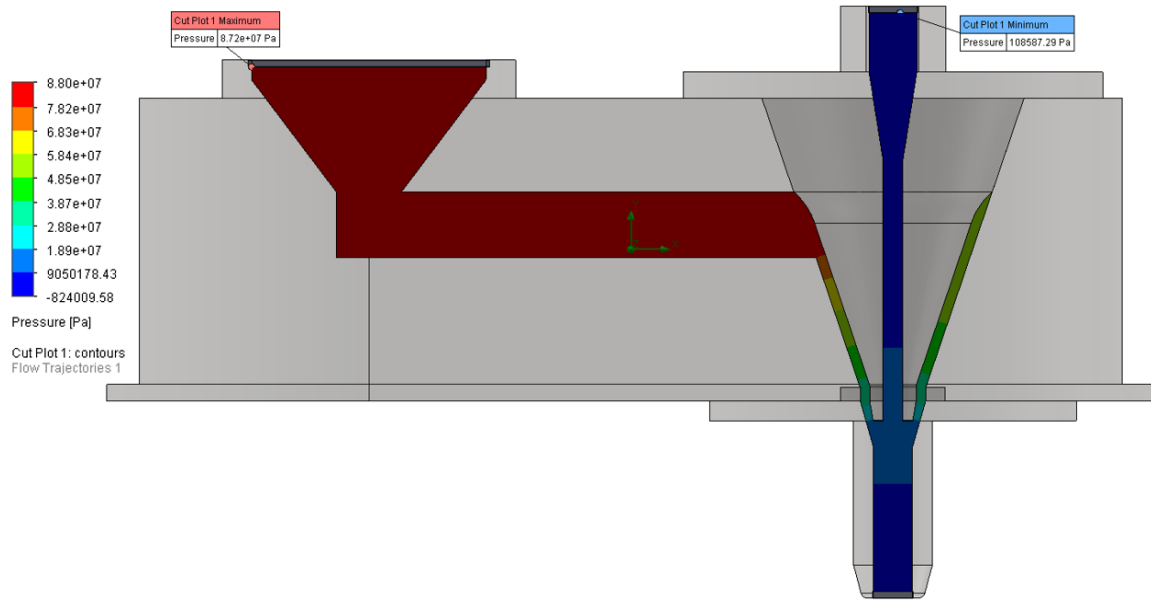


Figure 63. Pressure profile of polymer at cross-section in final nozzle design.

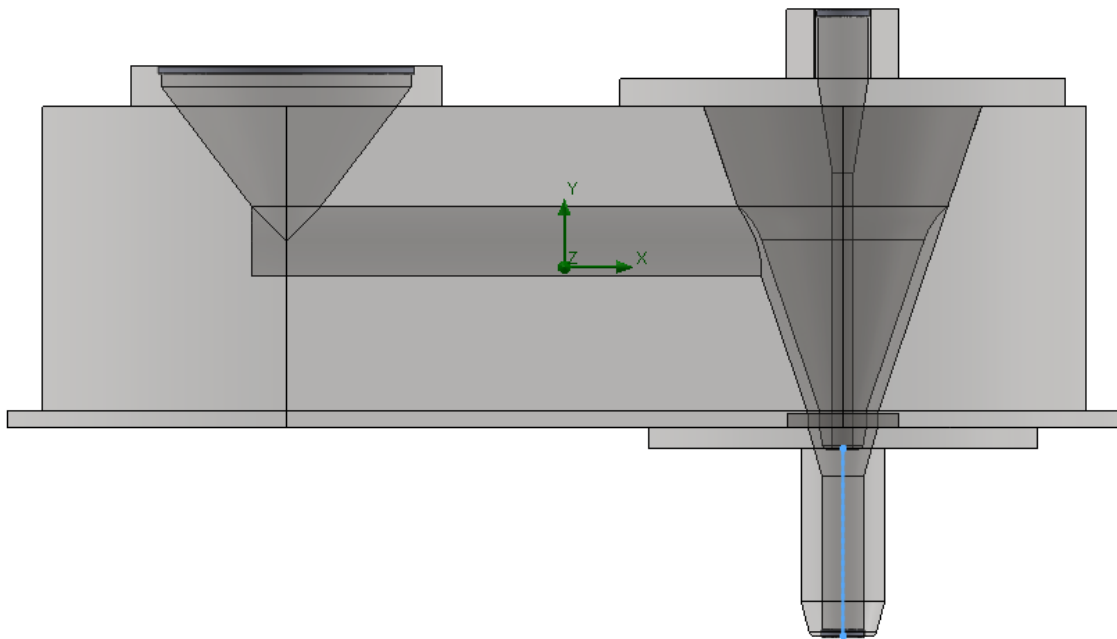


Figure 64. Illustration depicting the axis along which velocity is measured.

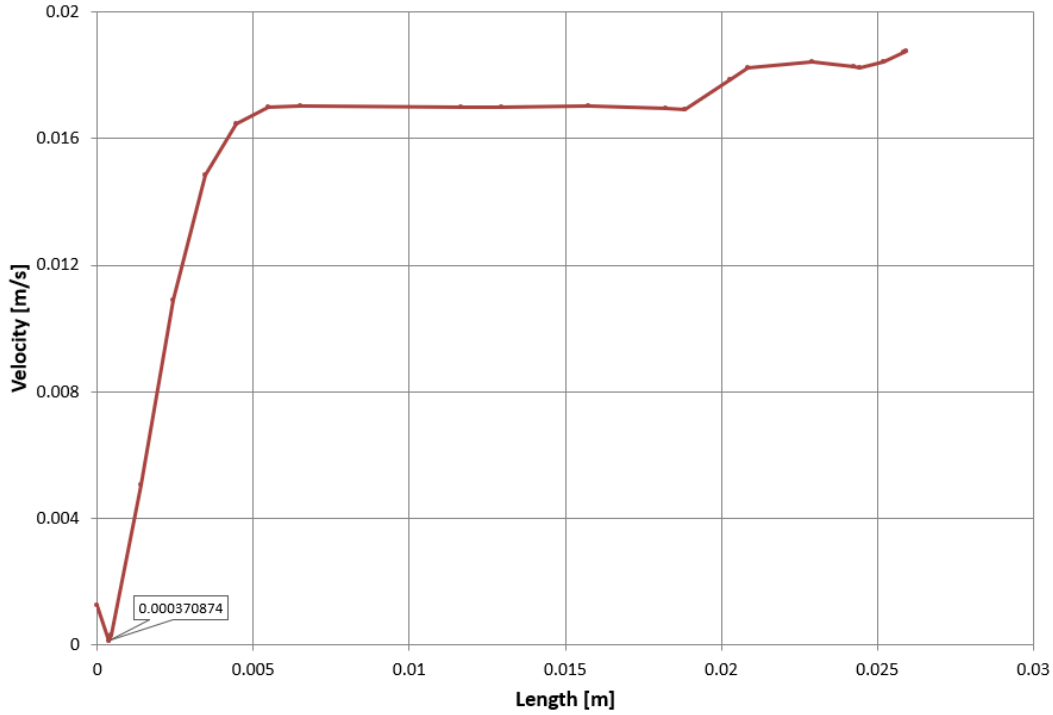


Figure 65. Velocity plot along the central axis of the impregnation nozzle.

Extrusion velocity:

After finalizing the geometry of the parts, a prediction of the extrusion velocity at the nozzle tip for various screw motor speeds was carried out. A comprehensive analysis of the flow trajectory was conducted, considering fluid pressure and velocity flow trajectories for each of the screw motor speeds, see Table 30. This analysis is essential to ensure the absence of mass accumulation points and to verify that there was no unintended flow through the fiber insertion channel. The surface goal function for average velocity through a surface [141] was used to calculate these values. Due to the small input mass flow rate at 200 and 300RPM screw motor speed, there is a quasi-stagnant fluid flow section in the flow channel. From the analysis, it is recommended to use the nozzle above 400RPM screw motor speeds with the current extruder.

Table 30. Predicted extrusion velocity for 5mm nozzle with varying screw motor speed

Screw motor speed (RPM)	Mass flow rate (kg/s)	Avg extrusion velocity at nozzle tip (mm/s)	Flow through fiber insertion channel	Mass accumulation in flow
200	0.000124	3.5	No	Yes
300	0.000198	5.5	No	Yes
400	0.000270	7.5	No	No
500	0.000350	10	No	No
600	0.000415	11	No	No
700	0.000490	13	No	No
800	0.000560	15	No	No
900	0.000630	17	No	No

#### 4.5.5.2.3 Fiber pulling force

As per the design concept, the fiber feeding should take place primarily through viscous drag force the molten PEEK material exerts on the fiber tow. To ensure there will be sufficient pulling force on the fiber, a simulation was carried out to measure this force. For this, a carbon fiber tow was introduced into the assembly as shown in Figure 66. The material for the tow was assigned as the carbon fiber material available in the SolidWorks Engineering Database and the size of the tow was roughly estimated from the 24K carbon fiber tow available for the experiments. To simplify the problem, impregnation of the fiber was not considered at this point. The viscous drag force on the peripheral surface of the tow was measured along the length of the tow in the simulation.

Referring to Table 31, Surface Goal Force (SG Force, refers to the force calculation on a surface for the solver to calculate the forces applied on the surface in Solidworks Flow Simulation) denotes the resultant force applied on the fiber tow and SG Force (Y) denotes the component of force applied along the Y direction. A force of  $\sim 16\text{N}$  was found to be applied on the fiber tow, since only a slight pulling force was required the resultant force was deemed sufficient to feed the fiber during printing [148]. Additionally, if the commingled fibers are preprocessed to make the tows stiff by melting the PEEK, a pushing force can be applied to aid the fiber feeding force. Since the resultant force and force along Y direction are the same, there is no force component in X and Z directions, this means that the fiber tow will be centered during the extrusion process.

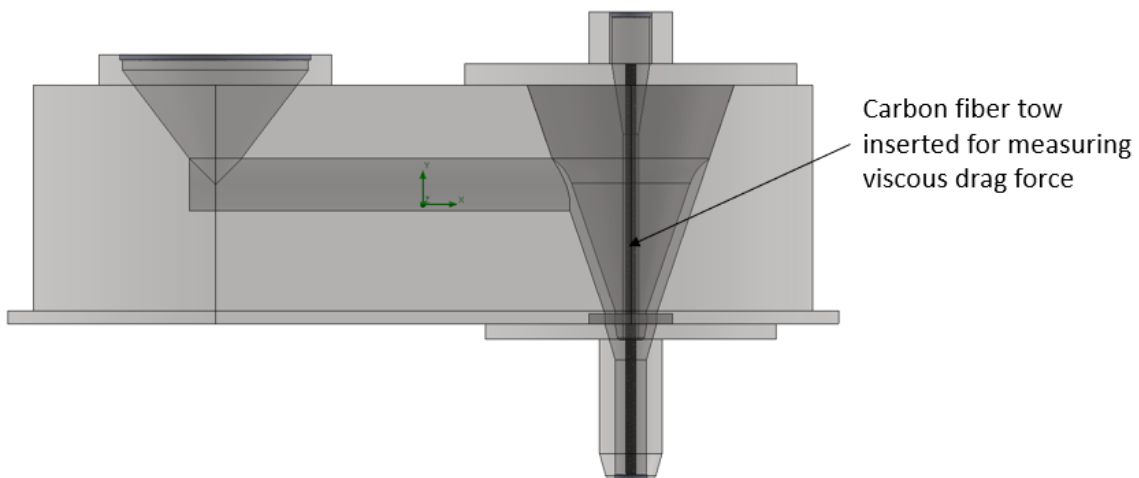


Figure 66. CAD model with the carbon fiber tow used for viscous force calculation simulation.

Table 31 . Surface force measured along the fiber surface.

Goal name	Unit	Value	Avg value	Min value	Max value	Progress [%]	Use in convergence	Delta	Criteria
SG force	[N]	16.017	16.051	16.008	16.098	100	Yes	0.035	0.045
SG force (Y)	[N]	-16.017	-16.051	-16.008	-16.098	100	Yes	0.035	0.045

#### 4.6 Integration of nozzle with extruder

All the parts of the nozzle were manufactured out of AISI 304 stainless steel. Manufacturing drawings for all the parts of the final design is available in Appendix 2. A sleeve heater was designed and manufactured for heating the PEEK block part. The heater is a 1200W coil heater embedded into a sleeve that fits snugly on the slot shape of PEEK block. An RTD sensor was placed in the PEEK block to measure the PEEK block temperature and control the heater. The impregnation nozzle is fitted with a coil heater of 200W. The coil heater has a thermocouple embedded into it to control the heater temperature. The Figure 69 shows the assembly of the nozzle with the extruder.

As an initial test print, extrusion with commingled fiber failed as the fibers did not have any rigidity thus had difficulty feeding through the CF feeding channel. Instead, a strand of carbon fiber reinforced in PEEK was extruded as shown in Figure 69 using a Synergex 24K CF tow with Polyurethane coating provided by COATS (London, UK). The polyurethane sizing provided adequate rigidity to the fibers and kept the fibers intact during the feeding process. Table 32 shows the set of parameters that were used to extrude the carbon fiber. Parameters were chosen by trial and error for the initial test print. Printed strands had a fiber volume fraction of 5.3%. A variation in volume percentage was found in the measurement which can attributed to inconsistencies in the diameter of the bead extruded. Further optimization of parameters is required to control the fiber volume fraction. The low volume fraction is due to the low fiber count tow used for extrusion due to the limited availability of the higher fiber count tows at the time of the experiments.

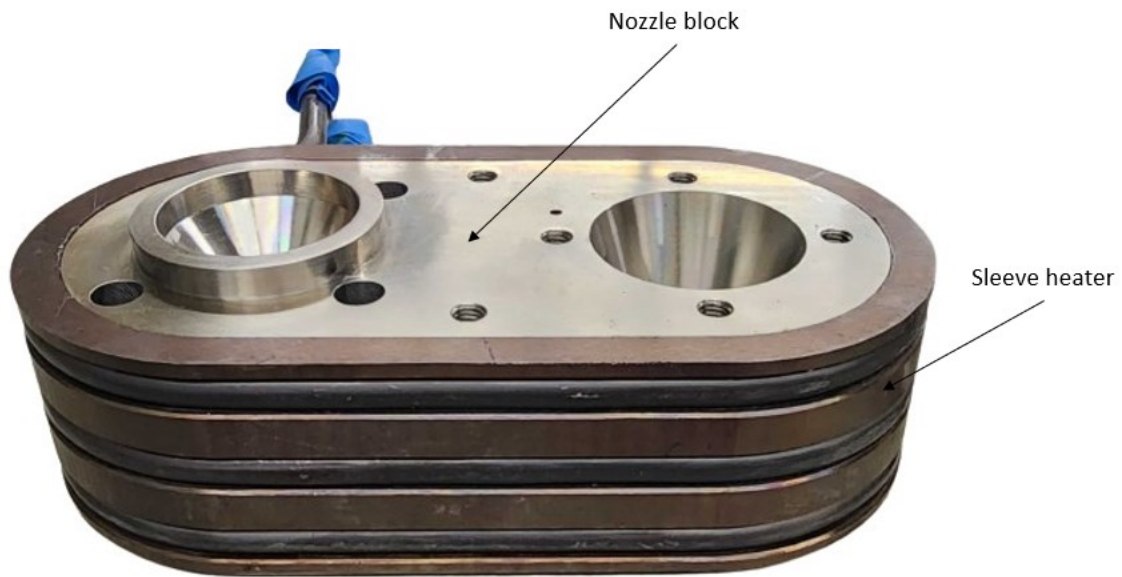


Figure 67. Sleeve heater assembly on PEEK block part.



Figure 68. Coil heater assembly on 5mm nozzle



Figure 69. Extrusion trial using newly designed nozzle

Table 32. Parameters used for initial testing of nozzle.

Parameter	Value
Extruder temperature (°C)	370
Screw motor speed (RPM)	500
Nozzle diameter (mm)	5

## **4.7 Conclusions**

A novel nozzle was designed to print continuous fiber reinforced thermoplastics. CFD analyses were conducted on design concepts to optimize flow channel geometries. The analysis conducted gave confidence that molten PEEK can flow through the intended channel and produce sufficient pulling force to feed the fiber. The nozzle was manufactured and integrated with the extruder. An initial test print of carbon fiber reinforced PEEK was performed, resulting in a fiber volume fraction of 5.3% for the extruded bead at a screw motor speed of 500RPM with a 5mm nozzle at 370°C.

# Chapter 5 Conclusions and future work

## 5.1 Conclusions

In the initial phase of this research, an exploration of the feasibility and challenges associated with additive manufacturing of high-performance engineering polymers was undertaken. Building on this foundation, the study delved into the feasibility of printing continuous fiber-reinforced polymers. Technical insights pertaining to large-scale additive manufacturing, high-performance thermoplastic 3D printing, continuous fiber-reinforced polymer additive manufacturing, and mechanisms and designs for CFRP printing were reviewed, drawing guidance from the available literature.

A large-scale material extrusion based additive manufacturing system was developed to print high-performance engineering thermoplastics. For this specific work PEEK polymer was employed. The system uses a screw-based extruder commonly used for injection molding for extruding material. The extruder has a capability of a maximum 2.5kg/hr throughput while coupled with a 4mm nozzle. The screw extruder was modified to maintain a continuous operating temperature up to 400°C. The extruder has a rated torque of 60Nm sufficient for commonly used thermoplastics in engineering applications. The screw extruder was assembled onto a six-axis robotic arm capable of 2000mm lateral motion and 3500mm vertical motion. Thus, the AM system has an effective build volume of ~14m<sup>3</sup>.

In order to facilitate printing with the system, a thorough investigation into the process parameters influencing the fused granular fabrication process was conducted. All experiments were executed using a 4mm nozzle. The initial step in the parametric study involved establishing a relationship between mass flow rate and screw motor speed. The scanning velocity was calculated using layer height, nozzle diameter, and extrusion velocity based on the equation from [127]. Additionally, the bead width was measured by varying layer height, extrusion velocity, and extruder temperature. An empirical relation between these parameters and the bead width was established through a regression analysis. To minimize inter-bead voids and surface deformities, a design of experiments study was conducted. The layer height, extrusion velocity, and bead overlap were varied during the experimentation. Statistical analysis of the DoE data revealed that bead overlap was the most significant parameter affecting both inter-bead void formation and surface deformity. Utilizing the response optimization tool in the Minitab software, an optimal set of process parameters was determined for a 4mm nozzle to be a screw motor speed (extrusion velocity) of 400 RPM, a layer height of 3mm, and an overlap percentage of 17%. The predicted response, with 0.3% inter-bead void and 1.17mm

surface uniformity, was evaluated and demonstrated successful printing with 0% inter-bead void and an average uniformity of 1.25mm.

The study provided a comprehensive understanding of the challenges associated with printing high-performance semi-crystalline polymers such as PEEK. Delamination between layers and warping were significant issues encountered in the initial stages of the research. To address these challenges, three 750W IR heaters were strategically installed around the print area to regulate the cooling rate of the deposited bead, effectively eliminating delamination and mitigating warping. While warping persists for specific geometries due to the rate of crystallization of PEEK polymer, further exploration into the crystallization behavior is deemed necessary for a more nuanced understanding. Bed adhesion posed another substantial challenge, given the non-polar nature of PEEK, requiring a superhydrophobic surface for adhesion. To address this, a laser texturing process was employed to create a parallel peak and valley pattern on the AISI 304 stainless steel print surface, with an average maximum height of 0.37mm. Additionally, the print surface was heated between 200°C and 220°C. Molten PEEK oozing out of the nozzle under the influence of gravity presented another obstacle. This occurrence was considered a design requirement for the development of the nozzle for printing polymer with continuous fiber reinforcement. The issue was successfully resolved by optimizing the nozzle design, specifically by reducing the vertical section through which PEEK material flows.

Leveraging insights into the critical process parameters influencing the fused granular fabrication process, the viscous material characteristics of PEEK, and diverse impregnation techniques for fiber composites, a pioneering nozzle was conceptualized. Computational fluid dynamics (CFD) analysis was executed on the design to refine the flow channel geometry, optimizing the fiber impregnation process, controlling the trajectory of polymer flow along the intended path, and ensuring consistent polymer flow. The analysis also confirmed that the viscous forces exerted by the polymer flow were sufficient for the fiber feeding mechanism.

Subsequently, the designed nozzle parts were manufactured using AISI 304 stainless steel material. The fabricated components were assembled and integrated with the extruder. In an initial trial, a 24K carbon fiber tow was extruded, employing parameters selected by train and error, including a screw motor speed of 500 RPM, material temperature of 370°C, and an impregnation nozzle size of 5mm. The outcome of this trial was the successful extrusion of carbon fiber reinforced PEEK, with a volume percentage of approximately 5.3%. This marked a significant milestone in validating the functionality of the designed nozzle for continuous fiber reinforced polymer printing.

## 5.2 Future work

The printing system developed ties into an umbrella of a project that aims at developing effective printing strategies for continuous fiber reinforced polymer and will be used as the experimental setup for the studies that are to be conducted for the same. Additionally, the continuation of the study can be taken through various avenues such as:

- Studying the crystallization behavior of PEEK polymer while 3D printing in order to eliminate the challenges of warping.
- Mechanical characterization of the printed parts can be carried out for validation and prediction of performance.
- In-situ process inspection of printing is another possibility to continue the study where process parameters are altered for subsequent layers based on the previously deposited layers to improve print quality.
- The system designed for printing continuous fiber reinforced polymer has to be further optimized for consistent extrusion and bead width. Furthermore, a higher volume percentage of fiber has to be achieved in order to be industrially applicable. For this, a process parameter study with the nozzle has to be conducted to obtain optimal printing parameters.
- The fiber impregnation characteristics of the nozzle can be studied, and design improvements can be brought about to produce parts suitable for industrial application.

## References

- [1] Gibson, I., Rosen, D., Stucker, B., & Khorasani, M. (2021). *Additive Manufacturing Technologies*. <https://doi.org/10.1007/978-3-030-56127-7>
- [2] J. Scott et al., “Additive Manufacturing: Status and Opportunities,” Science and Technology Policy Institute, pp. 1–29, Mar. 2012. doi: [https://www.researchgate.net/profile/Justin-Scott-4/publication/312153354\\_Additive\\_Manufacturing\\_Status\\_and\\_Opportunities/links/59e786db458515c3630f917b/Additive-Manufacturing-Status-and-Opportunities.pdf](https://www.researchgate.net/profile/Justin-Scott-4/publication/312153354_Additive_Manufacturing_Status_and_Opportunities/links/59e786db458515c3630f917b/Additive-Manufacturing-Status-and-Opportunities.pdf)
- [3] Babu, S. S., Love, L., Dehoff, R., Peter, W., Watkins, T. R., & Pannala, S. (2015). Additive Manufacturing of materials: Opportunities and challenges. *MRS Bulletin*, 40(12), 1154–1161. <https://doi.org/10.1557/mrs.2015.234>
- [4] van de Werken, N., Tekinalp, H., Khanbolouki, P., Ozcan, S., Williams, A., & Tehrani, M. (2020). Additively manufactured carbon fiber-reinforced composites: State of the art and perspective. *Additive Manufacturing*, 31, 100962. <https://doi.org/10.1016/j.addma.2019.100962>
- [5] Ahuja, B., Karg, M., & Schmidt, M. (2015). Additive manufacturing in production: Challenges and opportunities. *Laser 3D Manufacturing II*. <https://doi.org/10.1117/12.2082521>
- [6] Huang, Y., Leu, M. C., Mazumder, J., & Donmez, A. (2015). Additive manufacturing: Current State, future potential, gaps and needs, and recommendations. *Journal of Manufacturing Science and Engineering*, 137(1). <https://doi.org/10.1115/1.4028725>
- [7] Dawoud, M., Taha, I., & Ebeid, S. J. (2016). Mechanical behaviour of ABS: An experimental study using FDM and injection moulding techniques. *Journal of Manufacturing Processes*, 21, 39–45. <https://doi.org/10.1016/j.jmapro.2015.11.002>
- [8] Torrado, A. R., Shemelya, C. M., English, J. D., Lin, Y., Wicker, R. B., & Roberson, D. A. (2015). Characterizing the effect of additives to ABS on the mechanical property anisotropy of specimens fabricated by material extrusion 3D printing. *Additive Manufacturing*, 6, 16–29. <https://doi.org/10.1016/j.addma.2015.02.001>
- [9] Wittbrodt, B., & Pearce, J. M. (2015). The effects of PLA color on material properties of 3-D printed components. *Additive Manufacturing*, 8, 110–116. <https://doi.org/10.1016/j.addma.2015.09.006>
- [10] Suryanegara, L., Nakagaito, A. N., & Yano, H. (2009). The effect of crystallization of PLA on the thermal and mechanical properties of microfibrillated cellulose-reinforced PLA composites. *Composites Science and Technology*, 69(7–8), 1187–1192. <https://doi.org/10.1016/j.compscitech.2009.02.022>
- [11] Yeh, S.-K., Agarwal, S., & Gupta, R. K. (2009). Wood–plastic composites formulated with virgin and recycled ABS. *Composites Science and Technology*, 69(13), 2225–2230. <https://doi.org/10.1016/j.compscitech.2009.06.007>
- [12] Admin. (2015, May 21). *Understanding shrink rates*. The Tool Hub -. <https://thetoolhub.com/part-design/shrink/>

- [13] Brenken, B., Barocio, E., Favaloro, A., Kunc, V., & Pipes, R. B. (2019). Development and validation of extrusion deposition additive manufacturing process simulations. *Additive Manufacturing*, 25, 218–226. <https://doi.org/10.1016/j.addma.2018.10.041>
- [14] Boiko, Y. M., Guérin, G., Marikhin, V. A., & Prud'homme, R. E. (2001). Healing of interfaces of amorphous and semi-crystalline poly(ethylene terephthalate) in the vicinity of the glass transition temperature. *Polymer*, 42(21), 8695–8702. [https://doi.org/10.1016/s0032-3861\(01\)00406-2](https://doi.org/10.1016/s0032-3861(01)00406-2)
- [15] Wang, Z., Bi, X., Liu, B., Xu, M., & Dong, Z. (2021). Adhesion enhancement of peek/6161-T6 FLJ joints via laser surface modification. *Composites Part B: Engineering*, 216, 108797. <https://doi.org/10.1016/j.compositesb.2021.108797> [33] Das, A., Chatham, C. A., Fallon, J. J., Zawaski, C. E., Gilmer, E. L., Williams, C. B., & Bortner, M. J. (2020). Current understanding and challenges in high temperature additive manufacturing of engineering thermoplastic polymers. *Additive Manufacturing*, 34, 101218. <https://doi.org/10.1016/j.addma.2020.101218>
- [16] Isobe, T., Tanaka, T., Nomura, T., & Yuasa, R. (2018). Comparison of strength of 3D printing objects using short fiber and continuous long fiber. *IOP Conference Series: Materials Science and Engineering*, 406, 012042. <https://doi.org/10.1088/1757-899x/406/1/012042>
- [17] Mehl, K., Schmeer, S., Motsch-Eichmann, N., Bauer, P., Müller, I., & Hausmann, J. (2021). Structural optimization of locally continuous fiber-reinforcements for short fiber-reinforced plastics. *Journal of Composites Science*, 5(5), 118. <https://doi.org/10.3390/jcs5050118>
- [18] Stock, T., & Seliger, G. (2016). Opportunities of sustainable manufacturing in industry 4.0. *Procedia CIRP*, 40, 536–541. <https://doi.org/10.1016/j.procir.2016.01.129>
- [19] Global Additive Manufacturing Market, forecast to 2025 - Namic. (n.d.). [https://namic.sg/wp-content/uploads/2018/04/global-additive-manufacturing-market\\_1.pdf](https://namic.sg/wp-content/uploads/2018/04/global-additive-manufacturing-market_1.pdf)
- [20] Lund-Nielsen, P. (n.d.). *3D printing is transforming the construction industry*. SME. <https://www.sme.org/technologies/articles/2022/june/3d-printing-is-transforming-the-construction-industry/>
- [21] Zhang, W., Hou, W., Deike, L., & Arnold, C. B. (2020). Using a dual-laser system to create periodic coalescence in laser powder bed fusion. *Acta Materialia*, 201, 14–22. <https://doi.org/10.1016/j.actamat.2020.09.071>
- [22] Goodridge, R., & Ziegelmeier, S. (2017). Powder bed fusion of polymers. *Laser Additive Manufacturing*, 181–204. <https://doi.org/10.1016/b978-0-08-100433-3.00007-5>
- [23] Wen, S. F., Yan, C. Z., Wei, Q. S., Zhang, L. C., Zhao, X., Zhu, W., & Shi, Y. S. (2014). Investigation and development of large-scale equipment and high performance materials for powder bed laser fusion additive manufacturing. *Virtual and Physical Prototyping*, 9(4), 213–223. <https://doi.org/10.1080/17452759.2014.949406>
- [24] Gülcan, O., Günaydın, K., & Tamer, A. (2021). The state of the art of material jetting—A critical review. *Polymers*, 13(16), 2829. <https://doi.org/10.3390/polym13162829>
- [25] Elkaseer, A., Chen, K. J., Janhsen, J. C., Refle, O., Hagenmeyer, V., & Scholz, S. G. (2022). Material jetting for advanced applications: A state-of-the-art review, gaps and future directions. *Additive Manufacturing*, 60, 103270. <https://doi.org/10.1016/j.addma.2022.103270>

- [26] Sasahara, H., Tsutsumi, M., & Chino, M. (2005). Development of a layered manufacturing system using sheet metal-polymer lamination for mechanical parts. *The International Journal of Advanced Manufacturing Technology*, 27(3–4), 268–273. <https://doi.org/10.1007/s00170-004-2163-y>
- [27] Ntousia, M., & Fudos, I. (2019). 3D Printing Technologies & Applications: An overview. *Proceedings of CAD'19*. <https://doi.org/10.14733/cadconf.2019.243-248>
- [28] Suwanpreecha, C., & Manonukul, A. (2022). A review on material extrusion additive manufacturing of metal and how it compares with Metal Injection Moulding. *Metals*, 12(3), 429. <https://doi.org/10.3390/met12030429>
- [29] Altıparmak, S. C., Yardley, V. A., Shi, Z., & Lin, J. (2022). Extrusion-based additive manufacturing technologies: State of the art and future perspectives. *Journal of Manufacturing Processes*, 83, 607–636. <https://doi.org/10.1016/j.jmapro.2022.09.032>
- [30] Masood, S. H. (2014). Advances in fused deposition modeling. *Comprehensive Materials Processing*, 69–91. <https://doi.org/10.1016/b978-0-08-096532-1.01002-5>
- [31] Kalle, J., Joni, K., Alexander, S., & Juhani, O. (2023). Potential and challenges of fused granular fabrication in patternmaking. *International Journal of Metalcasting*, 17(4), 2469–2476. <https://doi.org/10.1007/s40962-023-00989-9>
- [32] *The factory of the future: 3D demonstrators*. The Factory of The Future: 3D Demonstrators. (n.d.). <https://www.stratasys.com/en/demonstrators/>
- [33] Ali, Md. H., Kurokawa, S., Shehab, E., & Mukhtarkhanov, M. (2023). Development of a large-scale multi-extrusion FDM printer, and its challenges. *International Journal of Lightweight Materials and Manufacture*, 6(2), 198–213. <https://doi.org/10.1016/j.ijlmm.2022.10.001>
- [34] Pignatelli, F., & Percoco, G. (2022). An application- and market-oriented review on large format additive manufacturing, focusing on polymer pellet-based 3D printing. *Progress in Additive Manufacturing*, 7(6), 1363–1377. <https://doi.org/10.1007/s40964-022-00309-3>
- [35] *3D printer catalog*. Aniwaa. (2022, January 27). <https://www.aniwaa.com/catalog/3d-printers/?sort=relevancy&order=desc&display=list&show=12&paged=1>
- [36] *Jupiter*. ATMAT. (n.d.). <https://atmat.pl/jupiter-en>
- [37] *BigRep Pro: Industrial Large-format 3D printer for professionals*. BigRep Industrial 3D Printers. (2023, September 5). <https://bigrep.com/bigrep-pro/>
- [38] *D1000*. Bootstrap. (n.d.). <https://www.creatbot.com/en/creatbot-D1000.html#tech-Specs>
- [39] Villa, D., & Moretti, F. (2023, September 21). *Delta Wasp 60100*. WASP. <https://www.3dwasp.com/en/large-format-3d-printer-delta-wasp-60100/>
- [40] We've made - Cincinnati incorporated. (n.d.-b). <http://www.assets.e-ci.com/PDF/Products/baam-fact-sheet.pdf>
- [41] Emeline. (n.d.). *Ingersoll - MasterPrint® 3X*. Multistation EN. <https://www.multistation.com/en/product/ingersoll-masterprint-3x/>
- [42] Marrett, D. (n.d.). *Thermwood LSAM - large scale additive manufacturing*. [https://www.thermwood.com/lсам\\_home.htm](https://www.thermwood.com/lсам_home.htm)

- [43] Millebot, Inc. (n.d.). *MILLEBOT 500 series*. MilleBot Intermodal Machine Platform for Advanced Digital-Manufacturing. <https://www.millebot.com/mille500>
- [44] *All specifications of the tested thermoplastic material for large scale 3D printing*. CEAD. (2023, September 28). <https://ceadgroup.com/materials/>
- [45] *Industrial 3D printer FGF Super Discovery 3D printer*. Discovery 3D Printers. (2023, November 17). <https://discovery3dprinter.com/en/super-discovery-3d-printer-2/>
- [46] Tyrer-Jones, A., Shaikhmag, A., Petch, M., Hanaphy, P., Sertoglu, K., & Everett, H. (2020, November 11). *Titan robotics launches Atlas 3.6 large-format pellet extrusion 3D printer*. 3D Printing Industry. <https://3dprintingindustry.com/news/titan-robotics-launches-atlas-3-6-large-format-pellet-extrusion-3d-printer-179026/#:~:text=Compatible%20with%20Titan%27s%20Dual%20Pellet,kind%20currently%20on%20the%20market.>
- [47] Severi, A., Teghini, T., Lazzari, G., & Schiavarelli, N. (2023, August 31). *Large scale 3D printer: WASP 3MT HDP*. WASP. <https://www.3dwasp.com/en/wasp-3mt-hdp-big-3d-printer/>
- [48] *The factory of the future: 3D demonstrators*. The Factory of The Future: 3D Demonstrators. (n.d.). <https://www.stratasys.com/en/demonstrators/>
- [49] C. Rauwendaal, *Polymer Extrusion*, 2nd ed., Hanser, Munich(1990)
- [50] Extruder, twin-screw. (n.d.). *SpringerReference*. [https://doi.org/10.1007/springerreference\\_210825](https://doi.org/10.1007/springerreference_210825)
- [51] Simplified models for single-screw extrusion applications - UFRGS. (n.d.-a). <https://lume.ufrgs.br/bitstream/handle/10183/8316/000573468.pdf?...1>
- [52] 2017, S. by D. 14. (2021, February 3). *An introduction to single screw extrusion*. AZoM.com. <https://www.azom.com/article.aspx?ArticleID=13566>
- [53] M.J. Stevens and J.A. Covas, *Extruder Principles and Operation*, 2nd ed., Chapman and Hall, London (1995)
- [54] BRUIN, S., VAN ZUILICHEM, D. J., & STOLP, W. (1978). A review of fundamental and engineering aspects of extrusion of biopolymers in a single-screw extruder. *Journal of Food Process Engineering*, 2(1), 1–37. <https://doi.org/10.1111/j.1745-4530.1978.tb00193.x>
- [55] *Examination of the performance of a high speed single screw extruder for several different extrusion applications*. Wiki. (n.d.). <http://extrusionwiki.com/wiki/POTM-Nov-2012.ashx>
- [56] The design and construction of a single screw extruder - JMEST. (n.d.). <https://www.jmest.org/wp-content/uploads/JMESTN42352996.pdf>
- [57] Tseng, J.-W., Liu, C.-Y., Yen, Y.-K., Belkner, J., Bremicker, T., Liu, B. H., Sun, T.-J., & Wang, A.-B. (2018). Screw extrusion-based additive manufacturing of Peek. *Materials & Design*, 140, 209–221. <https://doi.org/10.1016/j.matdes.2017.11.032>
- [58] Liu, X., Chi, B., Jiao, Z., Tan, J., Liu, F., & Yang, W. (2017). A large-scale double-stage-screw 3d printer for fused deposition of plastic pellets. *Journal of Applied Polymer Science*, 134(31). <https://doi.org/10.1002/app.45147>

- [59] Magnoni, P., Rebaioli, L., Fassi, I., Pedrocchi, N., & Tosatti, L. M. (2017). Robotic AM system for plastic materials: Tuning and on-line adjustment of process parameters. *Procedia Manufacturing*, *11*, 346–354. <https://doi.org/10.1016/j.promfg.2017.07.117>
- [60] Rebaioli, L., Magnoni, P., Fassi, I., Pedrocchi, N., & Molinari Tosatti, L. (2019a). Process parameters tuning and online re-slicing for robotized additive manufacturing of Big Plastic Objects. *Robotics and Computer-Integrated Manufacturing*, *55*, 55–64. <https://doi.org/10.1016/j.rcim.2018.07.012>
- [61] Schmidt, L., Schrickler, K., Bergmann, J. P., Hussenöder, F., & Eiber, M. (2019). Characterization of a granulate-based strand deposition process in the FLM-method for definition of material-dependent process strategies. *Rapid Prototyping Journal*, *25*(1), 104–116. <https://doi.org/10.1108/rpj-09-2017-0186>
- [62] Roschli, A., Gaul, K. T., Boulger, A. M., Post, B. K., Chesser, P. C., Love, L. J., Blue, F., & Borish, M. (2019). Designing for big area additive manufacturing. *Additive Manufacturing*, *25*, 275–285. <https://doi.org/10.1016/j.addma.2018.11.006>
- [63] Justino Netto, J. M., Idogava, H. T., Frezzatto Santos, L. E., Silveira, Z. de, Romio, P., & Alves, J. L. (2021). Screw-assisted 3D printing with granulated materials: A systematic review. *The International Journal of Advanced Manufacturing Technology*. <https://doi.org/10.1007/s00170-021-07365-z>
- [64] Alexandre, A., Cruz Sanchez, F. A., Boudaoud, H., Camargo, M., & Pearce, J. M. (2020). Mechanical properties of direct waste printing of polylactic acid with universal pellets extruder: Comparison to fused filament fabrication on open-source desktop three-dimensional printers. *3D Printing and Additive Manufacturing*, *7*(5), 237–247. <https://doi.org/10.1089/3dp.2019.0195>
- [65] Langnau, L. (n.d.). *Which is better-filament or pellet 3D printing materials?*. Make Parts Fast. <https://www.makepartsfast.com/better-filament-pellet-3d-printing-materials/#:~:text=Another%20difference%2C%20the%20cost%20of,good%20source%20of%20plastic%20pellets.>
- [66] Shaik, Y. P., Schuster, J., & Shaik, A. (2021). A Scientific Review on various pellet extruders used in 3D printing FDM Processes. *OALib*, *08*(08), 1–19. <https://doi.org/10.4236/oalib.1107698>
- [67] Saleh Alghamdi, S., John, S., Roy Choudhury, N., & Dutta, N. K. (2021). Additive Manufacturing of Polymer Materials: Progress, promise and challenges. *Polymers*, *13*(5), 753. <https://doi.org/10.3390/polym13050753>
- [68] Bourell, D., Kruth, J. P., Leu, M., Levy, G., Rosen, D., Beese, A. M., & Clare, A. (2017). Materials for additive manufacturing. *CIRP Annals*, *66*(2), 659–681. <https://doi.org/10.1016/j.cirp.2017.05.009>
- [69] Singh, S., Ramakrishna, S., & Singh, R. (2017). Material issues in additive manufacturing: A Review. *Journal of Manufacturing Processes*, *25*, 185–200. <https://doi.org/10.1016/j.jmapro.2016.11.006>
- [70] Ngo, T. D., Kashani, A., Imbalzano, G., Nguyen, K. T. Q., & Hui, D. (2018). Additive Manufacturing (3D printing): A review of materials, methods, applications and challenges. *Composites Part B: Engineering*, *143*, 172–196. <https://doi.org/10.1016/j.compositesb.2018.02.012>
- [71] Billah, K. M., Lorenzana, F. A. R., Martinez, N. L., Wicker, R. B., & Espalin, D. (2020). Thermomechanical characterization of short carbon fiber and short glass fiber-reinforced ABS used

- in large format additive manufacturing. *Additive Manufacturing*, 35, 101299. <https://doi.org/10.1016/j.addma.2020.101299>
- [72] Jiang, Z., Diggie, B., Tan, M. L., Viktorova, J., Bennett, C. W., & Connal, L. A. (2020). Extrusion 3D printing of polymeric materials with advanced properties. *Advanced Science*, 7(17). <https://doi.org/10.1002/advs.202001379>
- [73] Nichetti, D., & Manas-Zloczower, I. (1999). Influence of molecular parameters on material processability in extrusion processes. *Polymer Engineering & Science*, 39(5), 887–895. <https://doi.org/10.1002/pen.11478>
- [74] Northcutt, L. A., Orski, S. V., Migler, K. B., & Kotula, A. P. (2018). Effect of processing conditions on crystallization kinetics during materials extrusion additive manufacturing. *Polymer*, 154, 182–187. <https://doi.org/10.1016/j.polymer.2018.09.018>
- [75] Lyu, Y., Wu, J., Zhang, H., Brádaigh, C. M., & Yang, D. (2023). Effects of thermal process conditions on crystallinity and mechanical properties in material extrusion additive manufacturing of discontinuous carbon fibre reinforced polyphenylene sulphide composites. *Journal of Composite Materials*, 57(24), 3775–3787. <https://doi.org/10.1177/00219983231194391>
- [76] Chen, P., Wang, H., Su, J., Tian, Y., Wen, S., Su, B., Yang, C., Chen, B., Zhou, K., Yan, C., & Shi, Y. (2022). Recent advances on high-performance polyaryletherketone materials for Additive Manufacturing. *Advanced Materials*, 34(52). <https://doi.org/10.1002/adma.202200750>
- [77] Porter, M., & Yu, J. (2011). Crystallization kinetics of poly(3-hydroxybutyrate) granules in different environmental conditions. *Journal of Biomaterials and Nanobiotechnology*, 02(03), 301–310. <https://doi.org/10.4236/jbnb.2011.23037>
- [78] Crass, A. (2021, December 30). *What is a high performance plastic?*. Performance Plastics. <https://performanceplastics.com/blog/what-is-a-high-performance-plastic/>
- [79] Weyhrich, C. W., & Long, T. E. (2022). Additive Manufacturing of high-performance engineering polymers: Present and future. *Polymer International*, 71(5), 532–536. <https://doi.org/10.1002/pi.6343>
- [80] Barile, M., Lecce, L., Iannone, M., Pappadà, S., & Roberti, P. (2020). Thermoplastic Composites for aerospace applications. *Revolutionizing Aircraft Materials and Processes*, 87–114. [https://doi.org/10.1007/978-3-030-35346-9\\_4](https://doi.org/10.1007/978-3-030-35346-9_4)
- [81] *Polyether ether ketone market - peek - size, share & forecast*. Polyether Ether Ketone Market - PEEK - Size, Share & Forecast. (n.d.). <https://www.mordorintelligence.com/industry-reports/polyether-ether-ketone-peek-market>
- [82] *Polyether ether ketone (PEEK) market analysis: Industry market size, plant capacity, production, technology, operating efficiency, Demand & Supply, end-use, foreign trade, sales channel, regional demand, company share, 2015-2035*. PEEK Market | Polyether Ether Ketone Industry Size, 2035. (n.d.). <https://www.chemanalyst.com/industry-report/polyether-ether-ketone-peek-market-678>
- [83] Platt, D. K. (2003). *Engineering and high performance plastics market report: A rapra market report*. Rapra Technology Ltd.
- [84] Polymer composites in Aviation Sector - International Journal of ... (n.d.-b). <https://www.ijert.org/research/polymer-composites-in-aviation-sector-IJERTV6IS060291.pdf>

- [85] Red, C. (n.d.). *Thermoplastics in aerospace composites outlook, 2014-2023*. CompositesWorld. <https://www.compositesworld.com/articles/the-outlook-for-thermoplastics-in-aerospace-composites-2014-2023>
- [86] Zeyrek BY, Aydogan B, Dilekcan E, et al. Review of Thermoplastic Composites in Aerospace Industry. *Int J Eng Tech & Inf*. 2022;3(1):1–6. DOI: 10.51626/ijeti.2022.03.00031
- [87] CDI Products. (2023, October 12). *Thermoplastics and the modern aviation industry*. <https://www.cdiproducts.com/blog/thermoplastics-and-the-modern-aviation-industry>
- [88] CDI Products. (2021, December 6). *The top 6 thermoplastics trusted in the healthcare industry*. <https://www.cdiproducts.com/blog/the-top-6-thermoplastics-trusted-in-the-healthcare-industry>
- [89] Wiesli, M. G., & Özcan, M. (2015). High-performance polymers and their potential application as medical and oral implant materials. *Implant Dentistry, Publish Ahead of Print*. <https://doi.org/10.1097/id.0000000000000285>
- [90] Panayotov, I. V., Orti, V., Cuisinier, F., & Yachouh, J. (2016). Polyetheretherketone (PEEK) for medical applications. *Journal of Materials Science: Materials in Medicine*, 27(7). <https://doi.org/10.1007/s10856-016-5731-4>
- [91] Editor, S. (2023, February 16). *The advantages of using PEEK in high-performance automotive applications*. Shengwen. <https://www.tuntunplastic.com/news/the-advantages-of-using-peek-in-high-performance-automotive-applications.html#:~:text=of%20these%20components.-,3..choice%20for%20these%20demanding%20applications.>
- [92] Products, S. by Z. I. (2019, September 27). *Using Peek for next-generation Automotive Technology*. AZoM.com. <https://www.azom.com/article.aspx?ArticleID=13956>
- [93] *450GTM peek*. Victrex. (n.d.). <https://www.victrex.com/en/products/polymers/peek-polymers/450g>
- [94] Tafaoli-Masoule, M., Shakeri, M., Zahedi, S. A., & Vaezi, M. (2022). Experimental investigation of process parameters in polyether ether ketone 3D printing. *Proceedings of the Institution of Mechanical Engineers, Part E: Journal of Process Mechanical Engineering*, 095440892211415. <https://doi.org/10.1177/09544089221141554>
- [95] Pulipaka, A., Gide, K. M., Beheshti, A., & Bagheri, Z. S. (2023). Effect of 3D printing process parameters on surface and mechanical properties of FFF-Printed Peek. *Journal of Manufacturing Processes*, 85, 368–386. <https://doi.org/10.1016/j.jmapro.2022.11.057>
- [96] Atatreh, S., Alyammahi, M. S., Susantyoko, R. A., & Mohammed, A. (2022). Investigation of the dimensional accuracy of additively manufactured high-temperature material (PEEK). *Volume 4: Biomedical and Biotechnology; Design, Systems, and Complexity*. <https://doi.org/10.1115/imece2022-95692>
- [97] Rehekampff, C., Schroeffler, A., Irlinger, F., & Lueth, T. C. (2019). Influence of infill structures and process parameters on the tensile strength of 3D-printed peek parts. *2019 IEEE International Conference on Robotics and Biomimetics (ROBIO)*. <https://doi.org/10.1109/robio49542.2019.8961457>
- [98] Lee, A., Wynn, M., Quigley, L., Salviato, M., & Zobeiry, N. (2022). Effect of temperature history during additive manufacturing on crystalline morphology of Peek. *Advances in Industrial and Manufacturing Engineering*, 4, 100085. <https://doi.org/10.1016/j.aime.2022.100085>

- [99] Yang, C., Tian, X., Li, D., Cao, Y., Zhao, F., & Shi, C. (2017). Influence of thermal processing conditions in 3D printing on the crystallinity and mechanical properties of Peek Material. *Journal of Materials Processing Technology*, 248, 1–7. <https://doi.org/10.1016/j.jmatprotec.2017.04.027>
- [100] Zhao, D., Li, T., Zhang, H., Liu, W., Yue, G., & Pan, L. (2021). Effects of processing parameters and annealing on the mechanical properties of polyether ether ketone(peek) via fused deposition modeling(FDM). 2021 3rd International Academic Exchange Conference on Science and Technology Innovation (IAECST). <https://doi.org/10.1109/iaecst54258.2021.9695585>
- [101] Geng, P., Zhao, J., Wu, W., Ye, W., Wang, Y., Wang, S., & Zhang, S. (2019). Effects of extrusion speed and printing speed on the 3D printing stability of extruded peek filament. *Journal of Manufacturing Processes*, 37, 266–273. <https://doi.org/10.1016/j.jmapro.2018.11.023>
- [102] Wang, P., Zou, B., Xiao, H., Ding, S., & Huang, C. (2019). Effects of printing parameters of fused deposition modeling on mechanical properties, surface quality, and microstructure of Peek. *Journal of Materials Processing Technology*, 271, 62–74. <https://doi.org/10.1016/j.jmatprotec.2019.03.016>
- [103] Wang, H., Chen, P., Shu, Z., Chen, A., Su, J., Wu, H., Chen, Z., Yang, L., Yan, C., & Shi, Y. (2023). Laser powder bed fusion of poly-ether-ether-ketone/bioactive glass composites: Processability, mechanical properties, and bioactivity. *Composites Science and Technology*, 231, 109805. <https://doi.org/10.1016/j.compscitech.2022.109805>
- [104] Wang, H., Chen, P., Wu, H., Chen, A., Wu, S., Su, J., Wang, M., Feng, X., Yang, C., Yang, L., Yan, C., & Shi, Y. (2022). Comparative evaluation of printability and compression properties of poly-ether-ether-ketone triply periodic minimal surface scaffolds fabricated by laser powder bed fusion. *Additive Manufacturing*, 57, 102961. <https://doi.org/10.1016/j.addma.2022.102961>
- [105] Alberto, M. (2013). Introduction of fibre-reinforced polymers – polymers and composites: Concepts, properties and Processes. *Fiber Reinforced Polymers - The Technology Applied for Concrete Repair*. <https://doi.org/10.5772/54629>
- [106] Ray, B. C., & Rathore, D. (2014). Environmental damage and degradation of FRP Composites: A review report. *Polymer Composites*, 36(3), 410–423. <https://doi.org/10.1002/pc.22967>
- [107] Pitarresi, G., Scalici, T., & Catalanotti, G. (2019). Infrared Thermography assisted evaluation of static and fatigue mode II fracture toughness in FRP Composites. *Composite Structures*, 226, 111220. <https://doi.org/10.1016/j.compstruct.2019.111220>
- [108] Ramli, N., Norkhairunnisa, M., Ando, Y., Abdan, K., & Leman, Z. (2022). Advanced polymer composite for Aerospace Engineering Applications. *Advanced Composites in Aerospace Engineering Applications*, 1–21. [https://doi.org/10.1007/978-3-030-88192-4\\_1](https://doi.org/10.1007/978-3-030-88192-4_1)
- [109] Davis, J. (2021, November 20). *What materials can be added to concrete to make it stronger?*. HomeSteady. <https://homesteady.com/12588402/what-materials-can-be-added-to-concrete-to-make-it-stronger>
- [110] X, S. (2020, July 31). *Analyzing pros and cons of two composite manufacturing methods*. Phys.org. [https://phys.org/news/2020-07-pros-cons-composite-methods.html#google\\_vignette](https://phys.org/news/2020-07-pros-cons-composite-methods.html#google_vignette)

- [111] Luthada, P. (2022, July 18). *Challenges of switching to composite materials*. Addcomposites. <https://www.addcomposites.com/post/challenges-of-switching-to-composite-materials>
- [112] Hannah Mason, G. G. (2022, July 13). *3D printing with continuous fiber: A landscape*. CompositesWorld. <https://www.compositesworld.com/articles/3d-printing-with-continuous-fiber-a-landscape>
- [113] Yang, C., Tian, X., Liu, T., Cao, Y., & Li, D. (2017). 3D printing for continuous fiber reinforced thermoplastic composites: Mechanism and performance. *Rapid Prototyping Journal*, 23(1), 209–215. <https://doi.org/10.1108/rpj-08-2015-0098>
- [114] Caminero, M. A., Chacón, J. M., García-Moreno, I., & Reverte, J. M. (2018). Interlaminar bonding performance of 3D printed continuous fibre reinforced thermoplastic composites using fused deposition modelling. *Polymer Testing*, 68, 415–423. <https://doi.org/10.1016/j.polymertesting.2018.04.038>
- [115] Luo, M., Tian, X., Shang, J., Zhu, W., Li, D., & Qin, Y. (2019). Impregnation and interlayer bonding behaviours of 3D-printed continuous carbon-fiber-reinforced poly-ether-ether-ketone composites. *Composites Part A: Applied Science and Manufacturing*, 121, 130–138. <https://doi.org/10.1016/j.compositesa.2019.03.020>
- [116] Liu, T., Tian, X., Zhang, Y., Cao, Y., & Li, D. (2020). High-pressure interfacial impregnation by micro-screw in-situ extrusion for 3D printed continuous carbon fiber reinforced nylon composites. *Composites Part A: Applied Science and Manufacturing*, 130, 105770. <https://doi.org/10.1016/j.compositesa.2020.105770>
- [117] Rimašauskas, M., Kuncius, T., & Rimašauskienė, R. (2019). Processing of carbon fiber for 3D printed continuous composite structures. *Materials and Manufacturing Processes*, 34(13), 1528–1536. <https://doi.org/10.1080/10426914.2019.1655152>
- [118] Qin, Y., Ge, G., Yun, J., Tian, X., Liu, X., Han, J., & Gao, S. (2022). Enhanced impregnation behavior and interfacial bonding in CF/peek prepreg filaments for 3D printing application. *Journal of Materials Research and Technology*, 20, 4608–4623. <https://doi.org/10.1016/j.jmrt.2022.09.005>
- [119] Matsuzaki, R., Ueda, M., Namiki, M., Jeong, T.-K., Asahara, H., Horiguchi, K., Nakamura, T., Todoroki, A., & Hirano, Y. (2016). Three-dimensional printing of continuous-fiber composites by in-nozzle impregnation. *Scientific Reports*, 6(1). <https://doi.org/10.1038/srep23058>
- [120] Luo, M., Tian, X., Shang, J., Yun, J., Zhu, W., Li, D., & Qin, Y. (2020). Bi-scale interfacial bond behaviors of CCF/peek composites by plasma-laser cooperatively assisted 3D printing process. *Composites Part A: Applied Science and Manufacturing*, 131, 105812. <https://doi.org/10.1016/j.compositesa.2020.105812>
- [121] Köhler, T., Röding, T., Gries, T., & Seide, G. (2017). An overview of impregnation methods for Carbon Fibre Reinforced Thermoplastics. *Key Engineering Materials*, 742, 473–481. <https://doi.org/10.4028/www.scientific.net/kem.742.473>
- [122] Velu, R., Vaheed, N., Ramachandran, M. K., & Raspall, F. (2019). Experimental investigation of robotic 3D printing of high-performance thermoplastics (PEEK): A critical perspective to support automated fibre placement process. *The International Journal of Advanced Manufacturing Technology*, 108(4), 1007–1025. <https://doi.org/10.1007/s00170-019-04623-z>

- [123] Villmow, T., Kretzschmar, B., & Pötschke, P. (2010). Influence of screw configuration, residence time, and specific mechanical energy in twin-screw extrusion of polycaprolactone/multi-walled carbon nanotube composites. *Composites Science and Technology*, 70(14), 2045–2055. <https://doi.org/10.1016/j.compscitech.2010.07.021>
- [124] EXAIR, <https://www.exair.com/media/productcms/pdf/CompleteCatalog.pdf>
- [125] *Line VACTM*. EXAIR.com. (n.d.). <https://www.exair.com/line-vac.html?att=253%7C556#253=556>
- [126] Z. Zhang, Y. Long, Z. Yang, K. Fu, and Y. Li, “An investigation into printing pressure of 3D printed continuous carbon fiber reinforced composites,” *Composites Part A: Applied Science and Manufacturing*, vol. 162, p. 107162, 2022. doi:10.1016/j.compositesa.2022.107162
- [127] Hu, F., Mikolajczyk, T., Pimenov, D. Y., & Gupta, M. K. (2021, February 28). *Extrusion-based 3D printing of ceramic pastes: Mathematical Modeling and in situ shaping retention approach*. MDPI. <https://doi.org/10.3390/ma14051137>
- [128] Füllbrandt, M., Kesal, D., & von Klitzing, R. (2015). Multiscaling approach for non-destructive adhesion studies of metal/polymer composites. *ACS Applied Materials & Interfaces*, 7(30), 16247–16256. <https://doi.org/10.1021/acsami.5b01949>
- [129] Feng, X. J., & Jiang, L. (2006). Design and creation of superwetting/antiwetting surfaces. *Advanced Materials*, 18(23), 3063–3078. <https://doi.org/10.1002/adma.200501961>
- [130] Baek, I., Kwon, O., Lim, C.-M., Park, K. Y., & Bae, C.-J. (2022). 3D peek objects fabricated by fused filament fabrication (FFF). *Materials*, 15(3), 898. <https://doi.org/10.3390/ma15030898>
- [131] *Metal supply: Steel Supply: Metal Store*. Metal Supermarkets. (2023, November 13). <https://www.metalsupermarkets.com/>
- [132] Bai, H., Qin, W., Jia, S., Ren, L., An, Y., & Bao, J. (2021). A new type of 3D printing molding equipment: Overall structural design and the numerical simulation for the flow field characteristics of its screw module. *International Journal of Precision Engineering and Manufacturing*, 22(10), 1639–1656. <https://doi.org/10.1007/s12541-021-00564-4>
- [133] Vallurupalli, K., Farzadnia, N., & Khayat, K. H. (2021). Effect of flow behavior and process-induced variations on shape stability of 3D printed elements – a review. *Cement and Concrete Composites*, 118, 103952. <https://doi.org/10.1016/j.cemconcomp.2021.103952>
- [134] Minitab, LLC, “Determining the weight in response optimization.” <https://support.minitab.com/en-us/minitab/21/help-and-how-to/statistical-modeling/using-fitted-models/supporting-topics/response-optimization/determining-the-weight/>
- [133] N. A. Sukindar, M. K. Ariffin, B. T. Baharudin, C. N. Jaafar, and M. I. Ismail, “Analyzing the effect of nozzle diameter in fused deposition modeling for extruding polylactic acid using open source 3D printing,” *Jurnal Teknologi*, vol. 78, no. 10, 2016. doi:10.11113/jt.v78.6265
- [134] StructX.com. (n.d.). Metals/alloys - melting and annealing. [https://structx.com/Material\\_Properties\\_002a.html](https://structx.com/Material_Properties_002a.html)
- [135] *Metals - machinability*. Engineering ToolBox. (n.d.). [https://www.engineeringtoolbox.com/machinability-metals-d\\_1450.html](https://www.engineeringtoolbox.com/machinability-metals-d_1450.html)

- [136] idsBASINC\_webmgmt. (2023, June 6). *CNC Machining Brass Parts*. Basilius Inc. <https://www.basilius.com/blog/cnc-machining-for-brass-parts/>
- [137] Luo, D., Li, F., & Xing, G. (2022, January 1). *Corrosion resistance of 6061-T6 aluminium alloy and its feasibility of near-surface reinforcements in concrete structure*. De Gruyter. <https://www.degruyter.com/document/doi/10.1515/rams-2022-0048/html?lang=en>
- [138] *Alloy 360 brass (C36000) - sequoia brass & copper*. Sequoia Brass and Copper. (2023, April 10). <https://www.sequoia-brass-copper.com/brass/360-brass/>
- [139] Harris, A. (2023, July 31). *Does 304 stainless steel rust? common faqs: Arthur Harris*. Common FAQs | Arthur Harris. <https://arthurharris.com/news/does-304-stainless-steel-rust/>
- [140] *Carbon Steel vs stainless steel*. Markforged. (n.d.). <https://markforged.com/resources/blog/carbon-steel-vs-stainless-steel#:~:text=All%20carbon%20steels%20are%20susceptible,or%20high%2Dprecision%20manufaturing%20operations.>
- [141] *Technical Reference Solidworks Flow Simulation 2021*. Solidworks. <https://www.cati.com/wp-content/uploads/2021/04/swflow2021-technical-reference.pdf>
- [142] Koerdt, M., Koerdt, M., Grobrüg, T., Skowronek, M., & Herrmann, A. S. (2019). Modelling and analysis of the thermal characteristic of thermoplastic composites from hybrid textiles during compression moulding. *Journal of Thermoplastic Composite Materials*, 35(1), 127–146. <https://doi.org/10.1177/0892705719875204>
- [143] Ghosh, B., Xu, F., & Hou, X. (2021). Thermally conductive poly(ether ether ketone)/boron nitride composites with low coefficient of thermal expansion. *Journal of Materials Science*, 56(17), 10326–10337. <https://doi.org/10.1007/s10853-021-05923-0>
- [144] Yan, M., Tian, X., Peng, G., Li, D., & Zhang, X. (2018). High temperature rheological behavior and sintering kinetics of CF/Peek Composites during Selective Laser Sintering. *Composites Science and Technology*, 165, 140–147. <https://doi.org/10.1016/j.compscitech.2018.06.023>
- [145] Kelly, A. L., Brown, E. C., & Coates, P. D. (2006). The effect of screw geometry on melt temperature profile in single screw extrusion. *Polymer Engineering & Science*, 46(12), 1706–1714. <https://doi.org/10.1002/pen.20657>
- [146] “View Flexbot brochure - CEAD: Large Scale Additive Manufacturing,” CEAD, <https://ceadgroup.com/view-am-flexbot-brochure/> (accessed Jan. 2, 2024).
- [147] “MDAC50 additive cell,” Massive Dimension, <https://massivedimension.com/collections/printers/products/mdac50-mdpe50-abb-6700-additive-cell> (accessed Jan. 2, 2024).
- [148] Cebe, P., & Hong, S.-D. (1986). Crystallization behaviour of poly(ether-ether-ketone). *Polymer*, 27(8), 1183–1192. [https://doi.org/10.1016/0032-3861\(86\)90006-6](https://doi.org/10.1016/0032-3861(86)90006-6)

## Appendix 1



Figure 70. Rectangular geometry of 100mm x 70mm x 11mm 3D printed using PEEK.



Figure 71. 3D printed PEEK block of 200mm x 70mm x 11mm.

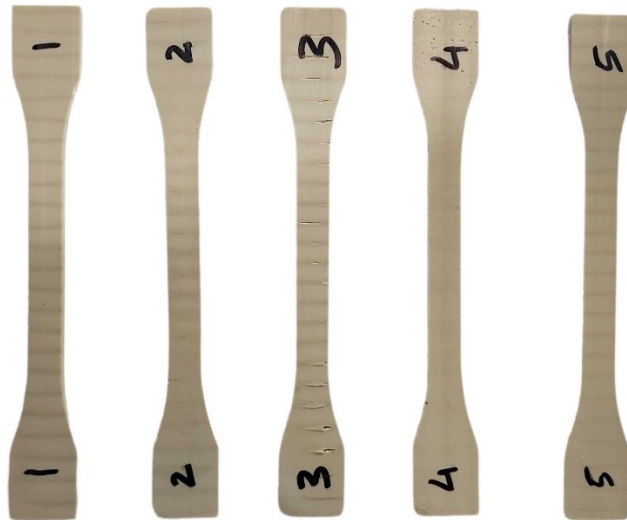
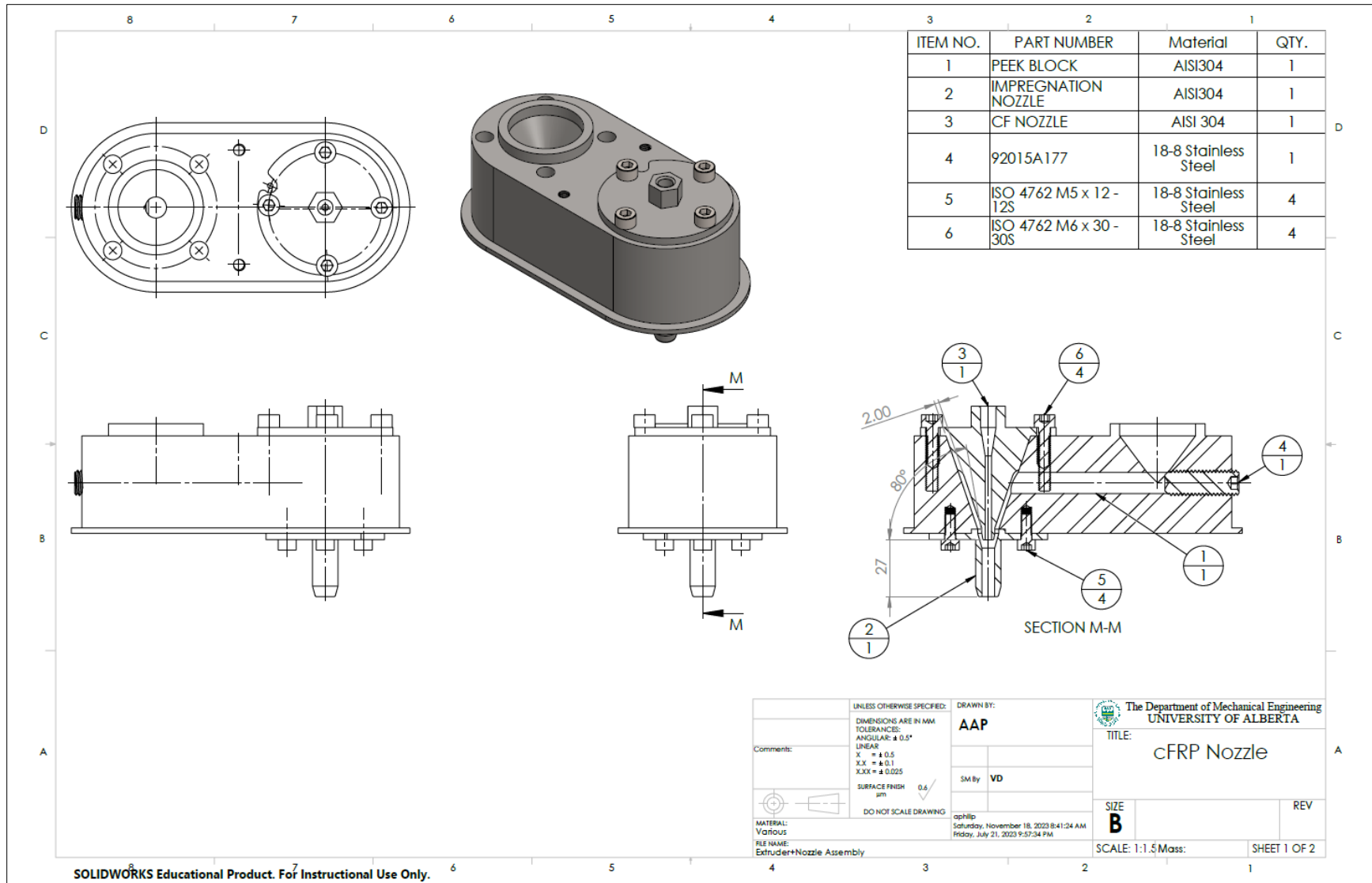


Figure 72 . Tensile test samples machined out as per ISO 527 from 3D printed PEEK block.

## **Appendix 2**

### Engineering drawing for cFRP Nozzle

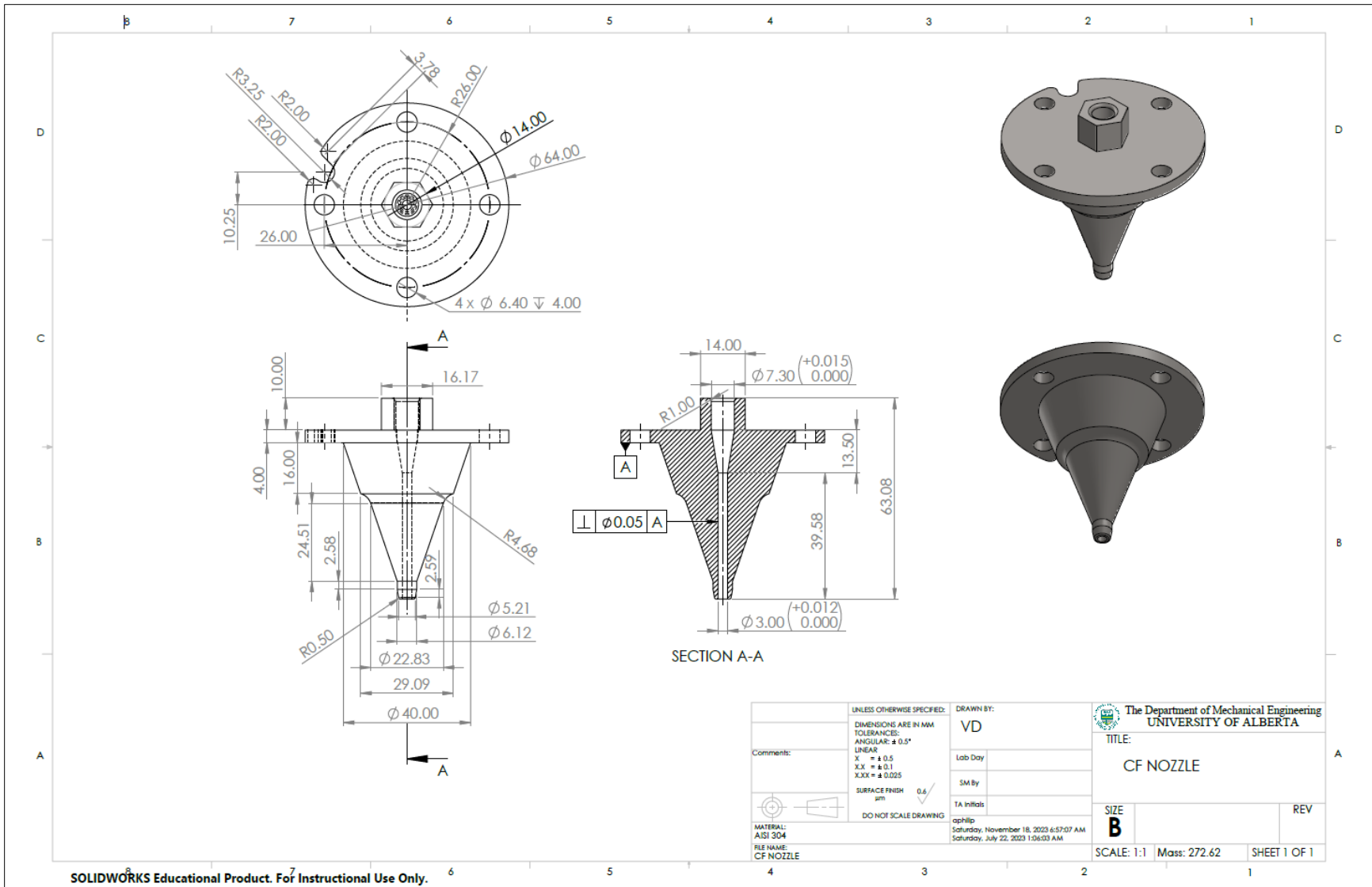
## A2.1 cFRP Nozzle assembly



SOLIDWORKS Educational Product. For Instructional Use Only.

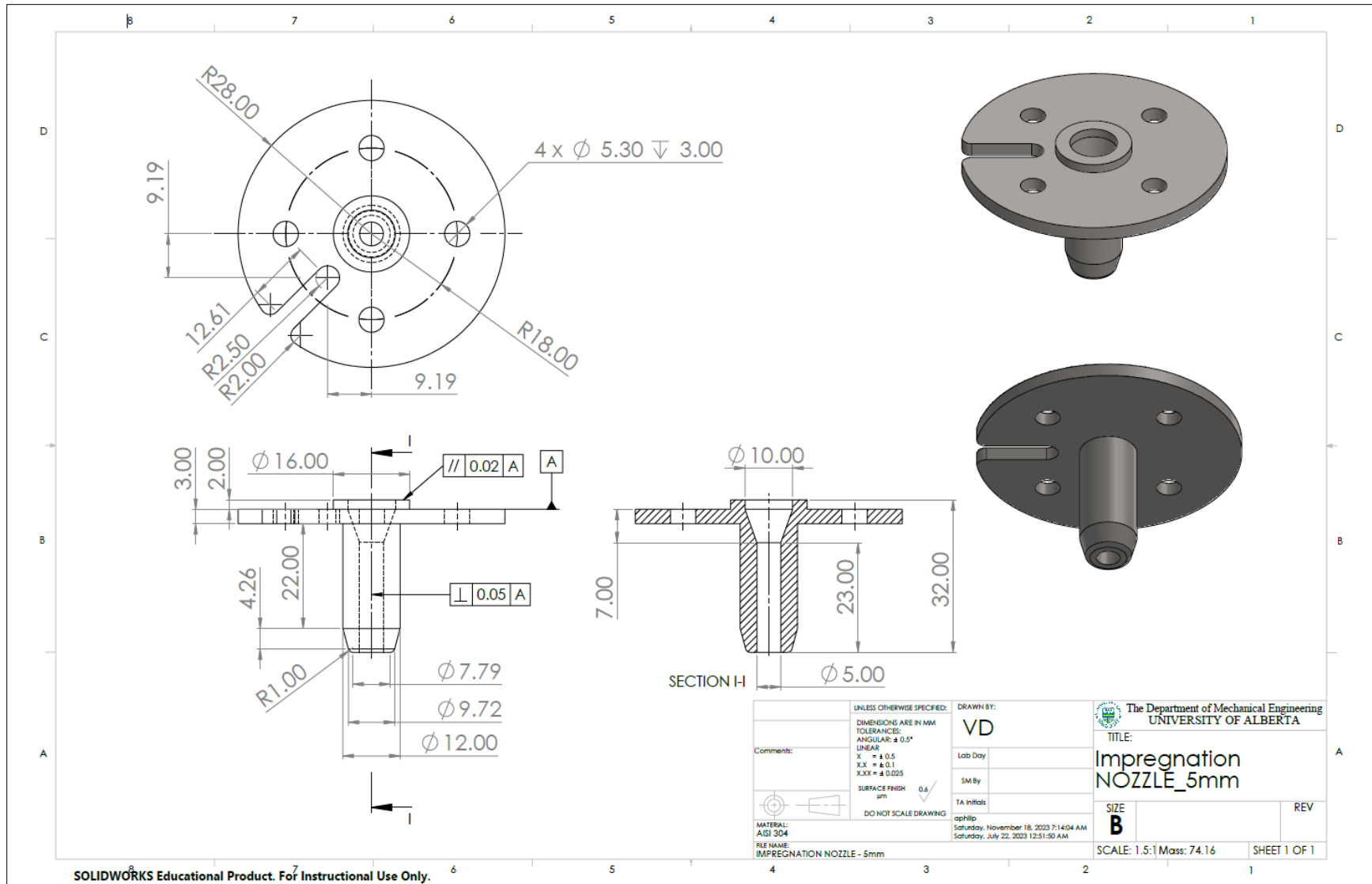


### A2.3 Drawing for CF Nozzle



SOLIDWORKS Educational Product. For Instructional Use Only.

## A2.4 Drawing for Impregnation Nozzle



SOLIDWORKS Educational Product. For Instructional Use Only.